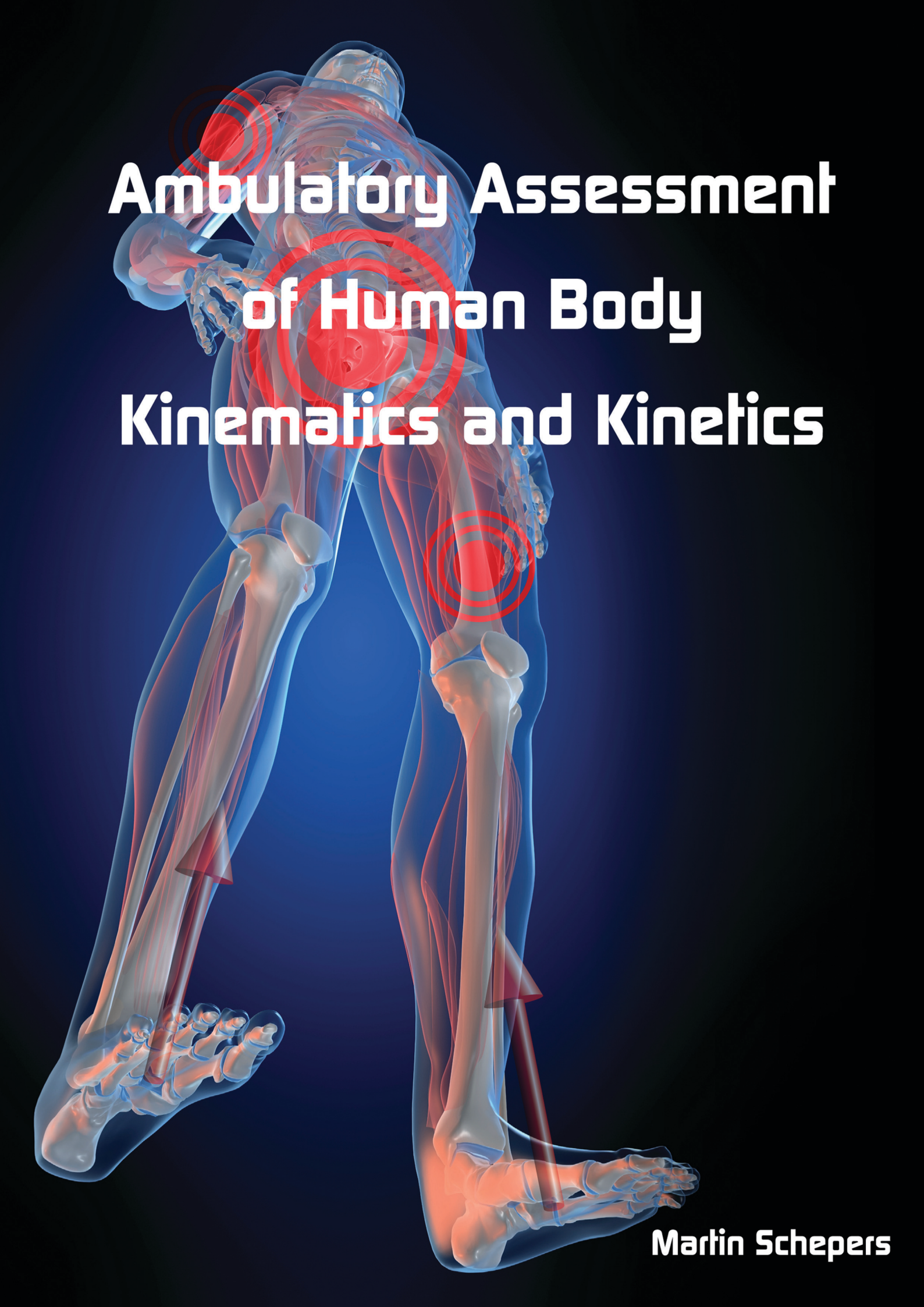

Ambulatory Assessment of Human Body Kinematics and Kinetics

Martin Schepers

Ambulatory Assessment of Human Body Kinematics and Kinetics

Martin Schepers

This work was financially supported by the Dutch Ministry of Economic Affairs under the FreeMotion project.

The publication of this thesis was financially supported by the following companies. Their support is gratefully acknowledged.

ATI Industrial Automation	www.ati-ia.com
Biometrics BV (see page 137)	www.biometrics.nl
OIM Orthopedie (see page 137)	www.oim.nl
Xsens Technologies BV (see page 137)	www.xsens.com

Samenstelling promotiecommissie:

Voorzitter en Secretaris (Chairman and Secretary)

Prof.dr.ir. A.J. Mouthaan	Universiteit Twente

Promotor

Prof.dr.ir. P.H. Veltink	Universiteit Twente

Leden (Members)

Prof.dr.ir. H.F.J.M. Koopman	Universiteit Twente
Prof.dr.ir. P.P.L. Regtien	Universiteit Twente
Prof.dr.ir. J.W.M. Bergmans	Technische Universiteit Eindhoven
Dr.ir. J. Harlaar	VU Medisch Centrum
Dr.ir. D. Roetenberg	Xsens Technologies BV

FSC
Mixed Sources
Product group from well-managed forests and other controlled sources

Cert no. CU-COC-811465
www.fsc.org
© 1996 Forest Stewardship Council

Paranimfen:
Remy Wiertz
Arjan Waterink

Cover design:
Danny Hof

Printed by:
Gildeprint Drukkerijen BV, Enschede, The Netherlands.

ISBN: 978-90-365-2844-3

Copyright ©2009 by H.M. Schepers, Hengelo, The Netherlands.
All rights reserved. No part of this publication may be reproduced or transmitted in any form or by any means, electronic or mechanical, including photocopy, recording or any information storage or retrieval system, without permission in writing from the author.

AMBULATORY ASSESSMENT OF HUMAN BODY KINEMATICS AND KINETICS

PROEFSCHRIFT

ter verkrijging van
de graad van doctor aan de Universiteit Twente,
op gezag van de rector magnificus,
prof.dr. H. Brinksma,
volgens besluit van het College voor Promoties
in het openbaar te verdedigen
op donderdag 25 juni 2009 om 16:45 uur

door

Herman Martin Schepers
geboren op 4 juli 1981
te Hardenberg

Dit proefschrift is goedgekeurd door de promotor:

Prof.dr.ir. P.H. Veltink

Contents

1 General Introduction 1

2 Ambulatory Assessment of Ankle and Foot Dynamics 13

3 Ambulatory Estimation of Foot Placement During Walking Using Inertial Sensors 29

4 Ambulatory Estimation of Center of Mass Displacement During Walking 41

5 Stochastic Magnetic Measurement Model for Relative Position and Orientation Estimation 55

6 Ambulatory Human Motion Tracking by Fusion of Inertial and Magnetic Sensing with Adaptive Actuation 71

7 General Discussion 87

A Derivation of the Stochastic Magnetic Model 95

B Derivation of the Process Model 107

References 111

Summary 121

Samenvatting 125

Dankwoord 129

About the Author 133

1

General Introduction

1.1 Traditional Human Movement Analysis

Human beings generate various movements during their everyday life activities such as walking, running and cycling. For centuries, tracking and display of human movements has been the topic of research and development for many purposes like knowledge generation, physical rehabilitation, sports training, and the construction of anthropomorphic robots. Over the last years, instrumentation and computer technologies have provided new opportunities for the study of human movement resulting in the development of wearable tracking solutions that do not impede natural movements and can operate for extended periods of time.

The science of human movement analysis probably originates from the work of Aristotle (384-322 BC). He wrote the first book called 'De Motu Animalium' - On the Movement of Animals, and is generally considered to be the first biomechanician. After a long period with no new thoughts and ideas, Leonardo da Vinci (1452-1519) (Figure 1.1) was the first who studied anatomy in the context of mechanics. He analyzed muscle forces as acting along lines connecting origins and insertions and studied joint function. In the 17th century, Galileo Galilei (1564-1642) also looked at the living body. Galileo was particularly aware of the mechanical aspects of bone structure, and the relations between size and shape. The work of Galileo was continued by Giovanni Alfonso Borelli (1608-1679), who wrote the second book called 'De Motu Animalium' [1]. A solid scientific foundation for our current understanding of human walking was provided by Braune (1831-1892) and Fischer (1861-1917) [2], who employed the principles of Newtonian classical mechanics [3], the coordinate geometry of Descartes [4], and Borelli's mathematical concepts for estimating muscle action, to create an elegant representation

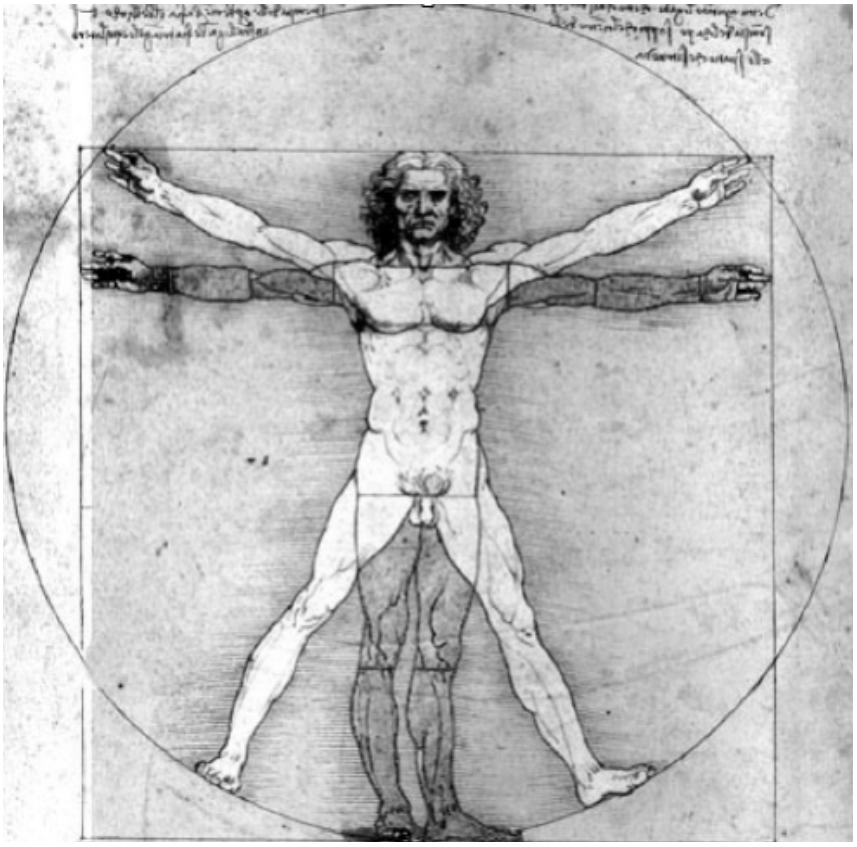

Figure 1.1: *Leonardo da Vinci: The Proportions of the Human Figure.*

of the gait of their military subjects carrying backpacks.

Over the last centuries, there have been several fundamental advancements on the development of new tools for observation of human movement that have made a substantial impact on our understanding of the human motor system [5]. The brothers Wilhelm (1804-1891) and Eduard Weber (1806-1871) [6] reported one of the first quantitative studies of temporal and spatial parameters during human locomotion. Their work established a model for subsequent quantitative studies of human locomotion. Muybridge (1830-1904) [7] and Marey (1830-1904) were among the first to quantify patterns of human movement using photographic techniques (Figure 1.2). They used a series of cameras to take multiple pictures in rapid succession of both animals and humans in movement. The classic work of Eberhart (1906-1993) and Inman (1905-1980) at the University of California [8, 9] provided a tremendous resource of knowledge related to the mechanics of human movement. They included the use of interrupted light to assess human movement (Figure 1.3). A photograph was obtained with the subject walking in front of the open lens of a camera while carrying small light bulbs located at the hip, knee, ankle and foot. A slotted disk was rotated in front of the camera, producing a series of white dots at equal time intervals. These dots could be laboriously connected to provide joint angles that could be manually measured. In order to examine transverse plane rotations, Inman drilled pins into the pelvis, femur, and tibia, and recorded pin rotation with the aid of a movie camera located above the subject. The work at the University of California formed the basis for many of the fundamental techniques currently used for the study of human movement.

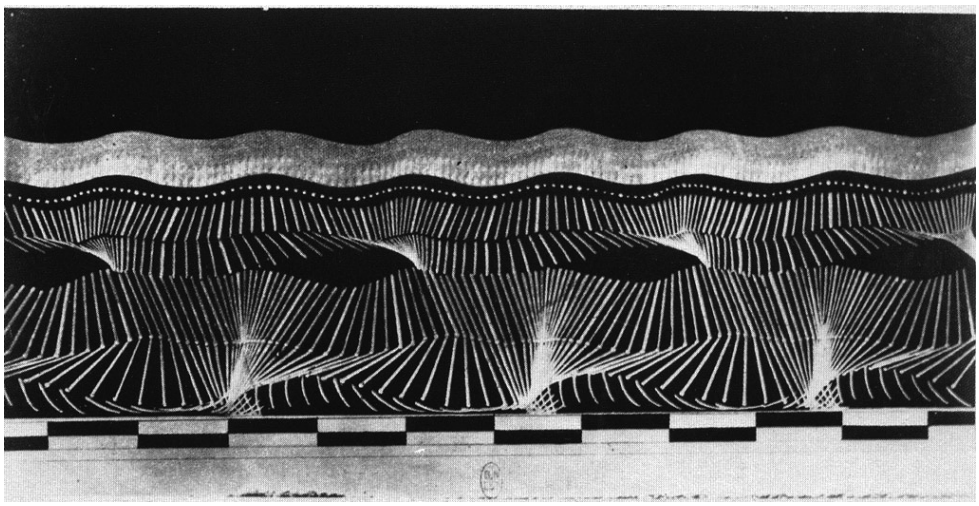

Figure 1.2: *Geometric chronophotograph of the man in the black suit made by Marey [10].*

Generally, the analysis of human movement can be separated in two parts. The first part is about kinematics, analysis of movement without considering the forces that cause the movement. The second part is about kinetics, analysis of forces that cause the movement. Both kinematics and kinetics will be described in the following sections. It should be noted that the assessment of kinematics and kinetics does not result in information for individual muscles. To detect the activity and contribution of individual muscles to movement, it is necessary to investigate the electrical activity of muscles which can be achieved using Electromyography (EMG). In this way it is possible to investigate the activation times of muscles and to some degree the magnitude of their activation, and thereby their contribution to human movement. Despite the important role of EMG in human movement analysis, it will not be discussed in more detail throughout this thesis.

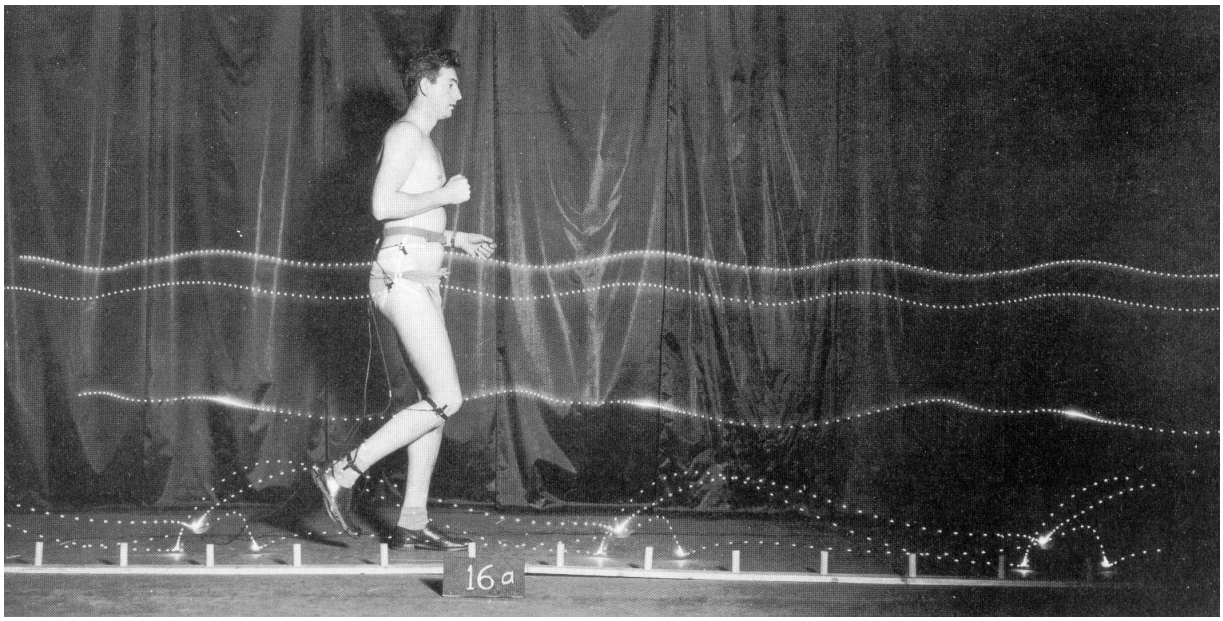

Figure 1.3: *Interrupted light study to assess human movement [11].*

1.1.1 Kinematics

In order to assess human body kinematics, several tracking solutions exist which are based on different sensing technologies. Specifically, motion tracking systems most often employ measurements of mechanical, acoustic, radio frequency, optical, magnetic, and inertial sensors. Each approach has advantages and limitations which will be discussed in this section

Mechanical sensing is typically used to determine joint angles. The system generally consists of two or more mechanical pieces interconnected with electromechanical transducers such as potentiometers or shaft encoders. As the user moves, the transducers move accordingly and the angle can be extracted. Although these systems measure directly at the joint, the linkages are uncomfortable to wear for extended periods of time, and impede movement. Moreover, mechanical sensing is difficult for complex joints such as the shoulder. Also, the relative position of the linkage with respect to the segment can change due to the movement of soft tissue.

Acoustic sensing operates either by timing the flight duration of a brief ultrasonic pulse, or by measuring the phase shift between the transmitted signal and the signal detected at a microphone [12]. A drawback of the phase shift method is that small errors in position estimation will accumulate over time (drift), since it is an incremental position estimation method. Another problem is the effect of multipath reflections which cause the received signal to be the sum of the direct path and one or more reflected signals of longer path lengths. An outstanding feature of pulsed time-of-flight acoustic systems is that most multipath reflection problems can be overcome by waiting until the first pulse arrives, which is guaranteed to have arrived via the direct path unless the signal is blocked. Yet, the requirement to wait for the next measurement until the multipath reflections of the previous measurement have decayed, influences the update rate negatively. Additionally, acoustic systems require a line of sight between emitter and receiver.

Radio and microwave sensing operates mostly on the principle of time of flight measurements, as described for acoustic sensing. The waves travel about a million times faster compared to acoustic sensing, making the task of measuring time of flight with sufficient precision more difficult. Recently, considerable interest has risen in Ultra-Wide Band (UWB) positioning,

Figure 1.4: *Inertial and magnetic sensor (MTx, Xsens Technologies B.V. [20]).*

which uses nonsinusoidal signals such as impulses. The advantages of UWB impulse radio technology are its ability to penetrate through non-metallic objects, its low energy requirements, and its robustness against multipath signals.

Optical sensing relies on measurements of emitted (active [13]) or reflected light (passive [14]), obtained from markers placed on the human body. Exact 3D marker locations are computed from images recorded by surrounding cameras using triangulation methods. Passive marker systems use reflected infrared light that is sent by Light Emitting Diodes (LEDs) mounted around the cameras to determine marker position. Active marker systems use pulsed infrared LEDs that are mounted on each segment to determine position. An advantage of active markers is that the markers can be distinguished automatically, since each marker can pulse at a predefined frequency. The primary disadvantage of all optical systems is that there must be a clear line of sight between camera and marker.

Magnetic sensing relies on measurements of the local magnetic field vector at the sensor. If purely the earth magnetic field is measured, heading of the sensor with respect to the global frame can be estimated [15, 16, 17]. Alternatively, a source with multiple coils can be used to actively induce excitations [18, 19]. Each of the source coils is actuated, and the corresponding magnetic field is measured by the sensor. With three of these excitations, the position and orientation of the sensor with respect to the source can be estimated. However, ferromagnetic and conductive material in the environment can affect the shape of a magnetic field. A significant component of the resulting field distortion is caused by unintended fields that appear around nearby conductive objects, since a changing magnetic field induces eddy currents in them. The source coils can be excited by either alternating (AC), or direct current (DC) signals. The advantage of an AC excited system is that multiple coils can be actuated simultaneously, but the alternating field continuously induces eddy currents in nearby conducting objects. When DC fields are used, a short waiting time is required for the initial transient of each excitation to decay. Furthermore, an additional measurement of the ambient magnetic field is required to extract the excitation response, as it is superimposed on the ambient magnetic field. With both AC and DC excited systems, the useful range of operation is limited due to the cubic falloff of the field as a function of the distance from the source. Despite the drawbacks, a major advantage is that the human body is transparent for the magnetic field applied, eliminating line of sight problems.

Inertial sensing uses accelerometers and gyroscopes to estimate change of position and orientation. It was the introduction of Micro Electro Mechanical Systems (MEMS) technology that made inertial sensors suitable for human movement analysis (Figure 1.4). Generally, miniature inertial sensors are rigidly attached to a segment, comprising a strapdown Inertial Navigation System (INS). The accelerometer, which consists of a damped mass suspended by a spring, measures sensor acceleration and gravitational acceleration. When the accelerometer experiences an external force such as gravity, the mass is displaced until the external force is balanced by the spring force. The displacement is measured and translated into acceleration. The gyroscope is used to measure angular velocity. It consists of a vibrating element that is, when rotated, subject to the Coriolis effect which causes a secondary vibration orthogonal to the original vibrating direction. Sensing the secondary vibration provides a measure of the angular velocity. Change of orientation can be estimated by integration of angular velocity. Change of position can be estimated by double integration of acceleration after removing the gravitational acceleration, which requires the inclination to be known. The main advantage of inertial sensors is that they are completely self-contained, which means no line of sight problems, no multipath problems and no sensitivity to interfering electromagnetic fields. The weakness of inertial sensors is their vulnerability to integration drift caused by noise and a fluctuating offset. Also, inertial sensors can not be used to estimate relative positions and orientations of sensors with respect to each other, since integration can only be used to estimate changes over time, and the initial position of each sensor is unknown. Yet, fusion of inertial sensors with other sensing technologies can overcome these weaknesses which will become clear in this thesis.

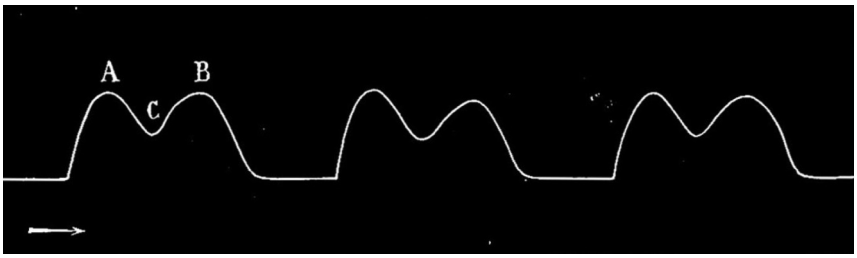

Figure 1.5: *The characteristic 'M'-shape of the vertical component of the ground reaction force during gait as recorded by Carlet [21].*

1.1.2 Kinetics

In order to calculate movement kinetics, the assessment of the three components of the Ground Reaction Force (GRF), the ground reaction moment (vertical), and the Center of Pressure (CoP) is essential. The GRF is the reaction force of the ground to the force that a human subject applies to the ground. The CoP is the application point of the GRF, the point on the contact surface between body and ground where the moments about the horizontal axes are zero.

The search for scientific methods of recording the magnitude of the GRF began in the 19th century. The first to register the characteristic 'M'-shape of the vertical GRF during gait were Marey and Carlet (1849-1892) [21] (Figure 1.5), who developed and utilized air reservoirs placed in the thick rubber sole of a shoe to measure the vertical force applied to the foot. When the foot made contact with the ground, the air reservoir was compressed which actuated a lever via a pneumatic tube for recording [22]. Demeny (1850-1918) and Marey used comparable technology to devise a force plate using a pneumatic mechanism [10]. Although

the early investigators understood that the GRF is a vector force, they lacked the technology to separate the GRF into three components. The first to develop a 3D (pneumatic) force plate was Jules Amar (1879-1935), who further developed the single component pneumatic force plate of Marey and Demeny to produce the 'Trottoire Dynamographique' [23] (Figure 1.6). His ideas were later developed by Elftman to produce a full 3D mechanical force plate [24]. The next development in force plate technology was that of a full 6D force plate using strain gauges by engineers Cunningham and Brown [25]. The efforts of scientists in several locations reduced the complexity of the platforms and improved the accuracy and reliability of the sensing instruments, which resulted soon in the first commercially available force plates. The current state of the art for GRF sensing is a 6D force plate based on either strain gauges [26], or piezoelectricity [27].

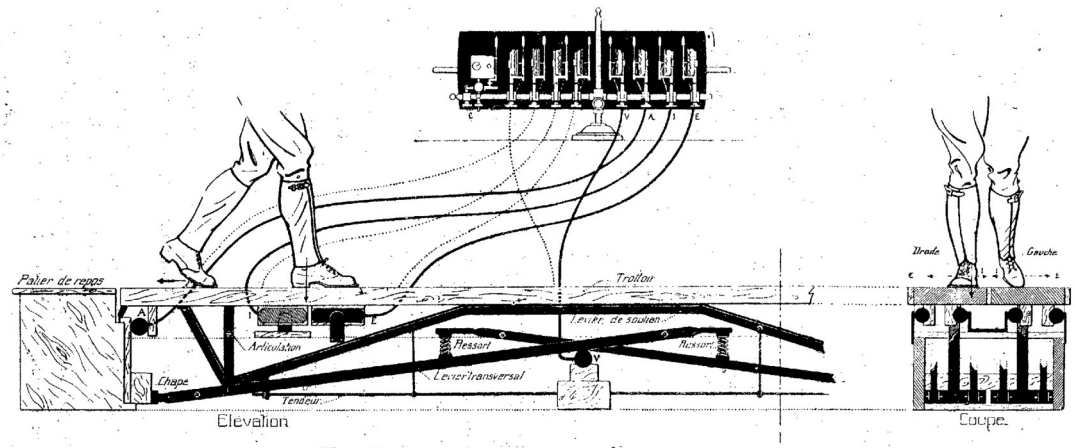

Figure 1.6: *Amar's 'Trottoire Dynamographique' [23].*

1.2 Ambulatory Assessment of Human Movement

An optical position measurement system with one or more 6D force plates is clinically accepted as 'the golden standard' for the assessment of human movement. Despite the high accuracy to assess position, optical position measurement systems are generally restricted to a laboratory environment with a limited measurement volume, which hinders their use during everyday life. Also, optical measurement systems suffer from marker visibility problems, since the line of sight from camera to marker is easily blocked due to movement of the subject. Force plates provide an accurate measurement of the GRF, but are also restricted to a laboratory environment. Moreover, subjects are required to place their feet completely on the force plates in order to perform a correct force measurement, which poses a restriction on the natural gait pattern. With only one or a few force plates mounted in a laboratory, this also means that usually many successive trials are required to obtain sufficient data. A final drawback is the impossibility to distinguish the GRF acting on each foot when standing with both feet on a single force plate, as only the total GRF is registered. These drawbacks stimulated several research groups to investigate alternative analysis methods that are capable of providing quantitative and repeatable results over extended periods of time.

1.2.1 Ambulatory Assessment of Kinematics

Inertial sensing provides a suitable ambulatory alternative for the assessment of human body kinematics. As mentioned, two important drawbacks of inertial sensing are the inherent drift due to integration of sensor signals and the inability to estimate relative positions and orientations of sensors with respect to each other. Especially for biomechanical applications, relative positions and orientations on the human body are of importance. Examples are the relation between the center of mass and the center of pressure for balance assessment, the estimation of relative positions in virtual reality applications, or the quantification of mechanical loading. Fusion of inertial sensing with a complementary sensing system can overcome both drawbacks.

Recently, it has been shown by several researchers that a stable and accurate estimate of orientation can be obtained by fusion of inertial and magnetic sensing in a Kalman filter structure [28, 16, 17, 20]. Gyroscopes are used to estimate change of orientation by integration of angular velocity. During periods of low acceleration, the accelerometer provides an estimate of inclination. Similarly, the magnetometer provides an estimate of heading obtained from the earth magnetic field. Ferromagnetic materials disturbing the earth magnetic field can be detected and compensated for, such that the orientation estimation remains unaffected [28]. This method can also be used to estimate relative orientations of sensors with respect to each other, provided that a homogeneous earth magnetic field is measured.

In order to obtain a stable and accurate estimate of position, inertial sensing can be fused with aiding systems such as GPS [29], optical sensing [30], acoustic sensing [31], UWB [32], or magnetic sensing [33]. Also, relative positions may be estimated using segment orientations and a kinematic model of the human body. However, the accuracy is limited, especially for complex joints such as the shoulder. The aforementioned advantage of magnetic sensing compared to the other examples is that the human body is transparent for the magnetic field applied. Additionally, magnetic sensing is suitable for possible use in an indoor environment, although it is sensitive to ferromagnetic objects in the environment. Commonly used existing magnetic systems [18, 19] are based on a fixed source positioned somewhere in a room, which does not

Figure 1.7: *Picture of the instrumented shoe with two 6D force/moment sensors beneath the heel and the forefoot proposed by Veltink et al. [36].*

allow the measurements to be performed during everyday life. An ambulatory alternative using a magnetic source that can be worn on the body has been proposed by Roetenberg *et al.* [34]. In a successive study [35], the measurement system was fused with an inertial sensor system using a complementary Kalman filter structure. Despite the satisfying results, several aspects of the measurement system require improvements before the system can be used during everyday life. The proposed system is based on a source coil configuration using three coils in an orthogonal arrangement sharing the same origin. For daily life use, it is intended to integrate the coils in garments, which means the system should not depend on a specific configuration. Also, it actuates all three coils every update at a fixed update rate, which is not desired from an energetic point of view. A final aspect that needs improvement is the structure of the fusion filter. The fusion filter proposed in [35] has a loosely coupled structure, which means inertial and magnetic measurements are processed separately to obtain positions and orientations which are then fed into the fusion filter. The independent estimation of position and orientation by the magnetic system requires each magnetic update to contain at least three independent actuations. In a tightly coupled structure on the contrary, the magnetic measurements are processed individually, which allows a single coil to be actuated each magnetic update. It also allows the stochastic characteristics of the magnetic measurement system to be propagated through the fusion filter.

1.2.2 Ambulatory Assessment of Kinetics

In order to assess human body kinetics using an ambulatory measurement system, several researchers have tried to construct a 'force plate' attached to the subject. Generally, the measurement system is a shoe like structure, where the force measurements are either performed in the shoe or beneath the shoe. An examples of an in-shoe measurement system to assess vertical force, bending of the sole and movement of the foot was given by Bamberg *et al.* [37]. A miniature triaxial piezoelectric transducer measuring three orthogonal stress components inside a shoe was described by Razian and Pepper [38]. For biomechanical studies, it is desired to assess the three components of the GRF beneath the shoe. Several studies describe the artificial 3D GRF estimation from 1D in-shoe pressure measurement [39, 40, 41]. A first attempt for an ambulatory measurement of the GRF beneath the shoe was made by Kljajić and Krajnik [42]. An instrumented shoe with two 6D force/moment sensors beneath the heel and the forefoot was presented by Chao and Yin [43], and Veltink *et al.* [36] (Figure 1.7). While the movement of the sole in the first design is constrained by a hinge between the front and rear sensor, the latter design allowed distributed deformation of the shoe sole. An essential aspect still missing in these designs is the measurement of foot movement, which is required since, in contrast to a force plate, the force transducers follow the movement of the foot. The combined assessment of force and movement using an ambulatory measurement system also allows inverse dynamics calculations each stride.

1.3 Thesis Objectives

This thesis has two objectives to overcome some essential limitations of existing systems for ambulatory assessment of human body kinematics and kinetics, and can be summarized as follows:

- Develop and evaluate a method to assess the 3D ground reaction force, the center of pressure trajectory, the center of mass trajectory, and the movement of the foot using an

instrumented shoe.

- Develop and evaluate a method to estimate relative positions and orientations on the human body by fusion of inertial and magnetic sensing using a tightly coupled filter structure. The method should not be dependent on a specific coil configuration and should allow the instants of actuation to be chosen adaptively based on the uncertainty of the estimated position and orientation. Furthermore, the number of actuations and the actuation parameters should be chosen such that the system achieves maximal accuracy at minimal energy consumption.

1.4 Thesis Outline

Based on the objectives mentioned in the previous section, this thesis can be separated in two parts. Chapters 2 to 4 are related to the first objective, and Chapters 5 and 6 to the second.

Chapter 2 introduces an ambulatory measurement system for assessing the dynamics of ankle and foot, which integrates the measurement of GRF with the measurement of human movement. Two 6D force/moment sensors are mounted beneath the heel and the forefoot of an orthopaedic sandal with two inertial sensors rigidly attached to the force/moment sensors. The instrumented shoe is used to assess GRF, CoP, joint moments, joint powers and the movement of foot and ankle. Data obtained from a healthy subject was used to evaluate the accuracy by comparison with an optical position measurement system as a reference.

The instrumented shoe is used in Chapter 3 to assess foot placement during walking. Lateral foot placement and stride length were estimated for a group of eight healthy subjects who walked with eyes open and eyes closed. For validation, the ambulatory measurement system was compared to an optical position measurement system.

In Chapter 4, a method to continuously estimate the displacement of the Center of Mass (CoM) using the instrumented shoe is proposed. The CoM is an imaginary point at which the total body mass can be assumed to be concentrated, and is a crucial variable for balance assessment. The displacement of the CoM is estimated by fusing low-pass filtered CoP data with high-pass filtered double integrated CoM acceleration. The CoM estimation using the instrumented shoe is compared to CoM estimation using an optical reference system, based on the segmental kinematics method for a group of seven stroke patients.

Chapter 5 presents a stochastic magnetic measurement model to predict the magnetic field generated by a source coil at the location of the sensor. The accuracy of the model is evaluated by experiments, and possible sources of error are analyzed and discussed.

The stochastic magnetic measurement model is fused with inertial sensing using an Extended Kalman Filter (EKF) structure for relative position and orientation estimation in Chapter 6. Inertial sensors are used to estimate change of position and orientation between magnetic updates. The EKF estimates the uncertainty associated with the position and orientation and decides to perform a magnetic update only if the uncertainty exceeds a predefined threshold. Furthermore, only the coil with the highest contribution to the reduction of the uncertainty is actuated.

Finally, Chapter 7 presents a general discussion that concludes this thesis.

2

Ambulatory Assessment of Ankle and Foot Dynamics

H.M. Schepers, H.F.J.M. Koopman, and P.H. Veltink
IEEE Transactions on Biomedical Engineering, 54(5):895-902, 2007

Abstract

Ground reaction force (GRF) measurement is important in the analysis of human body movements. The main drawback of the existing measurement systems is the restriction to a laboratory environment. This study proposes an ambulatory system for assessing the dynamics of ankle and foot, which integrates the measurement of the GRF with the measurement of human body movement. The GRF and the center of pressure (CoP) are measured using two 6D force/moment sensors mounted beneath the shoe. The movement of the foot and the lower leg is measured using three miniature inertial sensors, two rigidly attached to the shoe and one to the lower leg. The proposed system is validated using a force plate and an optical position measurement system as a reference. The results show good correspondence between both measurement systems, except for the ankle power. The root mean square (rms) difference of the magnitude of the GRF over 10 evaluated trials was 0.012 ± 0.001 N/N (mean $\pm$ standard deviation), being 1.1 ± 0.1 % of the maximal GRF magnitude. It should be noted that the forces, moments, and powers are normalized with respect to body weight. The CoP estimation using both methods shows good correspondence, as indicated by the rms difference of 5.1 ± 0.7 mm, corresponding to 1.7 ± 0.3 % of the length of the shoe. The rms difference between the magnitudes of the heel position estimates was calculated as 18 ± 6 mm, being 1.4 ± 0.5 % of the maximal magnitude. The ankle moment rms difference was 0.004 ± 0.001 Nm/N, being 2.3 ± 0.5 % of the maximal magnitude. Finally, the rms difference of the estimated power at the ankle was 0.02 ± 0.005 W/N, being 14 ± 5 % of the maximal power. This power difference is caused by an inaccurate estimation of the angular velocities using the optical reference measurement system, which is due to considering the foot as a single segment. The ambulatory system considers separate heel and forefoot segments, thus allowing an additional foot moment and power to be estimated. Based on the results of this research, it is concluded that the combination of the instrumented shoe and inertial sensing is a promising tool for the assessment of the dynamics of foot and ankle in an ambulatory setting.

2.1 Introduction

Analysis of human body movement is commonly done in so-called 'gait laboratories'. In these laboratories, body movement is measured by a camera system using optical markers, the ground reaction force (GRF) using a force plate fixed in the floor, and the muscle activity using EMG. From the body movements and ground reaction forces, joint moments and powers can be estimated by applying inverse dynamics methods [44, 45, 46, 47]. The main disadvantage of such a measurement system is that it is restricted to the gait laboratory. Therefore research is required to find ways for performing these measurements outside the gait laboratory, for example in a doctor's practice, at the working place, or at home.

The measurement of the GRF using a force plate has several drawbacks. First, the subjects are required to place their feet completely on the force plates in order to perform a correct force measurement. This poses a restriction on the natural gait pattern. Second, only one or two steps can be measured during a trial, so many successive trials are usually required. Third, it is impossible to distinguish the GRF acting on each foot when standing with both feet on a single plate, as only the total GRF is registered. Finally, the force plate is fixed in the gait laboratory, which means the measurements cannot be performed in everyday life situations. Several research groups are attempting to overcome these limitations by constructing a 'force plate' attached to the subject. A first attempt for an ambulatory measurement of the GRF was made by Kljajić and Krajnik [42], who described a system to measure the vertical component of the GRF and its distribution using force transducers beneath the shoe. The GRF has also been measured using pressure insoles [48, 49, 39]. However, like the system of Kljajić and Krajnik, these insoles only yielded the vertical component of the GRF. Therefore additional knowledge was needed to estimate the shear components. Forner-Cordero *et al.* [39] solved this by using knowledge of body movements. Another solution was given by Savelberg and De Lange [40] who used pressure insoles in combination with an artificial neural network to achieve a relationship between pressure patterns and the shear component of the GRF. A miniature triaxial piezoelectric transducer measuring three orthogonal stress components inside a shoe was described by Razian and Pepper [38]. However, an independent and complete measurement of the GRF is preferred. An example was given by Roland *et al.* [50], who described the design and demonstration of a dynamometric horseshoe for measuring GRFs of horses during racing conditions. Chao and Yin [43] presented a novel shoe-shape structure, capable of mounting two 6D force/moment sensors placed in the front part and rear part of that structure. This similar principle was proposed by Veltink *et al.* [36] using orthopaedic shoes equipped with 6D force/moment sensors (Figure 2.1). In the design of Chao and Yin [43] the movement is constrained by a hinge, positioned between the front and rear sensor, while the design of Veltink *et al.* [36] allows distributed deformation of the shoe sole. An essential component still missing in this design is the measurement of force sensor movement. In contrast to force plate measurements, the force sensors follow the movement of the foot, which means the orientation of the force sensors has to be measured for an accurate estimation of the GRF.

Measuring body movement by a motion tracking system, using reflective markers attached to the body, offers accurate position tracking of body segments. However, this system has several drawbacks. First, the line of sight from camera to marker is often blocked by the subject, resulting in incomplete data. Second, these measurements are restricted to the laboratory environment also, and thus cannot be performed in everyday life situations. An alternative is to use inertial sensors consisting of accelerometers and gyroscopes [28, 15, 51, 52]. These sensors do not suffer from the above mentioned problems. However, obtaining the positions

Figure 2.1: *Instrumented shoe with force transducers, and inertial sensors.*

and orientations of a sensor by integration will introduce integration errors (drift). These errors can be avoided by using zero velocity updates [53], and knowledge of position and orientation [54, 55].

The objective of this study is to assess the ankle and foot dynamics by integrating the measurement of GRFs and body movement using an ambulatory system. The GRFs are measured using the instrumented shoes of Veltink *et al.* [36], whereas the movement of foot and ankle is measured using inertial sensors [54, 56, 57]. The system is validated using a force plate and an optical position measurement system as a reference.

2.2 Methods

As mentioned in the introduction, this paper extends the work of Veltink *et al.* [36] by estimating the dynamics at the ankle and the foot. This section first describes the calculation of the moment and the power at the ankle and the foot. Subsequently, the calculation of the GRF and Center of Pressure (CoP) from the sensor signals is described, and the methods for estimation of the 3D foot position and orientation are presented. Finally, the experimental methods are described.

2.2.1 Moment and Power Calculation

To obtain a full biomechanical analysis, it is desirable that the joint forces, moments and powers are estimated. In this research, a first attempt is made by estimating the force, moment, and power at the ankle. For calculation purposes, all vectors have to be expressed in the same coordinate system, being the global coordinate system. The origin and orientation of this global coordinate system Ψ_g are renewed for each foot placement to coincide with the heel sensor coordinate system, when the heel is flat on the ground. Positive x is in the direction of gait; positive z is directed upward; and positive y is perpendicular to the x and z direction such that the result is an orthogonal right-handed coordinate system. All measured signals are expressed in a sensor fixed coordinate system Ψ_s. This means that the measured signals have to be transformed to the global coordinate system Ψ_g.

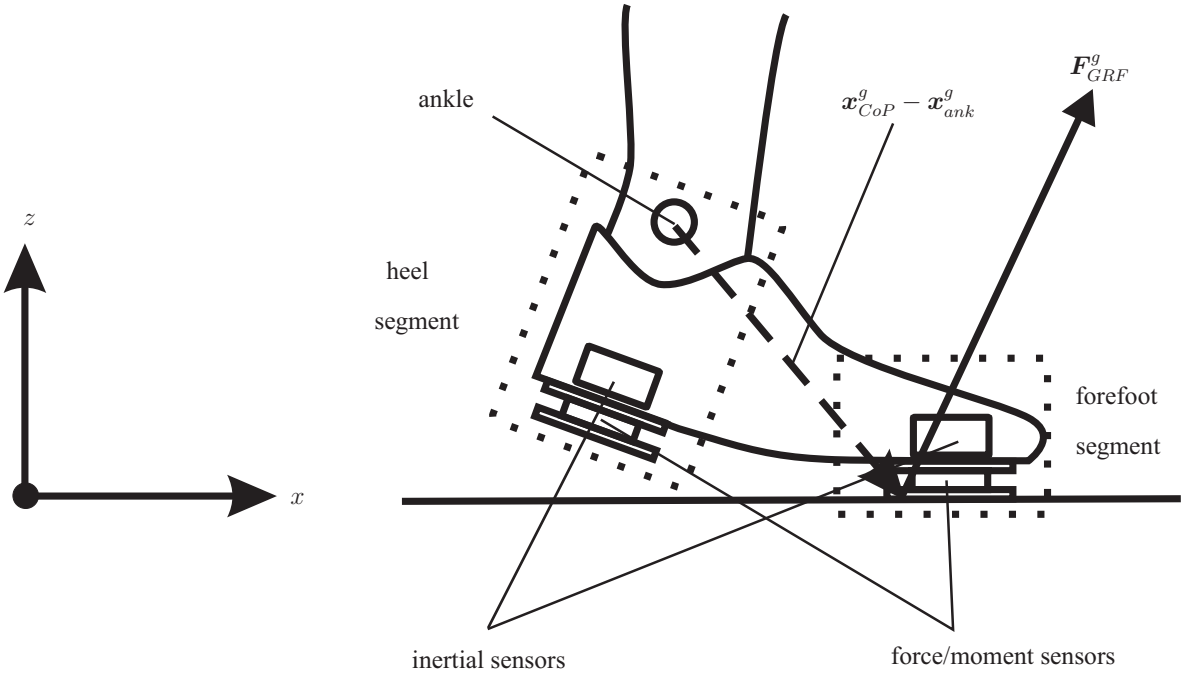

Figure 2.2: *Schematic drawing of the instrumented shoe during the stance phase.*

A general change of coordinates between two coordinate systems (Ψ_i an Ψ_j) is denoted by:

$$\boldsymbol{H}^j_i = \begin{pmatrix} \boldsymbol{R}^j_i & \boldsymbol{p}^j_i \\ 0^T_3 & 1 \end{pmatrix}, \tag{2.1}$$

where $\boldsymbol{R}^j_i$ is a rotation matrix representing the change of coordinates between frame Ψ_i and Ψ_j rotated with respect to each other, and $\boldsymbol{p}^j_i$ is a displacement vector representing the coordinates of the origin of frame Ψ_i expressed in frame Ψ_j. The columns of the rotation matrix $\boldsymbol{R}^j_i$ are the coordinates of the unit axes of frame Ψ_i expressed in frame Ψ_j:

$$\boldsymbol{R}^j_i = \begin{pmatrix} \boldsymbol{X}^j_i & \boldsymbol{Y}^j_i & \boldsymbol{Z}^j_i \end{pmatrix}. \tag{2.2}$$

This change of coordinates can for example be used to describe the position and orientation of a sensor, with attached frame Ψ_s, relative to a reference frame Ψ_g, by using $\boldsymbol{H}^g_s$, $\boldsymbol{R}^g_s$, and $\boldsymbol{p}^g_s$.

A schematic drawing of the instrumented shoe is shown in Figure 2.2, where the foot has been divided in two segments. The force of each segment is measured by a force sensor, and the movement of each segment by an inertial sensor. The moment at the ankle joint $\boldsymbol{M}^g_{ank}$ in global coordinates is calculated using the equations of motion [58], and the rotation matrix $\boldsymbol{R}^g_s$:

$$\begin{aligned} \boldsymbol{M}^g_{ank} = &- \left(\boldsymbol{x}^g_{CoP} - \boldsymbol{x}^g_{ank}\right) \times \boldsymbol{F}^g_{GRF} \\ &+ \left(\boldsymbol{x}^g_{ft} - \boldsymbol{x}^g_{ank}\right) \times m_{ft}\boldsymbol{s}^g_{ft} + \boldsymbol{R}^g_s \frac{d}{dt}\left(\boldsymbol{I}_{ft}\boldsymbol{\omega}^s_{ft}\right), \end{aligned} \tag{2.3}$$

where the position of the ankle, the CoP, and the center of mass of the foot are given by $\boldsymbol{x}^g_{ank}$, $\boldsymbol{x}^g_{CoP}$, and $\boldsymbol{x}^g_{ft}$ respectively. The mass of the foot is given by m_{ft}, the moment of inertia of the foot by $\boldsymbol{I}_{ft}$, the angular velocity of the foot by $\boldsymbol{\omega}^s_{ft}$, and the acceleration including gravity, expressed in global coordinates, by $\boldsymbol{s}^g_{ft} = \boldsymbol{a}^g_{ft} - \boldsymbol{g}^g$. Since the GRF contribution is considerably

larger than the contribution of the inertial terms, the contribution of the inertial terms will be neglected [58]. This means (2.3) reduces to:

$$\boldsymbol{M}^g_{ank} = -\left(\boldsymbol{x}^g_{CoP} - \boldsymbol{x}^g_{ank}\right) \times \boldsymbol{F}^g_{GRF}. \tag{2.4}$$

The ankle power P^g_{ank} is calculated by the product of the ankle moment $\boldsymbol{M}^g_{ank}$ and the angular velocity at the ankle $\boldsymbol{\omega}^g_{ank}$, which is the difference between the angular velocity of the heel segment of the foot $\boldsymbol{\omega}^g_{hl}$ and the angular velocity of the lower leg $\boldsymbol{\omega}^g_{lleg}$:

$$P^g_{ank} = \boldsymbol{M}^g_{ank} \cdot \boldsymbol{\omega}^g_{ank} = \boldsymbol{M}^g_{ank} \cdot \left(\boldsymbol{\omega}^g_{hl} - \boldsymbol{\omega}^g_{lleg}\right). \tag{2.5}$$

Since the foot has been modeled as two segments (Figure 2.2), the heel and forefoot can move with respect to each other. This means a foot moment, and foot power are generated as well. The foot moment $\boldsymbol{M}^g_{ft}$, and power $\boldsymbol{P}^g_{ft}$ are calculated as:

$$\begin{aligned} M^g_{ft} &= -\left(\boldsymbol{x}^g_{CoP} - \boldsymbol{x}^g_{ft}\right) \times \boldsymbol{F}^g_{ff}. \\ P^g_{ft} &= \boldsymbol{M}^g_{ft} \cdot \boldsymbol{\omega}^g_{ft} = \boldsymbol{M}^g_{ft} \cdot \left(\boldsymbol{\omega}^g_{hl} - \boldsymbol{\omega}^g_{ff}\right), \end{aligned} \tag{2.6}$$

where $\boldsymbol{x}^g_{ft}$ denotes the position of an imaginary hinge point assumed to be present between the two foot segments, and $\boldsymbol{F}^g_{ff}$ the GRF measured by the forefoot sensor. The angular velocity of the foot is denoted by $\boldsymbol{\omega}^g_{ft}$, which is the difference between the angular velocities of the heel $\boldsymbol{\omega}^g_{hl}$, and the forefoot $\boldsymbol{\omega}^g_{ff}$.

2.2.2 GRF and CoP Calculation

As mentioned in the introduction, the GRF is measured by two 6D force/moment sensors under the heel and the forefoot. The forces and moments measured by the sensors should be transformed to global coordinates, and combined. The transformation of the forces and moments measured by a force sensor with attached coordinate frame Ψ_{s1} to the global coordinate frame Ψ_g is achieved using (2.1), and (2.2):

$$\begin{aligned} \boldsymbol{F}^g_{s1} &= \boldsymbol{R}^g_{s1}\boldsymbol{F}^{s1} \\ \boldsymbol{M}^g_{s1} &= \boldsymbol{R}^g_{s1}\boldsymbol{M}^{s1} + \boldsymbol{p}^g_{s1} \times \boldsymbol{F}^{s1}. \end{aligned} \tag{2.7}$$

The GRF $\boldsymbol{F}^g_{GRF}$, and the moment $\boldsymbol{M}^g_{GRF}$ acting on the foot are found by summing the contributions of each force sensor. The moment around the x and y-axes can be represented using the CoP. The CoP denotes the point on the contact surface between the instrumented shoe and the ground, where the moments around the horizontal axes are zero. This means the moment measured by the force sensors, expressed in the global coordinate frame Ψ_g, can be described by: $\boldsymbol{M}^g_{GRF} = \boldsymbol{x}^g_{CoP} \times \boldsymbol{F}^g_{GRF}$. Solving this equation for $\boldsymbol{x}^g_{CoP}$, and excluding the moment around the z-axis results in:

$$\boldsymbol{F}^g = \begin{pmatrix} F^g_x \\ F^g_y \\ F^g_z \end{pmatrix} \quad \boldsymbol{x}^g_{CoP} = \begin{pmatrix} -\frac{M^g_y}{F^g_z} \\ \frac{M^g_x}{F^g_z} \\ 0 \end{pmatrix} \quad \boldsymbol{M}^g = \begin{pmatrix} 0 \\ 0 \\ M^g_z \end{pmatrix} \tag{2.8}$$

It should be noted that the z-component of the CoP is zero, since the CoP must be on the ground. Besides that, the subscript $_{GRF}$ has been omitted for clarity.

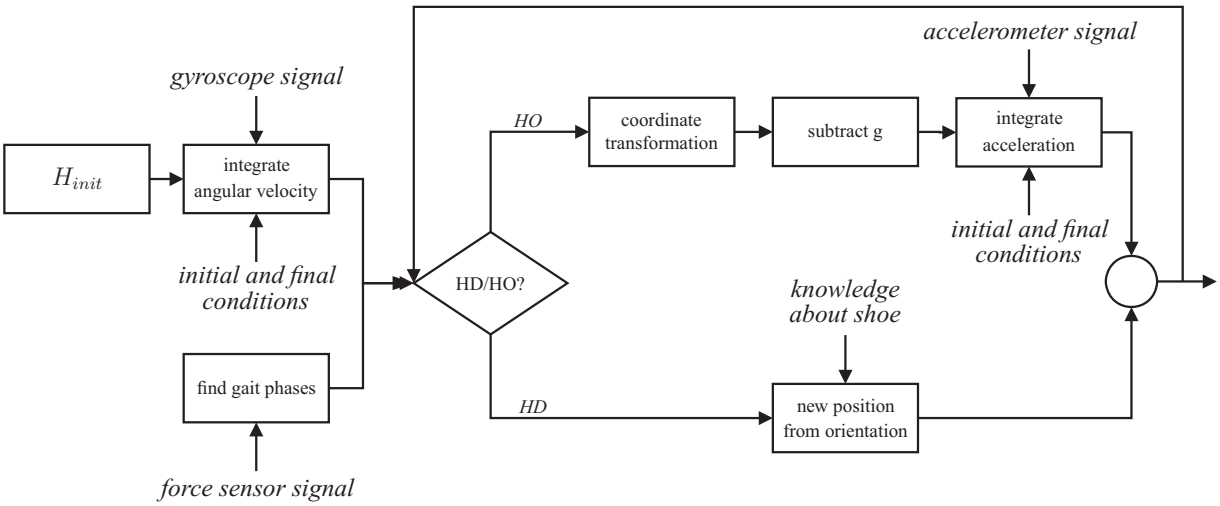

Figure 2.3: *Flowchart of the integration algorithm to obtain position and orientation of a stride (*HO = *heel off,* HD = *heel down).*

2.2.3 3D Foot Position and Orientation Estimation

For the coordinate transformation from sensor to global coordinates, the transformation matrix $\boldsymbol{H}_s^g$ has to be calculated (Section 2.2.1). This means the relative 3D position and orientation of the sensors have to be estimated, which is achieved by combining the signals of an inertial sensor consisting of three accelerometers, and three rate gyroscopes. The estimation requires integration of the angular velocity $\boldsymbol{\omega}$, measured with the rate gyroscopes, to orientation, and double integration of the acceleration $\boldsymbol{a}$, measured with the accelerometers, to position in global coordinates. The integration of the angular velocity $\boldsymbol{\omega}$ to orientation $\boldsymbol{R}_s^g$, is performed by solving the differential equation [59]:

$$\dot{\boldsymbol{R}}_s^g = \boldsymbol{R}_s^g \tilde{\boldsymbol{\omega}}_s^{s,g}, \tag{2.9}$$

where $\tilde{\boldsymbol{\omega}}_s^{s,g}$ is the skew-symmetric matrix of the angular velocity of frame Ψ_s with respect to Ψ_g, expressed in Ψ_s:

$$\tilde{\boldsymbol{\omega}} = \begin{pmatrix} 0 & -\omega_z & \omega_y \\ \omega_z & 0 & -\omega_x \\ -\omega_y & \omega_x & 0 \end{pmatrix} \tag{2.10}$$

In general, position estimation is not possible without additional sources, due to the integration drift of the accelerometers. However, during walking certain initial and final conditions can be assumed [54] (e.g. zero velocity update [53], vertical position of foot equal at each stride), and the integration time is limited (about one second). In addition, the relative position of a sensor touching the ground can be estimated from the orientation data separately, instead of straightforward integration of the accelerometer signals.

The algorithm for the relative 3D foot position and orientation estimation of each stride is based on these principles, and shown in Figure 2.3. The determination of the start and the end of a stride is based on force sensor information. The angular velocity $\boldsymbol{\omega}$ is integrated (2.9), and the initial and final conditions are used for drift compensation. The algorithm checks for heel down (HD) or heel off (HO), based on force sensor information. On the one hand, when the heel force sensor touches the ground (HD), the motion of the shoe is constrained, and the position determination is based on the orientation and knowledge about the distance between the force sensors under the shoe. During this phase, the absolute distance between the sensors

is assumed to be constant, and the position of the sensors can be extracted from the last column of the transformation matrix (2.1). On the other hand, when the heel sensor does not touch the ground (HO), the position is determined by straightforward integration of the accelerometer signal. First, the estimated orientation is used to transform the measured acceleration $\boldsymbol{s}$ from sensor coordinates to global coordinates, and the gravitational acceleration $\boldsymbol{g}$ is subtracted to result in the acceleration $\boldsymbol{a}$ of the sensor. Subsequently, to obtain the position of the sensors, this acceleration has to be integrated twice assuming the initial and final conditions to avoid drift, as shown by (2.11).

$$\begin{aligned}
\boldsymbol{v}^-(t) &= \boldsymbol{v}_0 + \int_{t_s}^{t} \boldsymbol{a}(\tau)d\tau \\
\boldsymbol{v}^+(t) &= \boldsymbol{v}^-(t) - \frac{t-t_s}{t_e-t_s}\boldsymbol{v}^-(t_e) \\
\boldsymbol{x}^-(t) &= \boldsymbol{x}_0 + \int_{t_s}^{t} \boldsymbol{v}(\tau)d\tau \\
x_z^+(t) &= x_z^-(t) - \frac{t-t_s}{t_e-t_s}x_z^-(t_e);\ t = t_s, \ldots, t_e,
\end{aligned} \tag{2.11}$$

where $t_s, \ldots, t_e$ denotes the time interval when the heel sensor does not touch the ground. A minus superscript denotes the estimation of the signal before the drift compensation, whereas a plus superscript denotes the estimation of the signal after the drift compensation has been applied. It should be noted that the initial conditions $\boldsymbol{v}_0$ and $\boldsymbol{x}_0$ are zero, since the global coordinate system is renewed for each foot placement, as mentioned in Section 2.2.1.

2.2.4 Experimental Methods

During the experiments, a healthy subject wearing instrumented shoes (total mass 68 kg), was asked to walk repeatedly over an AMTI force plate. The instrumented shoes consisted of standard orthopaedic sandals equipped with two 6D force/moment sensors (ATI-Mini45-SI-580-20, supplier: Schunk GmbH & Co. KG) under the heel and forefoot, as shown in Figure 2.1. Each sensor was enclosed between two aluminum mounting plates and carbon plates to assure rigidity and easy mounting. Furthermore, a thin piece of rubber provided friction between the lower carbon plates and the ground. The sole of the sandal between the sensors was not adapted, which resulted in a remaining flexibility at this part of the sole. Each force sensor had a miniature inertial sensor (Xsens Technologies B.V.) attached to it, for the estimation of position and orientation. The position of the ankle was determined by assuming a fixed position in the heel segment, and using the information from the inertial sensors. To estimate the power at the ankle, the angular velocity at the ankle should be known. Since this angular velocity is given by the difference between the angular velocities of the heel and the lower leg, a third inertial sensor was attached to the lower leg to measure its angular velocity. The combination of an instrumented shoe and inertial sensors was compared to a reference measurement system consisting of an AMTI force plate and an optical position measurement system (Vicon, Oxford Metrics).

At the start of a measurement, the inertial sensors had to be calibrated with respect to the position and orientation of the force sensors. For the inertial sensors attached to the force sensors, this was simply done by measuring the distances between the inertial sensors and the force sensors, and knowing the initial orientation with respect to each other. For the inertial sensor on the lower leg, this was done by a sensor to segment calibration. The z direction

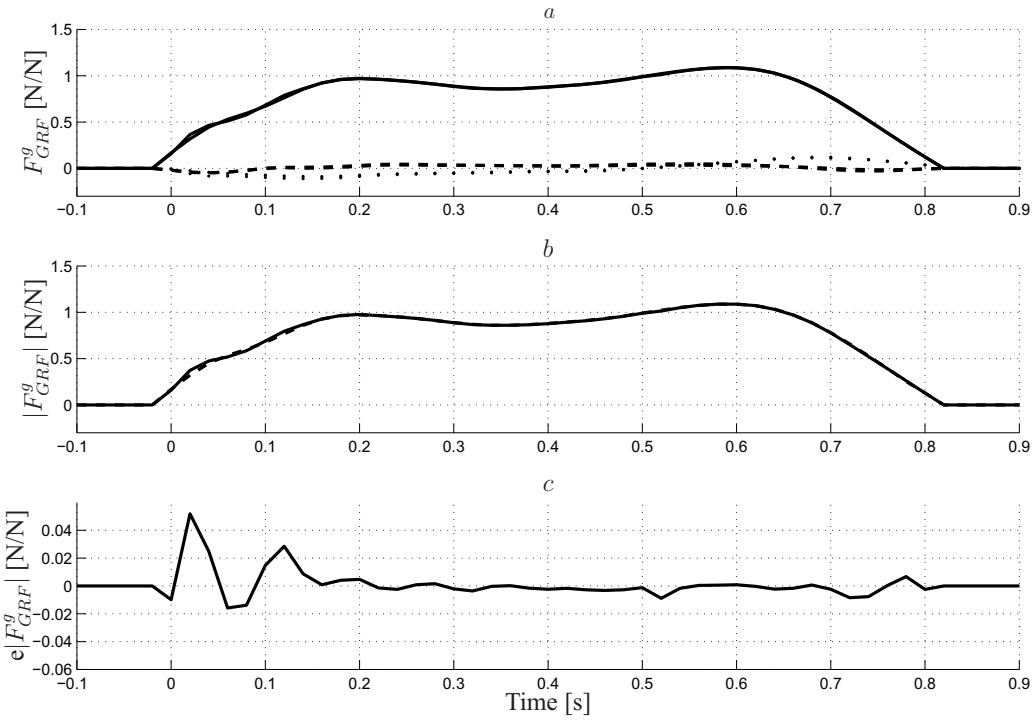

Figure 2.4: *GRF measured by the instrumented shoe and the force plate. (a) Components of the GRF (x: dotted; y: dashed; z: solid). (b) Magnitude of the complete GRF measured by the instrumented shoe (solid), and the force plate (dashed). (c) Error signal.*

was determined by measuring the (gravitational) acceleration while keeping the lower leg in an upright position. The y-direction was determined by bending the knee. The x direction was determined using the y and z direction, in order to obtain an orthogonal right-handed coordinate system. The position of the ankle in the heel segment was determined by measuring the distance between the ankle and the heel sensor.

Each of the ten evaluated trials consisted of four strides, one of which was on the force plate. The analogue data from the force plate and force sensors were acquired at a sample rate of 1000 Hz, the 3D marker data at 50 Hz, and the data from the inertial sensors at 50 Hz. All data were low-pass filtered by applying a second order Butterworth filter, both forward and reverse at a cutoff frequency of 15 Hz. The synchronization between the inertial sensor system and Vicon was done by maximizing the correlation between the angular velocities of the lower leg estimated with both systems. Subsequently, all signals were resampled to a frequency of 50 Hz, and possible gaps in the Vicon data were spline-interpolated prior to filtering. The voltages from the force sensors and the force plate were converted to forces by applying the calibration tables supplied by the manufacturer.

2.3 Results

The three components of the measured GRF of a representative trial are shown in Figure 2.4(a). It should be noted that the forces, moments, and powers are normalized with respect to body weight. The magnitude of the complete GRF is shown in Figure 2.4(b), and the error between

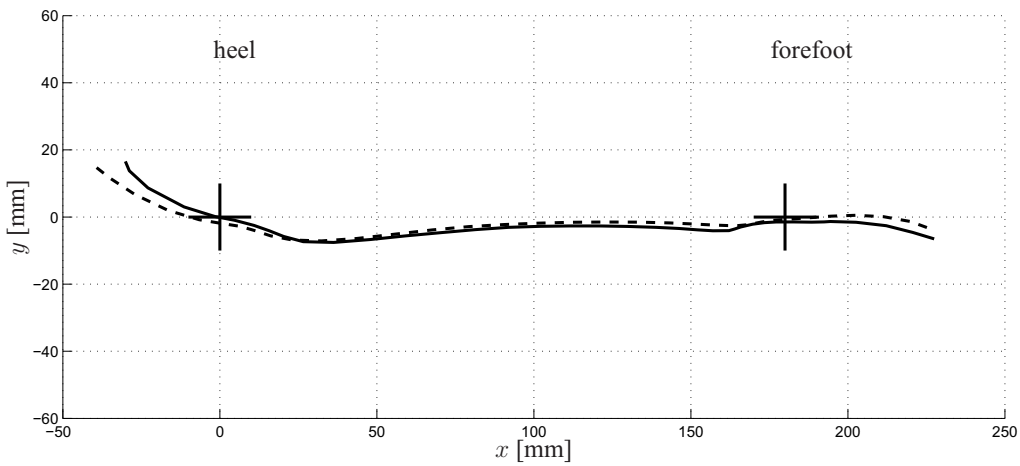

Figure 2.5: *CoP of the instrumented shoe (solid) and the force plate (dashed) expressed in global coordinate system. The center of each force sensor is indicated by the black cross.*

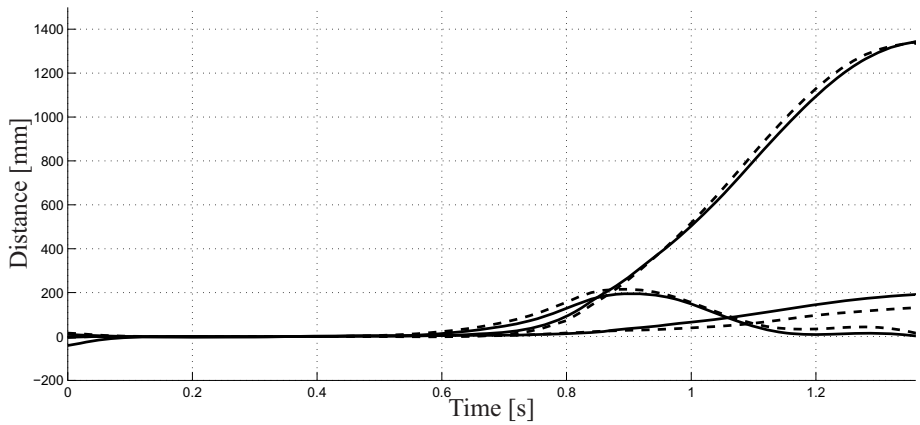

Figure 2.6: *Position of the heel sensor estimated using instrumented shoes and inertial sensors (solid), and force plate and Vicon (dashed).*

the magnitudes in Figure 2.4(c). The signals show good correspondence, which is confirmed by Figure 2.4(c), and the root mean square (rms) difference over 10 evaluated trials of 0.012 ± 0.001 N/N (mean $\pm$ standard deviation), being 1.1 ± 0.1 % of the maximal GRF magnitude. The rms difference of the estimates of the horizontal component of the GRF was 0.017 ± 0.008 N/N, which corresponds to 1.6 ± 0.8 % of the maximal GRF magnitude, or 16 ± 8 % of the maximal horizontal component of the GRF. A separate analysis of each horizontal component results for the x direction in an rms difference of 0.019 ± 0.008 N/N, being 1.8 ± 0.8 % of the maximal GRF magnitude, or 18 ± 8 % of the maximal x component. For the y direction in an rms difference of 0.007 ± 0.002 N/N, being 0.7 ± 0.2 % of the maximal GRF magnitude, or 15 ± 5 % of the maximal y component. The estimation of the position of the CoP using the instrumented shoes, as well as the force plate is shown in Figure 2.5. The trajectories agree well, resulting in an rms difference between both methods of 5.1 ± 0.7 mm, corresponding to 1.7 ± 0.3 % of the length of the shoe. The estimation of the position of the heel force sensor using both methods is shown in Figure 2.6. The rms difference between the magnitudes of the position estimates using both methods was calculated as 18 ± 6 mm, being 1.4 ± 0.5 % of the maximal magnitude.

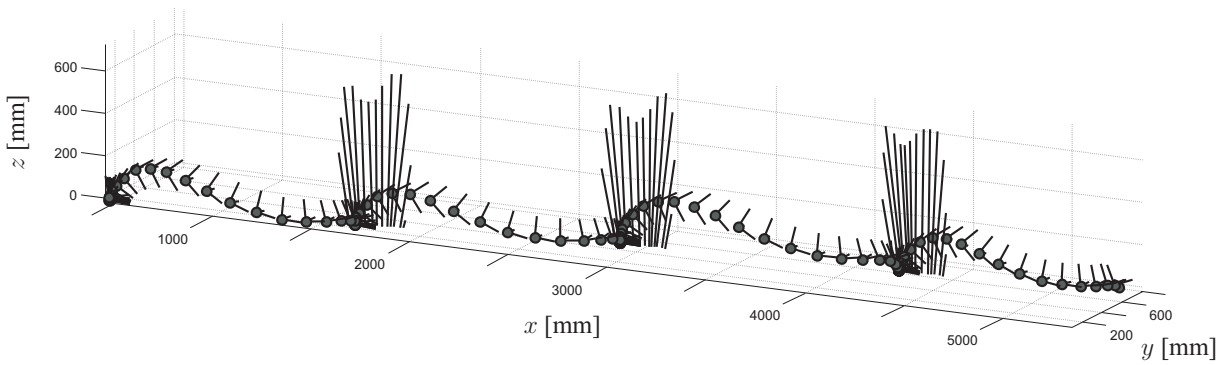

Figure 2.7: *CoP, GRF, position, and orientation of the heel sensor during several strides. The CoP and GRF of three strides are indicated by the lines pointing upwards. The position of the heel sensor is indicated by the dots, the corresponding orientation by the three lines representing the heel sensor coordinate axes.*

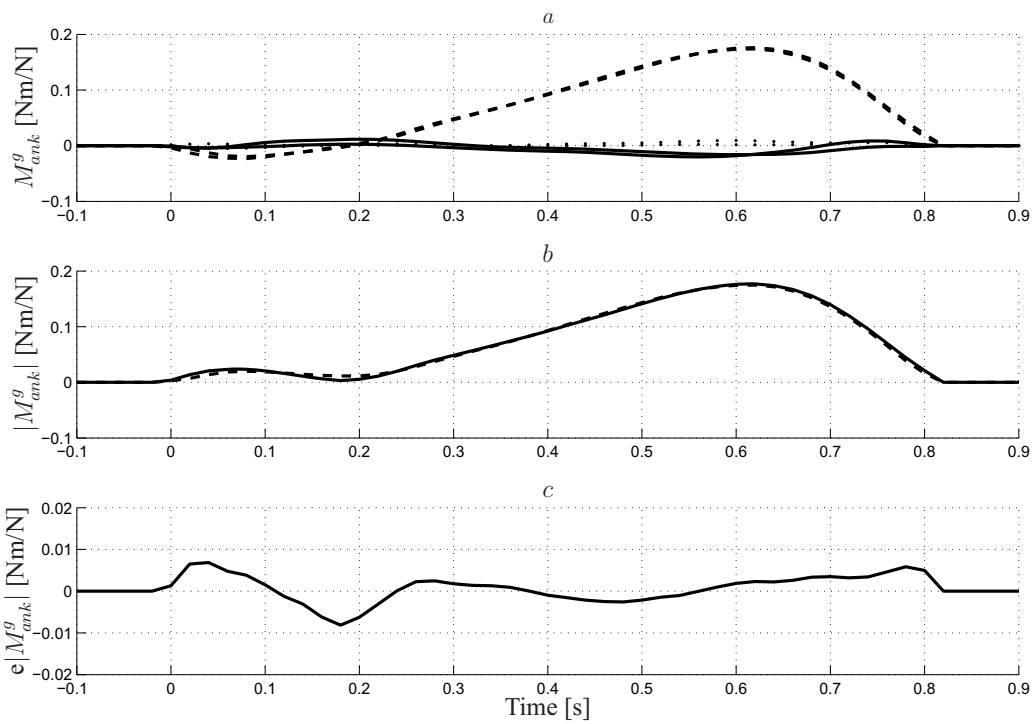

Figure 2.8: *Ankle moment estimated using instrumented shoes and inertial sensors, and force plate and Vicon. (a) Components of the ankle moment (x: dotted; y: dashed; z: solid). (b) Magnitude of the ankle moment measured by the instrumented shoe (solid), and the force plate (dashed). (c) Error signal.*

An integration of the estimated CoP, GRF, the position and orientation of the heel sensor is shown in Figure 2.7. The figure indicates the possibility to measure several strides during a single measurement. It is easy to recognize the characteristic M-shape of the GRF, as shown in Figure 2.4(b).

A comparison of the moment around the ankle is shown in Figure 2.8. Figure 2.8(a) shows the three components of the estimated ankle moment, using Vicon & force plate as well as

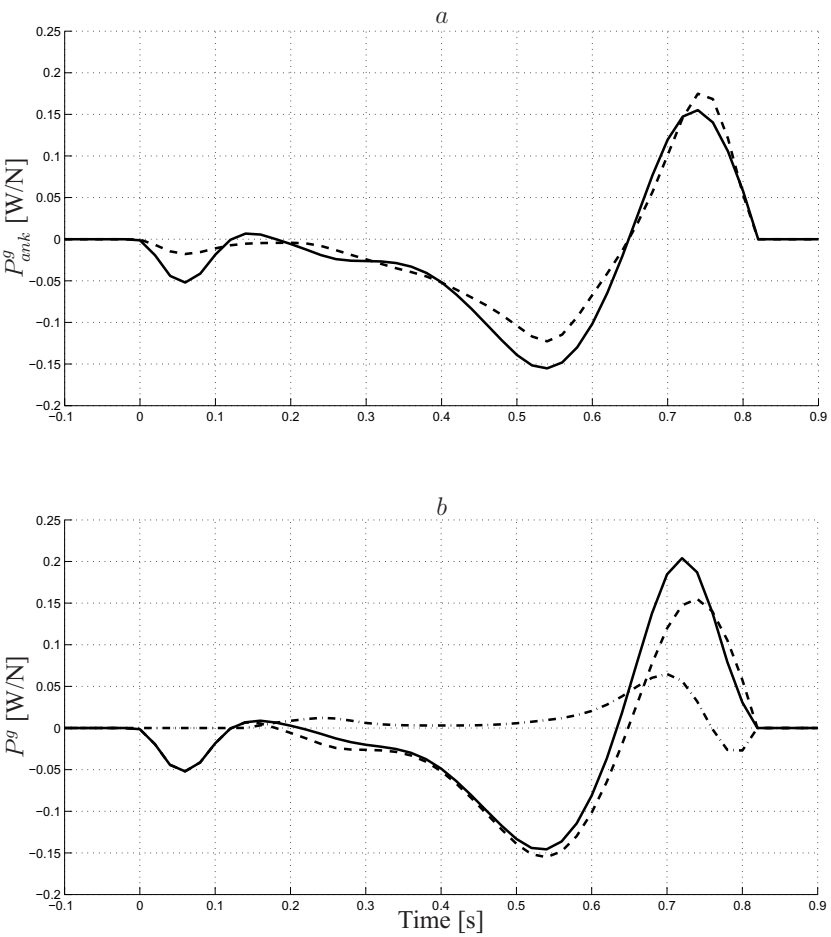

Figure 2.9: *Estimated Power. (a) Ankle power using instrumented shoes and inertial sensors (dashed), and force plate & Vicon (solid). (b) Total power using instrumented shoes and inertial sensors (solid) calculated by the sum of ankle power (dashed), and foot power (dashed/dotted).*

inertial sensors & instrumented shoes. The magnitude of the estimated ankle moment is shown in Figure 2.8(b), and the error between the magnitudes in Figure 2.8(c). The rms difference over the 10 trials was 0.004 ± 0.001 Nm/N, being 2.3 ± 0.5 % of the maximal magnitude. The estimated power at the ankle is shown in Figure 2.9(a). The rms difference over the 10 evaluated trials was 0.02 ± 0.005 W/N, being 14 ± 5 % of the maximal power. Since the ankle moment shows good correspondence (Figure 2.8), this relatively large difference is caused by an error in the estimation of the angular velocity (2.5), which is shown in Figure 2.10. It should be noted that the x and z direction of the angular velocities are not shown, since their magnitude is small compared to the y direction. Moreover, merely the difference between heel and lower leg angular velocity is shown for clarity. The rms differences of the angular velocities are 0.85 ± 0.10 rad/s, 0.53 ± 0.11 rad/s, and 0.89 ± 0.07 rad/s for the heel, lower leg, and the difference between them respectively, which corresponds to 14 ± 2 %, 19 ± 4 %, and 19 ± 3 % of the maximal angular velocity. During push-off the ankle moment is maximal, which means a small error in the angular velocity during push-off gives rise to significant errors in the calculated ankle power, as illustrated by Figure 2.9(a). Most probably, the angular velocity error is caused by an inaccurate estimation using Vicon for two reasons. Firstly, the Vicon

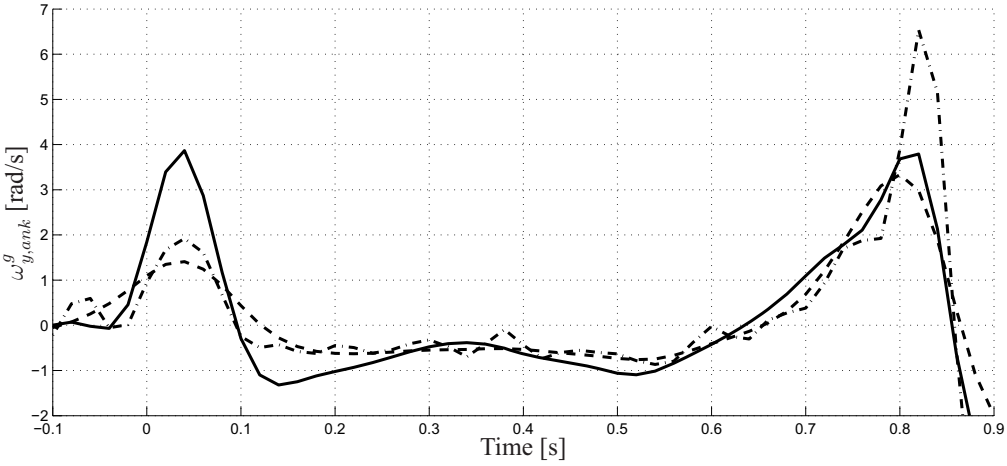

Figure 2.10: *Ankle angular velocity estimated using instrumented shoes and inertial sensors (solid), force plate and Vicon low-pass filtered using a second order Butterworth filter, both forward and reverse at a cutoff frequency of 5 Hz (dashed), and force plate and Vicon without filtering (dashed/dotted).*

estimation requires a differentiation of marker position, whereas the inertial sensors measure the angular velocity directly using gyroscopes. The differentiation requires low-pass filtering to reduce the effect of high-frequency noise, which influences the results considerably. The effect is shown in Figure 2.10, where the signal without filtering is rather noisy with a peak at toe off (dashed-dotted), whereas the low-pass filtered signal using a second order Butterworth filter, both forward and reverse at a cutoff frequency of 5 Hz (dashed) results in leakage in the time domain. This leakage becomes clear at the start and the end of the stance phase, where the peaks are spread out over time. In contrast, the angular velocity measurement by the gyroscopes yields a smooth signal, while allowing a sufficient bandwidth to represent the angular velocity peak between heel and subsequent forefoot ground contact. Secondly, in the Vicon analysis the foot is modeled as one rigid segment, whereas this analysis uses two segments (Figure 2.2). The wrong assumption of one rigid segment is confirmed by the relative change of distance between the markers positioned on the shoe, being 7 ± 1 mm rms during stance. It should be noted that the relative distance between the markers on the heel and the ankle changes as well (7 ± 1 mm rms during stance), which is caused by deformation of the shoe cushioning, along with movement of the foot inside the shoe.

The relative movement between the two foot segments causes a foot moment and power as described by (2.6). The ankle power, the foot power, and their sum are shown in Figure 2.9(b). For the calculation of the foot moment and power, an imaginary point of rotation was assumed at approximately the head of the first metatarsal bone. It should be noted that no reference is available for this signal, since the foot is assumed as one rigid segment in the Vicon analysis as is commonly done in such analysis [45].

2.4 Discussion

Integration of body movement and GRF sensing, using the ambulatory setup proposed in the current study, yields a comprehensive analysis of ankle and foot dynamics including heel and

forefoot movement, as well as ankle and foot moments and powers. The proposed measurement system is an extension of the system proposed by Veltink *et al.* [36]. Like Veltink's system, the GRF of a foot was measured using two 6D force/moment sensors. In addition, the movement of foot and ankle was measured, using two inertial sensors. The angular velocity of the lower leg was measured by a third inertial sensor. The good reproduction of the ankle moment shows the feasibility of the measurement system for inverse dynamics applications problems.

However, the reproduction of the ankle power shows a rather large difference between the two evaluated methods. As described in Section 2.3, the difference is caused by an inaccurate estimation of the angular velocities using Vicon. Standard marker configurations, as used in this research, do not allow the estimation of foot moment and power, since they do not separate the foot into multiple segments. In principle, more elaborate marker configurations could be used on the foot, which would allow foot moment and power to be estimated [60].

The biomechanical model of the foot used in our analysis consists of two segments (Figure 2.2), whereas the reference model used in the Vicon analysis consists of one segment. For the two segments model, an imaginary point of rotation was assumed. In reality, however, the deformation of the foot and the shoe is distributed, and there is no single point of rotation. Therefore the foot model should preferably include distributed deformation. The performance of the reference system can be improved by increasing the sample frequency, or by improving the accuracy of the position measurement, e.g. by using active markers, or by using more markers on the foot to measure the deformation of the foot. Principally, however, it is better to measure angular velocity directly, than to estimate it from position measurements by differentiation.

As mentioned in Section 2.3, the relative distance between the markers on the heel and the ankle changes during stance. This means the assumption that the ankle position is fixed in the heel segment should be reconsidered. However, the estimated ankle moment shows good correspondence and therefore the assumption has not been reconsidered in this research.

The position and orientation estimates reported in this study have been achieved after considering initial and final conditions for a stride. This results in a systematic delay which can not be compensated for by high computational power or efficient implementation of the algorithm. If the foot position and orientation will be computed realtime during a stride, higher errors will occur because of integration drift, which can only be corrected after heel contact and application of the final conditions.

The measurements in this study have been performed in a gait laboratory. The subject walked in a straight line to compare several strides of a trial, and for an easy comparison with the force plate. However, the proposed system allows for ambulatory measurement over any number of consecutive strides including a change of direction while walking.

The design of the instrumented shoe can still be improved. Currently, the sensors are mounted between two aluminum plates, which are rather stiff. However, the sole beneath the sensor does not need to be very stiff for valid measurement of the GRF, and thus some flexibility can be introduced. Moreover, the orientation of the force sensor is constantly measured by the inertial sensors, which allows the design optimization. Another possible optimization of the design would be a reduction of the weight of the sensors and mounting plates, which has not been optimized in the current design. It should be noted that the current design does have a small effect on the walking pattern, which is shown in an evaluation performed by Liedtke *et al.* [61]. In this study, gait on the instrumented shoe was compared to gait on normal, light, and heavy shoes. Gait parameters evaluated were stride length, stride width, maximum lateral foot excursion, stride time, stance time, and double stance time. However, a significant difference was only found in maximal GRF.

The proposed measurement system has been applied to a healthy subject. An important clinical application is the biomechanical analysis of patients having central neurological disorders, or lower leg amputees. It is therefore useful to see if it is possible to apply the proposed measurement system to those patients. Initial tests indicate that the shoes do not impede their walking.

3

Ambulatory Estimation of Foot Placement During Walking Using Inertial Sensors

H.M. Schepers, E.H.F. van Asseldonk, C.T.M. Baten, and P.H. Veltink

Submitted

Abstract

During human walking, foot placement is crucial for maintaining balance. The majority of existing studies describing the assessment of foot placement for consecutive strides use traditional optical position measurement systems, which are restricted to a laboratory environment. To overcome this limitation, this study proposes a method to assess foot placement during walking using an ambulatory measurement system consisting of orthopaedic sandals equipped with force/moment sensors and inertial sensors (accelerometers and gyroscopes). Two parameters, Lateral Foot Placement (LFP) and Stride Length (SL), were estimated for each foot separately during walking with Eyes Open (EO), and with Eyes Closed (EC) to analyze if the ambulatory system was able to discriminate between different walking conditions. Moreover, continuous walking as well as initiation and termination of walking were studied. For validation, the ambulatory measurement system was compared to a reference optical position measurement system (Optotrak). LFP and SL were obtained by integration of inertial sensor signals. To reduce the drift caused by integration, LFP and SL were defined with respect to an average walking path using a predefined number of strides. By varying this number of strides, it was shown that LFP and SL could be best estimated using three consecutive strides. LFP and SL estimated from the instrumented shoe signals and with the reference system showed high correlation for continuous walking (LFP: 0.77 ± 0.10, SL: 0.82 ± 0.08), and for initiation and termination of walking (LFP: 0.84 ± 0.09, SL:0.995 ± 0.001). The percentage difference between both measurement systems for the stride to stride variability was calculated as 7.8 ± 2.6 % for LFP, and 0.67 ± 0.49 % for SL. Additionally, a statistical analysis revealed that the ambulatory system was able to discriminate between the EO and EC condition, like the reference system. It is concluded that the ambulatory measurement system was able to reliably estimate foot placement during walking.

3.1 Introduction

Human walking is often conceived as the motion of two coupled pendula [62]. The double support phase is viewed as a transition from one inverted pendulum to the next. An efficient means to stabilize this essentially unstable system is to adjust foot placement [63]. Assessment of foot placement, especially the variability of foot placement between consecutive strides, reveals important aspects of balance [64].

Traditionally, foot placement is assessed using optical position measurement systems in a gait laboratory [62]. Although these systems are clinically accepted as 'the golden standard', there are several drawbacks. Firstly, the number of consecutive strides that can be measured is limited. This means that variability of gait, involved in balancing the body and walking during varying circumstances, can not be investigated using the existing systems as it requires a larger number of consecutive strides to be measured. Secondly, optical measurement systems suffer from marker visibility problems, since the line of sight from camera to marker is easily blocked due to movement of the subject. Instrumented treadmills provide a solution, allowing many strides to be measured [65, 66, 67]. However, despite the advantages associated to treadmill walking, uncertainty remains regarding the extent to which treadmill walking can be used to mimic overground walking [68]. In addition, the narrow path offered by the treadmill hinders freedom in selection of the trajectory and does not allow measurements during everyday life. These drawbacks stimulated several research groups to start initiatives for performing these measurements outside the laboratory, in an ambulatory environment.

An alternative to the traditional measurement systems is to use inertial (accelerometers and gyroscopes) and magnetic sensors [55, 69, 52]. Although these sensors do not suffer from the drawbacks associated to optical measurement systems or instrumented treadmills, they are not ideal as well. The estimation of position and orientation requires integration of acceleration and angular velocity respectively, which gives rise to inherent drift caused by noise and a fluctuating offset. Moreover, relative positions of sensors with respect to each other can not be estimated using inertial sensing only. However, during walking, the integration drift can be avoided by the use of regular zero velocity updates [70].

Up to the authors' knowledge, foot placement during many strides using an ambulatory measurement system has not been estimated previously. Veltink *et al.* [54] described a 3D inertial sensing system for measuring foot movements during gait in stroke patients using a drop-foot stimulator. The main interest in this study was on the effect of stimulation parameters on foot orientation during the swing phase, not on the assessment of foot position. Although Sabatini *et al.* [56], and Zijlstra and Hof [71] estimated foot movement during several strides, these studies merely considered movement in the sagittal plane, whereas adequate lateral foot placement is also essential in balancing the body. This also holds for the wireless wearable measurement system proposed by Bamberg *et al.* [37]. Bauby and Kuo [64] assessed foot placement variability using magnetic measurement system mounted on a rolling cart which was pushed near the walking subject. This measurement system allows several strides to be assessed, but still the rolling cart with the measurement equipment needs to be near the subject. In Chapter 2, foot movement was estimated under ambulatory conditions using instrumented shoes, but the analysis was limited to single stride, the variation between strides was not assessed.

The current study investigates whether it is possible to estimate foot placement of a single foot, both in forward and lateral direction, during many strides using the inertial sensors of an instrumented shoe allowing gait analysis in an ambulatory environment. The instrumented shoe consists of a pair of orthopaedic sandals with two 6D force/moment sensors beneath the heel and

the forefeet and two inertial sensors rigidly attached to the force/moment sensors (Figure 3.1). The performance of the proposed system is evaluated by a comparison with an optical position measurement system while varying the walking conditions to analyze if the ambulatory system is able to discriminate between different walking conditions.

Figure 3.1: *Picture of the instrumented shoe with force/moment sensors beneath the heel and forefoot and inertial sensors rigidly attached to the force/moment sensors. A thin flexible glass-fiber plate connects both sensors allowing regular flexion of the foot during push-off.*

3.2 Methods

3.2.1 Estimation of Foot Position and Orientation

An accelerometer measures the sum of sensor acceleration $\boldsymbol{a}^s$ and gravitational acceleration $\boldsymbol{g}^s$:

$$\boldsymbol{s}^s = \boldsymbol{a}^s - \boldsymbol{g}^s. \tag{3.1}$$

Position is estimated by integration of sensor acceleration, which means the gravitational acceleration needs to be removed. This requires the sensor orientation to be estimated, which is obtained by integration of the angular velocity measured by gyroscopes using the following differential equation [59]:

$$\dot{\boldsymbol{R}}_s^g = \boldsymbol{R}_s^g \tilde{\boldsymbol{\omega}}_s^{s,g}, \tag{3.2}$$

where $\boldsymbol{R}_s^g$ denotes the 3D rotation matrix representing the change of coordinates between sensor frame Ψ_s and global frame Ψ_g, $\dot{\boldsymbol{R}}_s^g$ its time derivative and $\tilde{\boldsymbol{\omega}}_s^{s,g}$ the skew-symmetric matrix consisting of the components of the angular velocity vector of frame Ψ_s with respect to Ψ_g, expressed in Ψ_s:

$$\tilde{\boldsymbol{\omega}}_s^{s,g} = \begin{pmatrix} 0 & -\omega_z & \omega_y \\ \omega_z & 0 & -\omega_x \\ -\omega_y & \omega_x & 0 \end{pmatrix}. \tag{3.3}$$

Applying the above equations yields the position in global coordinates $\boldsymbol{x}^g(t)$:

$$\begin{aligned} \boldsymbol{a}^g(t) &= \boldsymbol{R}_s^g(t)\boldsymbol{s}^s(t) + \boldsymbol{g}^g \\ \boldsymbol{v}^g(t) &= \boldsymbol{v}_0 + \int_{t_0}^{t} \boldsymbol{a}^g(\tau)d\tau \\ \boldsymbol{x}^g(t) &= \boldsymbol{x}_0 + \int_{t_0}^{t} \boldsymbol{v}^g(\tau)d\tau, \end{aligned} \tag{3.4}$$

where $\boldsymbol{v}^g(t)$ denotes the velocity in global coordinates, $\boldsymbol{v}_0$ the initial velocity, and $\boldsymbol{x}_0$ the initial position.

Integration of angular velocity to orientation and double integration of acceleration to position is prone to drift due to sensor noise and a fluctuating offset. However, since walking is a cyclical movement, several initial and final conditions can be applied to reduce this drift [70]. For the integration of angular velocity, the inclination can be assumed equal at every stride during the time interval when the foot is flat on the floor. In addition, it is assumed that the velocity is zero, and that the vertical position is constant during these intervals. Moreover, to minimize integration time, position estimation for each stride is divided in two phases. During the stance phase, position estimation is based on the orientation and knowledge about the geometry of the shoe. During the swing phase, position estimation is obtained by integrating the acceleration twice (3.4). To obtain the position of the foot for several strides, the estimated position changes for the individual strides are added.

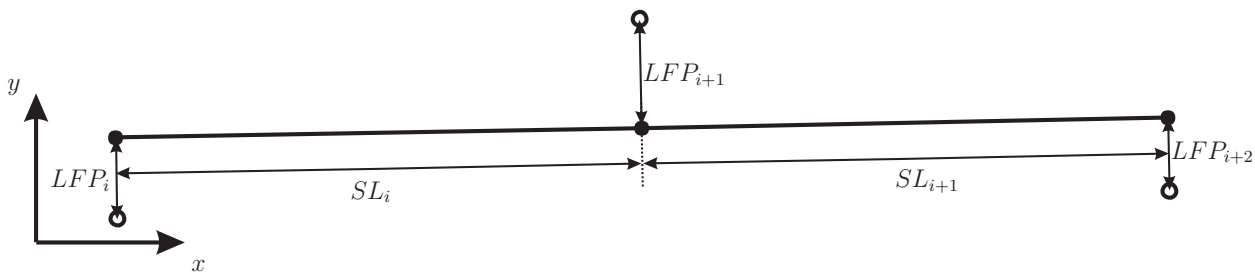

Figure 3.2: *Schematic view of three consecutive heel positions of the same foot (circles), and the orthogonal projections of these positions on the average walking path (dots). Stride Length (SL) and Lateral Foot Placement (LFP) are defined with respect to this average walking path.*

3.2.2 Foot Placement Parameters

In order to evaluate the accuracy of the ambulatory measurement system for the analysis of foot placement, two parameters were chosen for evaluation: Lateral Foot Placement (LFP) and Stride Length (SL). Each stride, the time instance of Heel Down (HD) was defined using the force transducers beneath the instrumented shoe. The evaluated parameters, LFP and SL, were estimated for each foot separately, because the inertial sensors do not provide information about the relative positions of both feet. To do so, an average walking path was calculated by a first order least squares fit to a predefined number of consecutive HD positions of the same foot. For each stride, the HD position was defined in the middle of the mounting plate beneath the heel (Figure 3.1). An example of the average path for three consecutive strides is shown in Figure 3.2. The parameters were defined as follows:

Stride Length (SL) was defined as the distance between heel positions of the same foot in a direction parallel to the average walking path (Figure 3.2) at two consecutive HD instances.

Lateral Foot Placement (LFP) was defined as the distance between the heel position and the orthogonal projection of this heel position of the same foot on the average walking path (Figure 3.2).

Since the position and orientation were estimated by integration which is prone to integration drift (Section 3.2.1), the predefined number of strides used to determine the average walking path was varied to analyze its influence on the accuracy and to determine the optimal number of strides. It should be noted that the method proposed, which fits an average path using a moving window, implies that multiple LFPs and SLs will be estimated for the same stride.

3.2.3 Experimental Methods

To determine the foot placement parameters, experiments were performed in a gait laboratory using a 3D optoelectronic reference registration system (Optotrak), consisting of five arrays of three cameras. Ten subjects participated in this study (7 male, 3 female, age 27.5 ± 4.9 years (mean $\pm$ standard deviation), length 1.76 ± 0.07 m, and body mass 72.0 ± 8.4 kg). Two subjects were excluded for data analysis, because most trials of these subjects showed large peaks in the acceleration ($> 10\ g$) estimated by double integration of Optotrak position data. These acceleration peaks occurred during the transition of measurement volumes of individual cameras and yielded position errors up to 10 cm. All subjects were healthy and exhibited no clinical abnormalities. Informed consent was obtained from each subject prior to the experiment. The subjects, wearing instrumented shoes, were asked to walk through the laboratory (10 m walkway) under two different conditions (eyes open (EO) and eyes closed (EC)). Foot movement was estimated using instrumented shoes (Figure 3.1) consisting of orthopaedic sandals with two 6D force/moment sensors (ATI-Mini45-SI-580-20, supplier: Schunk GmbH & Co. KG) beneath the heel and forefoot. Moreover, an inertial sensor (Xsens Technologies B.V.) and an Optotrak marker were rigidly attached to each force/moment sensor.

The analogue data from the force transducers and inertial sensor data were acquired at 50 Hz. Data from the reference system were acquired at 100 Hz, but resampled to 50 Hz. All data were low-pass filtered by applying a recursive second order Butterworth filter at 15 Hz. A pulse, generated by the Optotrak system, was recorded by an additional channel of the inertial sensor system. This pulse was used to synchronize Optotrak, force/moment and inertial data.

3.2.4 Statistical Analysis

A statistical analysis was carried out to determine whether the ambulatory system is able to distinguish between the EO and EC condition like the reference system. All statistical tests were done using a repeated measures general linear model analysis with post-hoc comparison ($p < 0.05$) in SPSS.

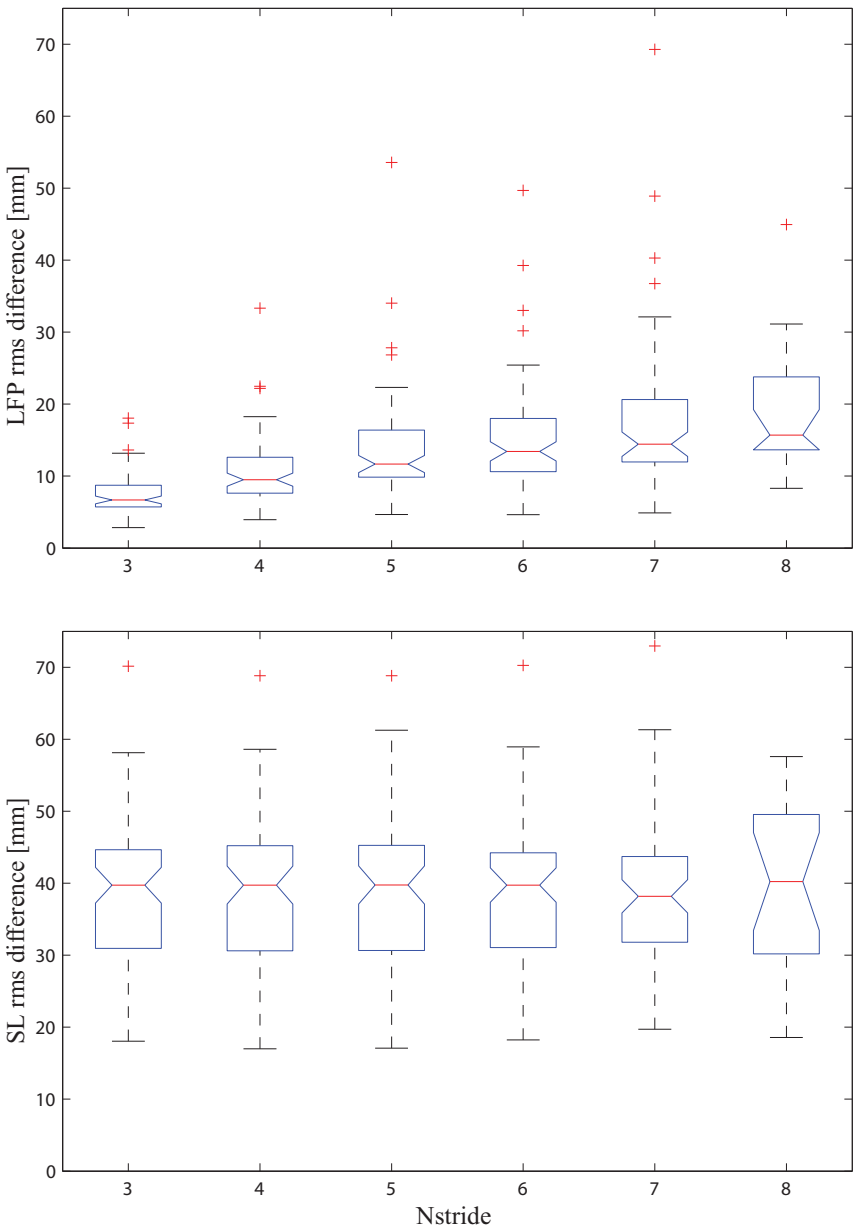

Figure 3.3: *Box and whisker plot of rms differences for LFP (top) and SL (bottom) estimated with ambulatory and reference systems for a varying number of strides used to calculate the average walking path. The rms differences were calculated for all trials of the EO condition. The box has lines at the lower quartile, median, and upper quartile values. The whiskers are the lines showing the extent of the rest of the data. Outliers are indicated by plus signs.*

3.3 Results

3.3.1 Accuracy of LFP and SL Estimation

The number of trials that have been analyzed were 75 for the EO condition, and 38 for the EC condition resulting in a total number of 113 trials. In order to determine the number of strides used to construct the average walking path, root mean square (rms) differences between the ambulatory and the reference systems were calculated. It should be noted that this was done for

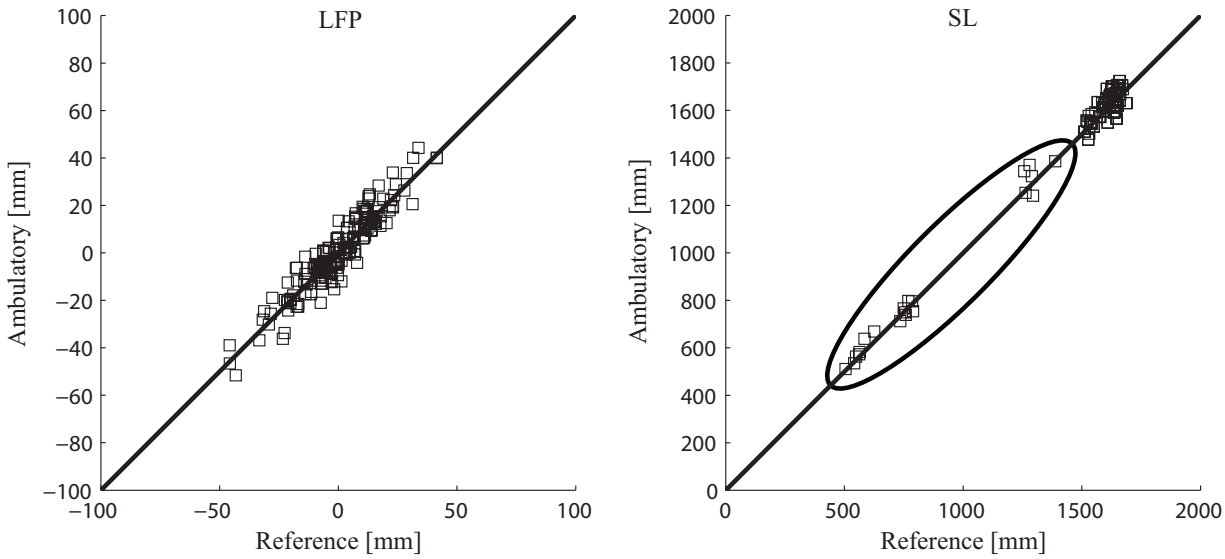

Figure 3.4: *LFP and SL estimated by the reference and ambulatory measurement systems of a representative subject for the EO condition. The encircled SL strides are caused by initiation and termination of walking.*

the EO condition only. Figure 3.3 shows the results, which indicate that the SL rms difference is hardly influenced by the number of strides, whereas the LFP rms difference increases as the number of strides increases. Since the smallest LFP rms difference can be clearly seen at three consecutive strides, it is chosen to use three consecutive strides for analysis in the remainder of this study.

3.3.2 Similarity of LFP and SL Estimation

The LFP and SL of a representative subject for the EO condition are shown in Figure 3.4. Ideally, if there was no difference between both measurement systems, all estimations would be on the diagonal line. The encircled SL strides indicate initiation and termination of walking, which are considered as disturbances inherent to human walking. To determine the similarity between both measurement systems, correlation coefficients were calculated for each subject. Subsequently, the correlation coefficients were averaged over all subjects. For continuous walking with EO, excluding the first and last stride of each trial, the correlation coefficients were 0.77 ± 0.10 (mean $\pm$ standard deviation) for LFP, and 0.82 ± 0.08 for SL. For initiation and termination of walking with EO, the correlation coefficients were 0.84 ± 0.09 for LFP, and 0.995 ± 0.001 for SL.

3.3.3 Stride to Stride Variability

To analyze the ability of the proposed system for the analysis of stride to stride variability, standard deviations were calculated for the EO condition of LFP and SL for each subject. The accuracy is represented by the percentage difference obtained by dividing the difference of the variability for LFP and SL of each subject calculated with both measurement systems by the variability calculated with the reference system. The results, averaged over all subjects, were 7.8 ± 2.6 % for LFP, and 0.67 ± 0.49 % for SL.

Table 3.1: *Significance levels for the influence of walking condition (EO-EC), measurement system (ambulatory-reference), and their interaction for LFP and SL. A significant difference is indicated by an asterisk (*).*

Parameter	Condition	System	System x Condition
LFP	0.021*	0.001*	0.823
SL	0.007*	0.063	0.453

3.3.4 Sensitivity for Manipulation

The results of the statistical analysis for the different walking conditions are shown in Table 3.1. As expected, the influence of walking condition is significant for LFP and SL. The influence of walking condition is also graphically shown in Figure 3.5 by an increase of LFP and a decrease of SL. Although the influence of measurement system is significant for the LFP comparison as indicated by the fourth column of Table 3.1, it is important to note that the last column of Table 3.1 indicates that there is no significant interaction effect. The statistical analysis implies that both measurement systems register similar changes caused by different walking conditions, and are able to discriminate between the EO and EC condition.

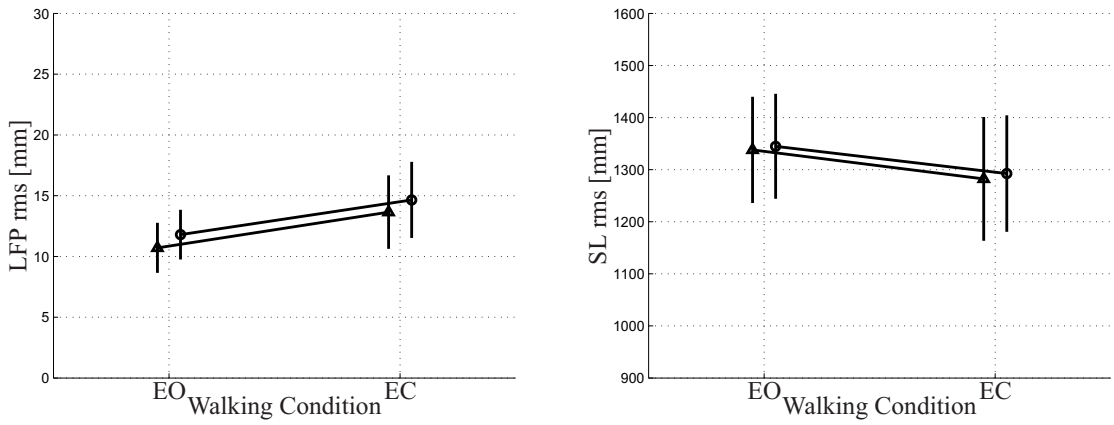

Figure 3.5: *Effect of measurement system and walking condition on LFP (left) and SL (right) with an average walking path determined using three consecutive strides. LFP or SL is shown on the vertical axis and walking condition on the horizontal axis. The circles and triangles indicate the mean values of the ambulatory and reference system, respectively. The vertical lines indicate the standard deviations.*

3.4 Discussion

This study proposes a method to assess two spatial parameters, Lateral Foot Placement (LFP) and Stride Length (SL), during walking using an ambulatory measurement system. The measurement system consisted of a pair of instrumented shoes that were introduced in Chapter 2. The results revealed in different ways that the ambulatory system can well be used in the

assessment of LFP and SL. First, the ambulatory system is able to discriminate between different walking conditions, like the reference system. Second, both measurement systems show good correspondence for the stride to stride variability, as indicated by the percentage difference between both measurement systems for the standard deviation of LFP and SL. Third, the high correlation coefficients indicated a large similarity between both measurement systems. For initiation and termination of walking with EO, the correlation coefficients were higher compared to continuous walking with EO. This is caused by a lower stride to stride variation for continuous walking, which emphasizes the relative importance of the measurement error in both measurement systems. It should be noted that the correlation for initiation and termination of walking gives a better indication of the accuracy of the ambulatory measurement system for a larger range of walking speeds.

The ambulatory measurement system was compared to a widely used 'golden standard', an optical position measurement system. Besides the drawbacks already mentioned in the introduction associated with optical position measurement systems, the relatively large measurement volume as used in the present study introduces another drawback. As stated in Section 3.2.3, the transition between the measurement volumes of individual cameras yielded position errors up to 10 cm, which caused two subjects to be excluded from the analysis. A solution would be to increase the number of cameras used, but this also increases the complexity of the measurement system as well as the financial costs.

The proposed method was used to estimate LFP and SL for a limited number of consecutive strides for each foot separately. If it is desired to estimate the relative positions of both feet with respect to each other, additional information needs to be included since the position is obtained by integration which means that only the change of position of the same foot can be estimated. A possible option to obtain the additional information is to apply Newton's second law for rotational motion. Using the ground reaction force as measured by the instrumented shoe and the assumption that the product of angular acceleration and moment of inertia will be small during walking allows the lateral distance between both feet to be estimated [72]. If it is desired to relate more strides to each other or if the absolute positions in space of the feet are required, the system can be fused with another aiding system such as GPS [29] or magnetic tracking systems [73, 35]. However, these aiding systems will have their drawbacks as well and increase the complexity of the measurement system. Moreover, for balance assessment, most information is obtained by relating the current stride to one or a few consecutive strides.

It should be noted that the estimation of LFP and SL in an ambulatory environment does not necessarily require an instrumented shoe to be worn. In principle, an inertial sensor mounted on the foot or the shoe will suffice. However, besides the ability to estimate spatial parameters, the instrumented shoe allows more gait variables to be estimated. For balance assessment for example, it is crucial to monitor center of mass trajectories, center of pressure trajectories and the relation between these variables which is described in Chapter 4. Chapter 2 showed the feasibility of the instrumented shoe to estimate ankle and foot dynamics accurately in an ambulatory environment. The method proposed in the current study enhances the potential of the instrumented shoe as an ambulatory measurement system allowing several spatial gait variables to be estimated in an ambulatory environment. Additionally, the instrumented shoe can be used to assess temporal parameters like stride time, (double) stance time and stride frequency. Compared to traditional methods, based on optical position measurement systems that can require rather complex signal conditioning algorithms, this system allows temporal parameters to be assessed accurately using a simple and straightforward method since the force transducers will only measure a force unequal to zero during ground contact.

Although the shoe (Figure 3.1) introduces extra height and weight compared to normal shoes, the influence of the shoe on the gait pattern appeared to be small [61]. It should be emphasized that the purpose of this study was to evaluate the accuracy of the estimation of foot placement, not to analyze undisturbed gait. An optimization with respect to the design of the shoe, e.g. miniaturization of the sensors and components, will reduce the influence on gait without affecting the functionality.

The estimation of foot placement has a significant contribution to understanding human motor control. During human walking, foot placement is used to balance the body. It would be interesting to use the proposed measurement method to characterize foot placement in more challenging environments such as circular walking [74] or walking on uneven terrain. In principle, the methods proposed in this study are appropriate for such applications.

4

Ambulatory Estimation of Center of Mass Displacement During Walking

H.M. Schepers, E.H.F. van Asseldonk, J.H. Buurke, and P.H. Veltink
IEEE Transactions on Biomedical Engineering, 56(4):1189-1195, 2009

Abstract

The Center of Mass (CoM) and the Center of Pressure (CoP) are two variables that are crucial in assessing energy expenditure and stability of human walking. The purpose of this study is to estimate the CoM displacement continuously, using an ambulatory measurement system. The measurement system consists of instrumented shoes with 6D force/moment sensors beneath the heels and the forefeet. Moreover, two inertial sensors are rigidly attached to the force/moment sensors for the estimation of position and orientation. The estimation of CoM displacement is achieved by fusing low-pass filtered CoP data with high-pass filtered double integrated CoM acceleration, both estimated using the instrumented shoes. Optimal cut-off frequencies for the low-pass and high-pass filter appeared to be 0.2 Hz for the horizontal direction and 0.5 Hz for the vertical direction. The CoM estimation using this ambulatory measurement system was compared to CoM estimation using an optical reference system, based on the segmental kinematics method. The root mean square (rms) difference of each component of the CoM displacement averaged over a hundred trials obtained from seven stroke patients was 0.020 ± 0.007 m (mean $\pm$ standard deviation) for the forward x direction, 0.013 ± 0.005 m for the lateral y direction, and 0.007 ± 0.001 m for the upward z direction. Based on the results presented in this study, it is concluded that the instrumented shoe concept allows accurate and continuous estimation of CoM displacement under ambulatory conditions.

4.1 Introduction

Biomechanical analysis of human movement is used by many different disciplines to understand the mechanisms underlying human movement, to quantify performance, or to guide rehabilitation interventions. A significant contribution is provided by means of gait analysis. The easiest and most common model used to describe human walking is the inverted pendulum model [62, 75]. In this model, human walking is characterized by two variables: the Center of Mass (CoM) and the Center of Pressure (CoP). The CoM is an imaginary point at which the total body mass can be assumed to be concentrated. The CoP is the application point of the Ground Reaction Force (GRF), the point on the contact surface between body and ground where the moments about the horizontal axes are zero. In the inverted pendulum model, the CoM is balancing on a rod with the origin at the CoP. The double support phase is viewed as a transition from one inverted pendulum to the next.

Several methods exist for the estimation of CoM movement which differ in the underlying assumptions. The segmental kinematics method [44, 76, 77] is based on the definition of the CoM and models the body as a kinematic chain of rigid segments. By measuring the position and orientation of each segment and by approximating the mass fractions as well as the locations of the CoM of each segment, an estimation of the overall CoM movement is obtained. Another method is the double integration of GRF method based on Newton's second law [78, 79], which states that the net external force acting upon a body is equal to its mass multiplied by its acceleration. Since the external force and body mass can be measured accurately by a force plate, an estimation of the acceleration of the CoM is obtained. The displacement of the CoM can be calculated through double integration of acceleration after subtracting gravitational acceleration, with proper consideration of initial constants of integration, i.e. initial velocity and position [80, 81]. A third method, the CoP low-pass filter method, uses the knowledge that CoP motion has higher frequency content than CoM motion [82, 83]. Moreover, the relative magnitude of the CoM movement with respect to the CoP movement can be described by a mathematical relation in the frequency domain [84], assuming that the movement is periodic and that the body can be modeled as an oscillating inverted pendulum. A fourth method is to assume that CoM movement can be approximated by movement of the pelvis [85]. This simple method assumes that the CoM is stationary within the pelvis, which may be a reasonable assumption in normal gait, but becomes inaccurate when relative movement of body segments increases, since the location of the CoM is affected by movement of individual segments. These methods have been extensively compared by many researchers [86, 87, 88, 89, 90, 91, 92]. Summarizing, it can be concluded that in general the performance of the segmental kinematics method is similar to that of the double integration of GRF method, and superior to the CoP low-pass filter method and pelvic movement method.

Although widely accepted, the above mentioned methods have their limitations as well. The performance of the segmental kinematics method depends heavily on the accuracy of the approximated segmental mass fractions and segment CoM locations. Moreover, it requires precise marker or sensor placement for accurate position and orientation determination. The performance of the double integration of GRF method is limited by the accuracy of the determined initial constants of integration. A joint drawback of all described methods is the restriction to a laboratory environment and the accompanying inability for continuous measurement of the CoM trajectory. The segmental kinematics method and pelvic movement method are limited by the measurement volume of the optical measurement system, whereas the double integration of GRF method and CoP low-pass filter method are limited by the number of

Figure 4.1: *Picture of the instrumented shoe with force/moment sensors beneath the heel and forefoot and inertial sensors rigidly attached to the force/moment sensors.*

force plates and the occurrence of a correct hit.

It is desirable to estimate the CoM trajectory continuously during walking, since it contains important information about dynamic balance control and, especially for pathological gait, the CoM movement can vary from stride to stride. Moreover, the measurement of the CoM should not be restricted to a laboratory environment, but should be possible during everyday life as well. The objective of this study is to determine the CoM trajectory continuously during walking, based on a combination of methods described above, using an ambulatory measurement system. The proposed method fuses CoP trajectory with double integrated CoM acceleration, such that the best characteristics of each constituent are used. For validation, data from seven stroke patients were acquired and the estimated CoM trajectories were compared to the trajectories obtained by the segmental kinematics method using an optical position measurement system as a reference.

4.2 Methods

This study proposes a method to estimate the CoM trajectory continuously during walking using an ambulatory measurement system. This section first describes the methods used to obtain an estimation of the CoM displacement, followed by a description of the experimental methods.

4.2.1 Estimation of Center of Mass Displacement

The trajectory of the CoM is estimated by fusing CoP with double integrated CoM acceleration, derived from the GRF measured by the instrumented shoes. The instrumented shoe was introduced in Chapter 2, and is shown in Figure 4.1. A schematic drawing of a subject during walking with the most important variables is depicted in Figure 4.2. This section first describes the derivation of the CoP position of a single stride from signals measured by the force/moment sensors. Subsequently, the estimation of foot position and orientation is described, which are required to obtain the CoP trajectory during several strides. Finally, the fusion of CoP trajectory with double integrated CoM acceleration, based on a frequency domain method, is described.

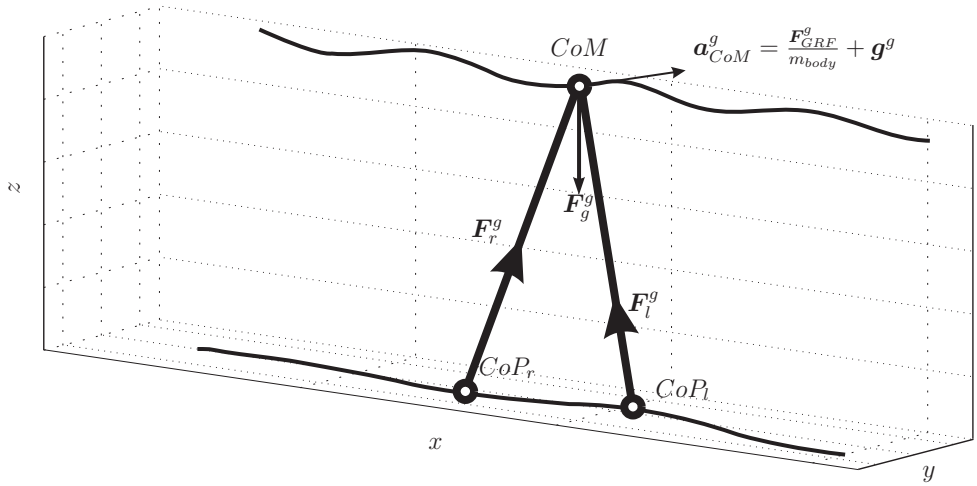

Figure 4.2: *Schematic drawing of a subject during walking, where the trajectories of the CoP and CoM are indicated by the solid lines. The small circles denote the current position of the CoM and the CoP of the left foot (CoP_l) and right foot (CoP_r). The GRFs of the left and right foot are denoted by $\boldsymbol{F}^g_l$ and $\boldsymbol{F}^g_r$, respectively, and the gravitational force by $\boldsymbol{F}^g_g = -m_{body} \cdot \boldsymbol{g}^g$, where m_{body} denotes the body mass and $\boldsymbol{g}^g$ the gravitational acceleration. Newton's second law relates the sum of GRFs of the left and right foot $\boldsymbol{F}^g_{GRF}$ to the acceleration of the CoM $\boldsymbol{a}^g_{CoM}$ as stated in (4.5).*

Estimation of Foot Position and Orientation

An estimation of foot position and orientation is obtained by combining the signals of an inertial sensor consisting of three accelerometers, and three gyroscopes. The accelerometers measure the sum of sensor acceleration $\boldsymbol{a}^s$ and gravitational acceleration $\boldsymbol{g}^s$ expressed in the sensor frame Ψ_s: $\boldsymbol{s}^s = \boldsymbol{a}^s - \boldsymbol{g}^s$. The gyroscopes measure the angular velocity $\boldsymbol{\omega}^{s,g}_s$ of the sensor frame Ψ_s with respect to the global frame Ψ_g, expressed in the sensor frame Ψ_s. The coordinate axes of the global frame are defined by positive x in the direction of gait; positive z directed upward; and positive y perpendicular to the x and z directions such that the result is an orthogonal right-handed coordinate system. It is desired to express all signals in the global coordinate frame Ψ_g, which means the rotation matrix $\boldsymbol{R}^g_s$ needs to be known. This matrix is obtained by solving the differential equation [59]:

$$\dot{\boldsymbol{R}}^g_s = \boldsymbol{R}^g_s \tilde{\boldsymbol{\omega}}^{s,g}_s, \tag{4.1}$$

where $\tilde{\boldsymbol{\omega}}^{s,g}_s$ is the skew-symmetric matrix of the angular velocity measured by the gyroscopes $\boldsymbol{\omega}^{s,g}_s$:

$$\tilde{\boldsymbol{\omega}}^{s,g}_s = \begin{pmatrix} 0 & -\omega_z & \omega_y \\ \omega_z & 0 & -\omega_x \\ -\omega_y & \omega_x & 0 \end{pmatrix}. \tag{4.2}$$

The estimation of position is dependent on the phase of the gait cycle and is restarted each stride, where the start and end of a stride are determined using the magnitude of the force measured by the force/moment sensors. During the stance phase, when the foot touches the ground, the position of the foot is fixed. During the swing phase, the position of the foot is estimated by double integration of the acceleration expressed in the global coordinate frame, after subtraction of the gravitational acceleration. The estimation of position and orientation by integration is prone to integration drift caused by noise and fluctuating offsets. This drift

is reduced by using zero velocity updates and the knowledge that the vertical position of the foot during midstance is equal at each stride [70]. To obtain the position and orientation during several strides, the estimated end position and orientation of the previous stride are used as an initial value for the current stride. To remove the error caused by an unknown initial orientation, it is assumed that both feet move in the same direction on average and that the distance between the feet is equal at the start and end of a measurement [93].

Estimation of Center of Pressure Trajectory

In Chapter 2, the CoP was estimated using instrumented shoes. The CoP $\boldsymbol{x}^g_{CoP,i}$ beneath each foot i was calculated by:

$$\boldsymbol{x}^g_{CoP,i} = \begin{pmatrix} -\frac{M^g_{y,i}}{F^g_{z,i}} \\ \frac{M^g_{x,i}}{F^g_{z,i}} \\ 0 \end{pmatrix}, \tag{4.3}$$

where $F^g_{z,i}$ denotes the vertical component of the GRF measured by force transducers under the shoe expressed in the global coordinate frame, and $M^g_{x,i}$ and $M^g_{y,i}$ the measured moments about the horizontal axes. To obtain the CoP of a foot for several strides, the estimated foot position is used. The contributions of both feet should be added to obtain the complete CoP trajectory. The addition is achieved by weighting the CoP trajectories of each foot by the relative magnitude of the GRF of that foot:

$$\boldsymbol{x}^g_{CoP} = \frac{\|\boldsymbol{F}^g_l\|}{\|\boldsymbol{F}^g_l + \boldsymbol{F}^g_r\|}\boldsymbol{x}^g_{CoP,l} + \frac{\|\boldsymbol{F}^g_r\|}{\|\boldsymbol{F}^g_l + \boldsymbol{F}^g_r\|}\boldsymbol{x}^g_{CoP,r}, \tag{4.4}$$

where $\boldsymbol{F}^g_l$ and $\boldsymbol{F}^g_r$ denote the measured GRF of the left and right foot, respectively.

Estimation of Double Integrated Center of Mass Acceleration

In order to estimate the CoM acceleration, Newton's second law was used, which states that the net external force acting upon a body is equal to its mass multiplied by its acceleration ($\boldsymbol{F} = m \cdot \boldsymbol{a}$). Since all body mass can be assumed to be lumped at the CoM and since the net external force is measured continuously by the instrumented shoes, an estimation of the acceleration expressed in the global coordinate frame is obtained. This acceleration vector consists of CoM acceleration $\boldsymbol{a}^g_{CoM}$ and gravitational acceleration $\boldsymbol{g}^g$, which means the gravitational acceleration needs to be removed (Figure 4.2):

$$\boldsymbol{a}^g_{CoM} = \frac{\boldsymbol{F}^g_{GRF}}{m_{body}} + \boldsymbol{g}^g, \tag{4.5}$$

where $\boldsymbol{F}^g_{GRF} = \boldsymbol{F}^g_l + \boldsymbol{F}^g_r$ denotes the total GRF measured by the instrumented shoes expressed in the global coordinate frame, and m_{body} the body mass of the subject. The estimated acceleration is double integrated to obtain the position $\boldsymbol{x}^g_{a_{CoM}}$:

$$\begin{aligned} \boldsymbol{v}^g_{a_{CoM}}(t) &= \boldsymbol{v}_0 + \int_{t_0}^{t} \boldsymbol{a}^g_{CoM}(\tau)d\tau \\ \boldsymbol{x}^g_{a_{CoM}}(t) &= \boldsymbol{x}_0 + \int_{t_0}^{t} \boldsymbol{v}^g_{a_{CoM}}(\tau)d\tau, \end{aligned} \tag{4.6}$$

where $\boldsymbol{v}_0$ and $\boldsymbol{x}_0$ denote the initial velocity and position, respectively.

Fusion

CoM displacement $\boldsymbol{x}^g_{CoM}$ is obtained by fusing CoP trajectory (4.3 and 4.4) with double integrated CoM acceleration (4.5 and 4.6). In essence, fusion is necessary since double integration of acceleration introduces drift, which is removed by a high-pass filter. This means, however, that the low frequency component of the CoM trajectory is removed as well. To reinclude this component, the knowledge that the CoP varies about the vertical projection of the CoM and coincides with this projection on average is used. Fusion consists of addition of the high-pass filtered, double integrated acceleration with the low-pass filtered CoP trajectory obtained from the instrumented shoes. To assure the result is indeed the CoM displacement, the order and cut-off frequency of the low-pass and high-pass filter were identical. It should be noted that the vertical component of the CoP is always zero, since the CoP is defined on the contact surface between body and ground. This means the low-pass filtered CoP trajectory is merely used to estimate the horizontal CoM displacement. Moreover, since the average height of the CoM is removed by the high-pass filter, the average height of the sacrum is added to the vertical component of the CoM displacement.

4.2.2 Experimental Methods

To compare the accuracy of the ambulatory measurement system with a conventional measurement system, experiments were performed in a gait laboratory, where an optical tracking system (Vicon, Oxford Metrics) was available. Seven stroke patients participated in this study. Their age was 58.3 ± 8.6 years (mean $\pm$ standard deviation), their length 1.80 ± 0.07 m, and their body mass 86.6 ± 12.2 kg. Informed consent was obtained from each subject prior to the experiment, and the study was approved by the local Ethical Committee. Subjects wearing instrumented shoes were instructed to walk repeatedly through the laboratory between predefined start and end points. To assure an equal distance between the feet at the beginning of each measurement, subjects were asked to position the feet against a mold attached to the floor between the feet before each walking trial. Body movement and GRF were measured by the instrumented shoes, while the optical tracking system was used as a reference. The instrumented shoes consisted of standard orthopaedic sandals equipped with two 6D force/moment sensors (ATI-Mini45-SI-580-20, supplier: Schunk GmbH & Co. KG) beneath the heel and forefoot, as shown in Figure 4.1. Each force sensor had a miniature inertial sensor (Xsens Technologies B.V.) rigidly attached to it, for the estimation of position and orientation. For the reference system, markers were placed on both legs (toe, heel, lateral malleolus, shank, knee, thigh), both arms (upper arm, elbow, head of ulna and styloid process of radius), left and right anterior superior iliac spine, left and right shoulder, and a 3 cluster marker on the sacrum.

Data from the inertial sensors, the analogue data from the force sensors beneath the shoe and the 3D marker data were sampled at 50Hz. All data were low-pass filtered by applying a second order recursive Butterworth filter, at a cut-off frequency of 15 Hz. The voltages from the force and moment sensors were converted to forces and moments by applying calibration matrices obtained from static calibration measurements. The synchronization between the inertial sensor system and Vicon was done by maximizing the correlation between pulses generated by a pulse generator that were sent to both measurement systems. Possible gaps in the Vicon data were spline-interpolated prior to filtering with a maximum gap-size of 15 samples.

Before fusing CoP trajectory and double integrated CoM acceleration, a low-pass filter was applied to the first and a high-pass filter to the second component. Both filters were first order recursive Butterworth filters.

The CoM displacement using the reference system was determined by the segmental kinematics method, based on the model of Koopman *et al.* [45]. Measured marker positions were used to determine body segmental mass fractions and segment CoM locations with the regression equations of Chandler *et al.* [94]. The total body CoM is calculated as the weighted sum of the CoM of every segment [77]:

$$\boldsymbol{x}_{CoM} = \frac{\sum_i m_i \cdot \boldsymbol{x}_{CoM,i}}{\sum_i m_i}, \tag{4.7}$$

where m_i is the mass of segment i, and $\boldsymbol{x}_{CoM,i}$ its CoM location.

4.3 Results

Data obtained from seven stroke patients were analyzed in this study, which resulted in a total number of 100 trials. To determine the optimal cut-off frequencies used to filter CoP and double integrated acceleration data, root mean square (rms) differences between the CoM estimates of the ambulatory and reference systems were calculated while varying the cut-off frequencies between 0.1 and 1 Hz. The cut-off frequency at the smallest rms difference was considered to be

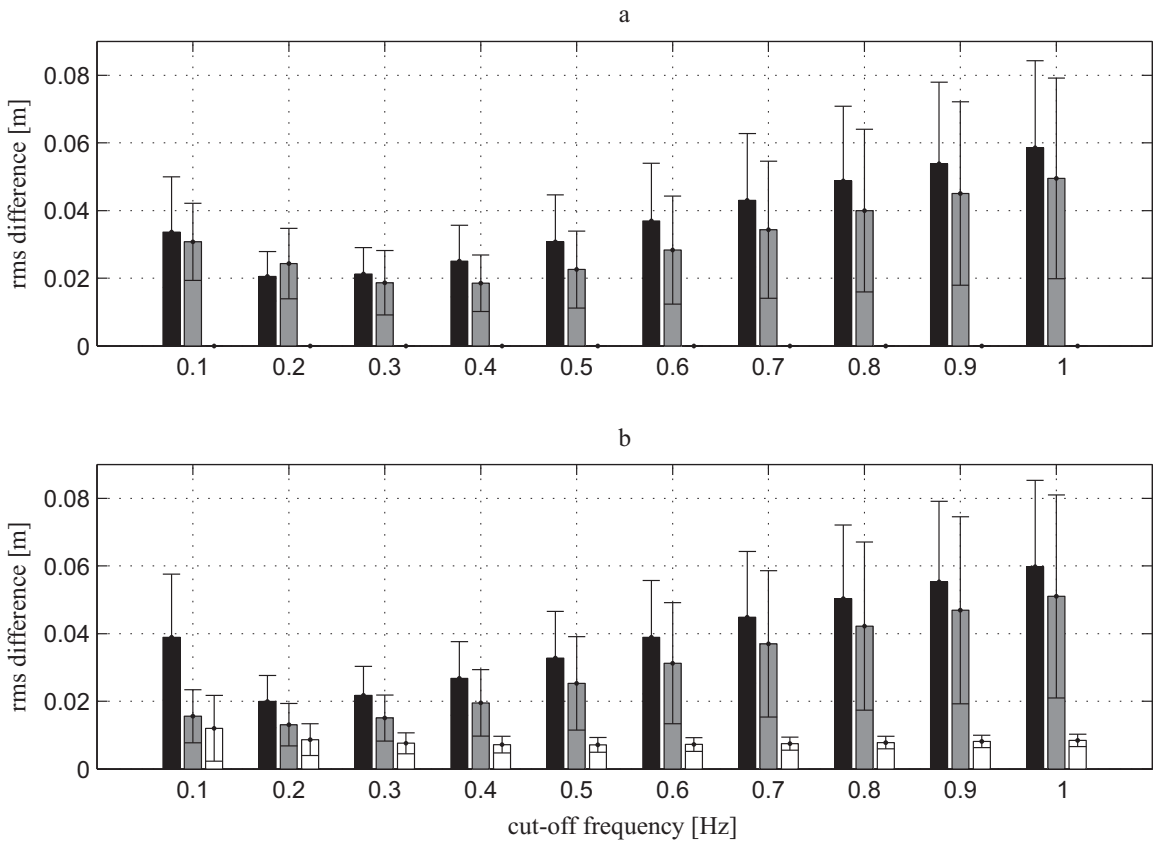

Figure 4.3: *RMS differences (mean and standard deviation averaged over all trials) of CoM estimates between ambulatory and reference systems with varying cut-off frequency (x: black; y: gray; z: white). (a) Only low-frequency CoP component (z direction not applicable). (b) After fusing low-frequency (CoP) and high-frequency (double integrated CoM acceleration) components.*

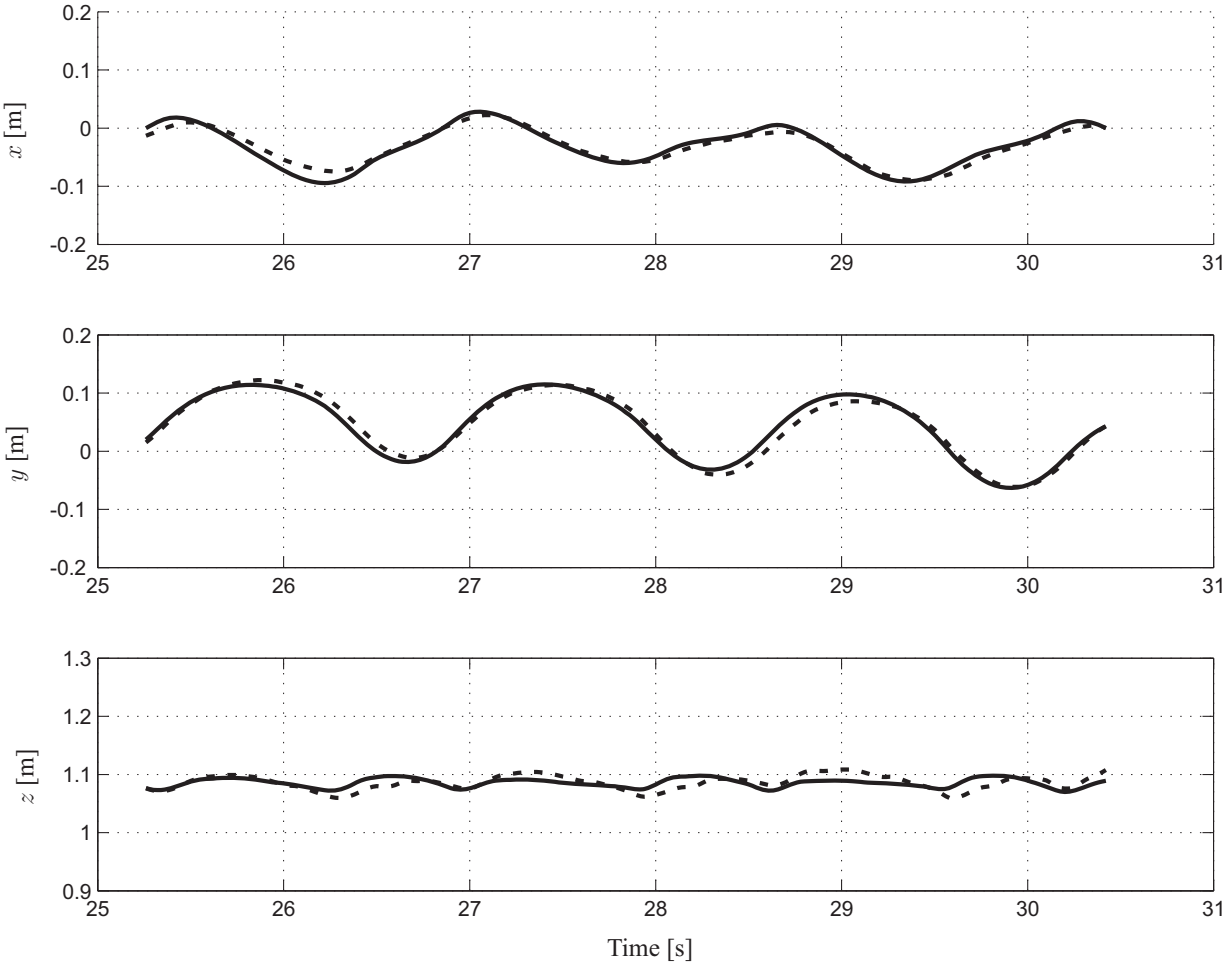

Figure 4.4: *CoM as a function of time for a representative trial estimated by ambulatory (solid) and reference (dashed) systems (x: upper; y: middle; z: lower). It should be noted that the integrated mean velocity has been subtracted from the x component.*

optimal. First, the low-pass filtered CoP trajectory was evaluated separately to compare against subsequent fusion with the double integrated CoM acceleration. The results for the x and y directions averaged over all analyzed trials, are shown in Figure 4.3(a). The optimal cut-off frequencies were determined to be 0.2 Hz for the x direction and 0.4 Hz for the y direction. It should be noted that the CoP trajectory does not provide information about the CoM movement in z direction. Second, the optimal cut-off frequencies for the x, y and z directions using the method combining CoP and double integrated CoM acceleration data were determined, and shown in Figure 4.3(b). The rms differences are smaller than in the case of CoP only, which demonstrates the need to include the high-frequency component for CoM displacement estimation. The results indicate that the optimal cut-off frequency is 0.2 Hz for the x and y directions and 0.5 Hz for the z direction.

The CoM displacement of a representative trial using the previously calculated cut-off frequencies is shown in Figure 4.4. For the x and y components, the mean value of the CoM displacement determined by each measurement system was subtracted to remove the static position error caused by a separate origin for both measurement systems. Moreover, the integrated mean velocity has been subtracted from the x component to visualize differences between both measurement systems in that direction.

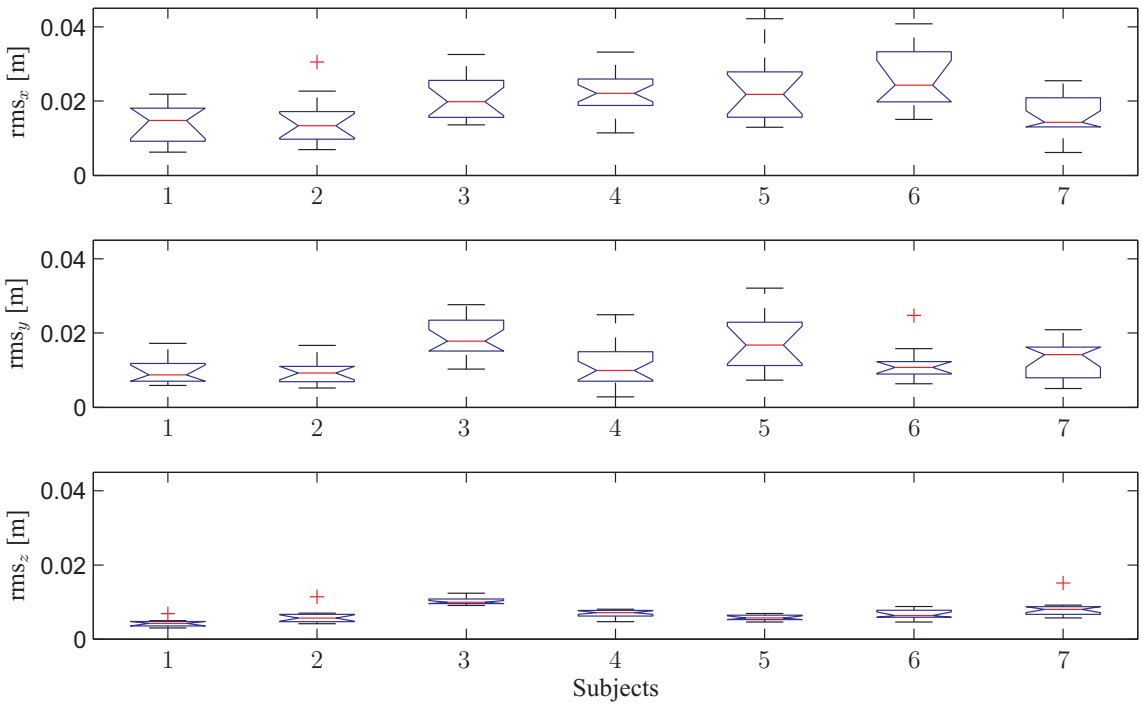

Figure 4.5: *Box and whisker plot of rms differences of CoM estimates using ambulatory and reference systems for each direction and all analyzed subjects (x: upper; y: middle; z: lower). The box has lines at the lower quartile, median, and upper quartile values. The whiskers are the lines showing the extent of the rest of the data. Outliers are indicated by crosses.*

An overview of the relative rms differences between the ambulatory and reference systems for the seven analyzed stroke patients is shown in Figure 4.5. The rms differences for each component of the CoM displacement averaged over all subjects were 0.020 ± 0.007 m (mean $\pm$ standard deviation) for the forward x direction, 0.013 ± 0.005 m for the lateral y direction, and 0.007 ± 0.001 m for the upward z direction. The rms distance between both CoM estimates was 0.025 ± 0.007 m. The rms differences as a percentage of the height of the subjects were 1.1 ± 0.4 % for the x direction, 0.7 ± 0.3 % for the y direction, and 0.4 ± 0.1 % for the z direction.

An indication of the potential of the ambulatory measurement system to quantify pathological gait disorders is shown in Figure 4.6. The asymmetric walking pattern of a stroke subject can be clearly seen in the figure. As illustrated, the foot of the paretic leg is rotated outward, and the position of the CoM is toward the non-paretic leg most of the time. Moreover, the figure clearly shows that the CoM displacement estimation by the reference system is limited to a few strides due to a restricted measurement volume, while the ambulatory system estimates the CoM displacement continuously.

4.4 Discussion

This study proposes a method to assess the CoM displacement continuously during walking using an ambulatory system. The method is based on a combination of the CoP low-pass filter method and the double integration of GRF method. The ambulatory system was compared to

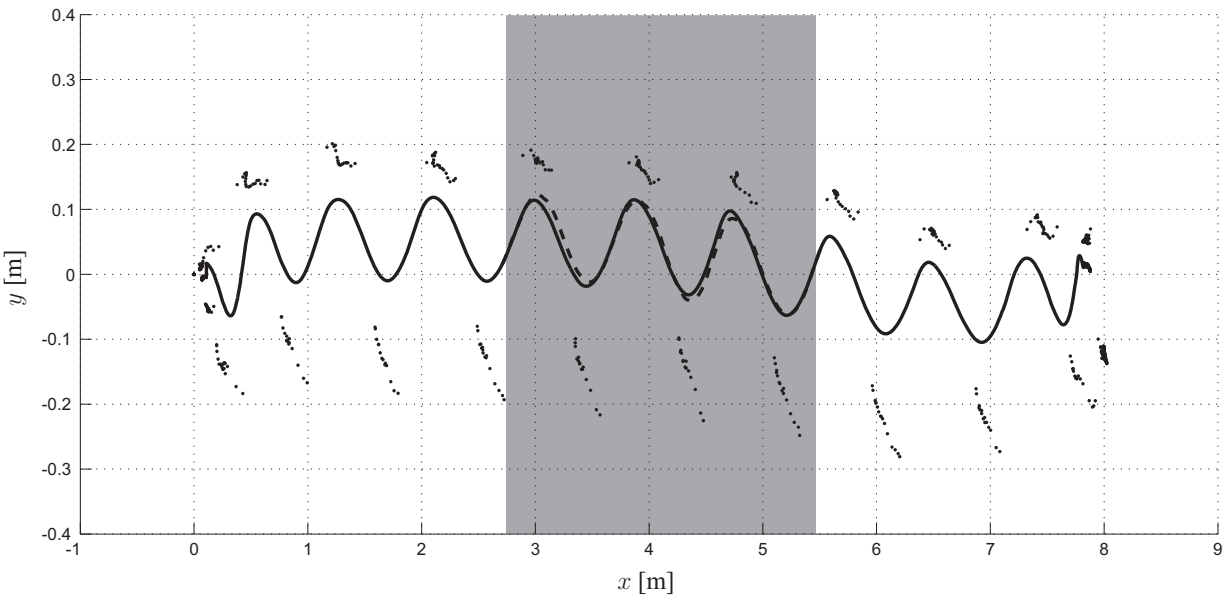

Figure 4.6: *Top view of the CoM of a walking stroke patient estimated by ambulatory (solid) and reference (dashed) systems. The data used to construct this figure is equal to the data used for Figure 4.4. On either side of the CoM, the CoP assessed from instrumented shoe data is indicated by the dotted lines, where each dot represents a time sample. The gray area indicates the Vicon measurement volume. For display purposes, the aspect ratio of the axes has not been equalized.*

a reference measurement system based on the segmental kinematics method. The results were promising and comparable to those described in literature [89]. In that study rms differences between CoM estimates as a percentage of the height of the subjects between the segmental kinematics method and the double integration of GRF method were 0.4 ± 0.3 % for the x direction, 0.4 ± 0.2 % for the y direction, and 0.9 ± 0.7 % for the z direction. Compared to the differences found in this study, their differences were smaller for the x direction, comparable for the y direction, and larger for the z direction.

Although the segmental kinematics method has been widely used and is considered to be the standard, its quality depends heavily on the accuracy of the approximated segmental mass fractions, segment lengths and CoM locations [92]. It is therefore questionable which of the two methods represents the true CoM displacement most accurately. Another option would have been to compare the ambulatory measurement system to the double integration of GRF method using force plates, which is widely used and accepted to be accurate as well. This is similar to a comparison of the GRF determined with both measurement systems which has been done in Chapter 2. The signals agreed well with a rms difference of 0.012 ± 0.001 N/N, being 1.1 ± 0.1 % of the maximal GRF magnitude. Every method will have its drawbacks and inaccuracies, since the CoM is an imaginary point at which the total body mass can be assumed to be concentrated and thus can not be measured exactly. Still, as discussed at the start of this section, the relative rms differences acquired in this study with respect to the amplitude of the CoM movement are comparable to those described in literature [89], while the described system allows measurements in an ambulatory environment.

Continuous estimation of CoM displacement, using the ambulatory system described in this study, has several advantages compared to existing measurement systems. Compared to the reference segmental kinematics method, which requires a full-body marker configuration,

the described measurement system allows estimation of CoM movement merely wearing the instrumented shoes (Figure 4.1). Moreover, the measurements are not restricted to a laboratory environment or a limited measurement volume. As indicated by Figure 4.6, pathological gait that can have a rather variable and asymmetrical walking pattern can still be estimated. Besides, the behavior at the start and end of a trial is incomparable to the behavior during the remainder of a trial, but as interesting for evaluating motor control. Especially for pathological gait, continuous estimation of CoM displacement is important as it can be used to monitor improvement, efficiency of walking, and balance control.

Although the results presented in this study are promising, there is still room for improvements. First, estimation of position and orientation by integration introduces drift, which will increase for longer time durations. However, walking is a cyclical movement, which means initial and final conditions can be applied every stride, i.e. zero velocity when the foot is flat on the floor, constant vertical position of the foot at midstance during level walking. Moreover, for the determination of gait parameters and biomechanical analysis, relative positions instead of absolute positions in space are important. The integration drift in these relative positions can be limited by the use of human body constraints. Also, to limit the integration drift in the estimation of the lateral distance between the feet and as an alternative for the mold between the feet used to estimate this distance initially, Newton's second law for rotational motion can be used. It states that the net external moment $\boldsymbol{M}$ acting upon a body is equal to its moment of inertia $\boldsymbol{I}$ times its angular acceleration $\boldsymbol{\alpha}$: ($\boldsymbol{M} = \boldsymbol{I} \cdot \boldsymbol{\alpha}$). The net external moment is calculated by the vector product of position and force ($\boldsymbol{M} = \boldsymbol{r} \times \boldsymbol{F}$). If the product of angular acceleration and moment of inertia is assumed to be small during walking, it follows that $\boldsymbol{r} \times \boldsymbol{F} = \boldsymbol{0}$. For the frontal plane this results in: $F_y \cdot z - F_z \cdot y = 0$. Since the forces F_y and F_z are measured by the force/moment sensors and the vertical position z can be estimated using the methods proposed in this study, an estimation of the lateral distance y between the feet and the projection of the CoM on the ground is obtained.

Second, the design of the instrumented shoe (Figure 4.1) can be improved. The current design could raise questions about its influence on the gait pattern and the clinical applicability as it seems rather heavy and bulky. Nevertheless, the influence of the shoe on the gait pattern appeared to be small as reported by Liedtke *et al.* [61]. In that study, an evaluation of several gait parameters was performed with healthy subjects wearing the instrumented shoes, light, normal and heavy weight shoes. Significant differences between the shoe types were found in maximum GRF only, but these differences could not be attributed to individual shoe types. Moreover, the differences were small compared to the body weight of the subjects and were therefore not considered relevant. The small influence on gait was confirmed by the experience of patients, who were able to walk comfortably with the instrumented shoes. Irrespective of the possible gait adaptation caused by the modified shoes, the resulting gait was registered by both the ambulatory and the reference system. The purpose of this study was to introduce the measurement method, not to optimize the design of the instrumented shoe. In principle, such an optimization will further reduce the influence on gait without affecting the accuracy of the measurement system.

The accuracy of the CoM displacement estimated by the ambulatory measurement system is dependent on the choice for the cut-off frequencies of the filters used to fuse the low-frequency and high-frequency component, as indicated by Figure 4.3. Optimal values for the cut-off frequencies appeared to be 0.2 Hz for the horizontal direction and 0.5 Hz for the vertical direction. These values are, among other things, related to gait velocity and should be changed accordingly when for example the CoM displacement during running would be analyzed. The

dependencies of the cut-off frequencies with respect to these variables needs to be investigated thoroughly.

Although the rms difference between the CoM movement in vertical z direction estimated by both measurement systems was small compared to the horizontal x and y directions and small compared to literature [89], the relative difference of the z direction with respect to the CoM excursion in that direction was larger, as shown at the bottom of Figure 4.4. Since the CoM movement in z direction is estimated by high-pass filtering the double integrated CoM acceleration only, it does not contain low-frequent information. It should be noted that the horizontal and not the vertical position of the CoM with respect to the CoP is of primary interest in balance assessment [62, 95].

None of the above current drawbacks and remarks, however, jeopardize the potential value of the presented concept of continuous ambulatory CoM tracking in biomechanical analysis.

5

Stochastic Magnetic Measurement Model for Relative Position and Orientation Estimation

H.M. Schepers, and P.H. Veltink

Submitted

Abstract

This study presents a stochastic magnetic measurement model that can be used to estimate relative position and orientation. The model predicts the magnetic field generated by a source coil at the location of the sensor. The model will be used in a fusion filter that predicts the change of position and orientation by integration of acceleration and angular velocity measured by inertial sensors. The difference between the actual magnetic measurement and the prediction of the measurement are used to reduce the drift caused by integration of acceleration and angular velocity. The model is accurate as confirmed by the small rms differences between validation measurements and predictions of the magnetic field using the model. The use of a linearized version of the measurement model for the fusion filter, and the appearance of a ferromagnetic object in the vicinity of the source or sensor were defined as two sources of error that may lead to divergence of the fusion filter. Both sources of error were analyzed and it appeared that the linearized model introduces errors which generally increase for sensor locations near the source. Moreover, it appeared that a ferromagnetic object influences the measurements only if it is located near or between the source and sensor.

5.1 Introduction

Human motion tracking comprises the reconstruction of position and orientation of body segments. Several methods exist for the estimation of position and orientation based on different sensing technologies, for example optical, magnetic, or acoustic. A common drawback of the existing measurement systems is their restriction to a laboratory environment. A solution to overcome this common drawback is the use of inertial sensors (accelerometers and gyroscopes). Change of position and orientation can be estimated by integration of acceleration and angular velocity, respectively. However, since the sensor signals are rather noisy and can have a fluctuating offset, integration of these signals involved in estimation of orientation and position change introduces integration drift. This drift can be limited by using suitable estimation algorithms [28, 51, 96, 16], initial and final conditions and limiting the integration time [70, 56]. Still, a stable, robust and ambulatory solution is desired, especially for the estimation of relative position of body segments since the starting position is unknown.

A commonly used solution is to fuse inertial measurements with an aiding system. An example is the use of GPS measurements [29, 97], but the accuracy is limited partly due to possible loss or degradation of the GPS signal, especially for relative positions between body segments. Other examples are the use of an acoustic time of flight measurement system [31], or an optical [30], or a magnetic position and orientation tracking system [33]. However, these systems are commonly fixed to a laboratory environment. Recently, it was proposed to fuse inertial sensing with Ultra-Wide Band (UWB) positioning [32]. An advantage of magnetic tracking compared to UWB or acoustic tracking is that the human body is transparent for the field applied. Compared to GPS tracking, magnetic tracking does not suffer from the mentioned loss or degradation of the signal, although it is sensitive to disturbances caused by for example ferromagnetic material. Summarizing, it can be concluded that the combination of an inertial measurement system and an ambulatory magnetic tracking system that can minimize errors due to magnetic disturbances may be a good choice to estimate relative positions and orientations of body segments.

An ambulatory magnetic position and orientation measurement system was previously proposed by Roetenberg *et al.* [34]. A major advantage over commercially available systems, like Fastrak (Polhemus) and Flock of Birds (Ascension Technology) as used by Emura and Tachi [33], is that the magnetic source is worn on the body which means measurements can be performed during everyday life. Moreover, since the ranges to be covered are generally smaller compared to available systems, the coil dimensions can be reduced. A drawback is that, besides the movement of the sensor, the movement of the source needs to be estimated. In another study [35], the measurement system was fused with an inertial sensor system using a complementary Kalman filter structure to correct for the integration drift, and to reduce errors related to magnetic disturbances. Although the results were promising, the method needs to be improved on several aspects. The estimation algorithm [98, 99], based on a magnetic dipole approximation of the source, requires all three source coils to be actuated every update, while the update rate is fixed and pre-assigned by the user. Moreover, the calculations did not involve a stochastic measurement model required for sensor fusion applying optimal estimation methods. Such a stochastic measurement model would also allow for an optimal choice of the actuation levels. Also, the source consisted of three coils which need to be mounted orthogonally and share the same origin. An algorithm using two source coils was proposed by Paperno *et al.* [100], but still the two coils needed to be mounted orthogonally and to share the same origin.

In order to apply the ambulatory magnetic position and orientation estimation system more

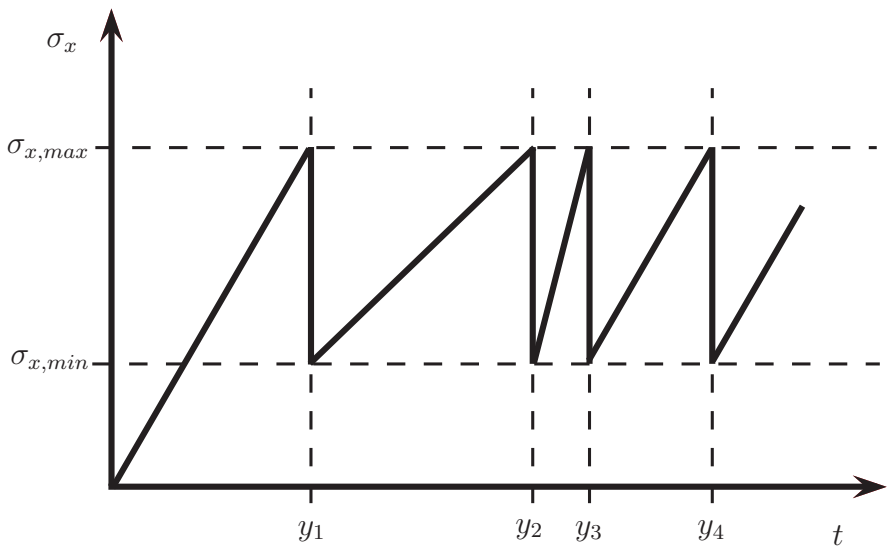

Figure 5.1: *Schematic overview of the reduction of the uncertainty associated with a state variable σ_x by fusion with measurements y. The time interval between updates is not fixed, since the filter updates only when the uncertainty exceeds a predefined threshold ($\sigma_{x,max}$).*

generally, an estimation method is needed which is not based on the dipole approximation and does not require the source coils to be mounted orthogonally or to share the same origin. It is therefore the objective of the current study to present a stochastic measurement model that predicts the magnetic measurement based on an estimation of position and orientation. The model is based on a single source coil and will be used in a fusion filter that combines inertial and magnetic sensing to estimate relative position and orientation of the sensor with respect to the source (Chapter 6). The accuracy of the measurement model is validated using a source coil and a remote sensor at known position and orientation. Moreover, the influence of a ferromagnetic object in the vicinity of the measurement system is analyzed.

5.2 Methods

5.2.1 Sensor Fusion

The measurement model proposed and evaluated in this paper will be used in a fusion filter to estimate relative positions and orientations of a remote sensor with respect to a source. The source exists of one or more coils mounted in a known configuration which can be actuated independently. The remote sensor consists of an inertial sensor (3D accelerometer and 3D gyroscope) and a 3D magnetometer. The inertial sensor is used to predict the change of position and orientation by integration of the sensor signals. Since integration of noisy signals introduces drift, magnetic updates are used to reduce the drift. The fusion filter compares the measurements to a prediction of the measurements using a stochastic magnetic measurement model and updates the estimates of position and orientation based on the difference between prediction and measurement. In general, a stochastic measurement model is described by:

$$\boldsymbol{y} = \boldsymbol{h}\left(\boldsymbol{x}\right) + \boldsymbol{v}, \tag{5.1}$$

where $\boldsymbol{h}\left(\boldsymbol{x}\right)$ denotes the nonlinear function which maps the state vector $\boldsymbol{x}$ to the measurement vector $\boldsymbol{y}$. The additive measurement noise is denoted by $\boldsymbol{v}$ with covariance $\boldsymbol{R}_v$.

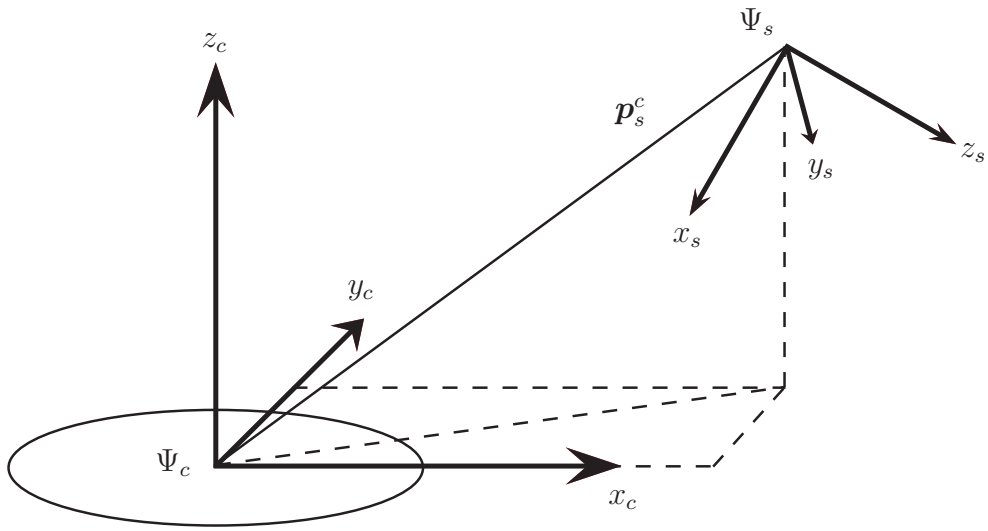

Figure 5.2: *Schematic overview of a configuration with a coil around the z axis (frame Ψ_c), and a remote sensor (Ψ_s).*

The process of predicting and updating the estimation of a state variable is schematically depicted in Figure 5.1. In between magnetic updates, the estimated uncertainty of a state variable σ_x increases due to drift caused by integration of inertial sensor signals. An actuation is required if the estimated uncertainty reaches a predefined maximum $\sigma_{x,max}$. Only the coil yielding the largest uncertainty reduction is actuated and the current applied is chosen such that the uncertainty decreases to a predefined minimum $\sigma_{x,min}$.

A schematic overview of a configuration with a coil around the z-axis is depicted in Figure 5.2. The coil frame is denoted by Ψ_c, and the sensor frame by Ψ_s. The true state vector consists of the relative position and orientation of the sensor frame with respect to the source frame: $\boldsymbol{p}_s^c$ and $\boldsymbol{\theta}_s^c$, respectively. It is chosen to use a fusion filter that operates on the errors of the state $\delta\boldsymbol{x}$, being the difference between the true state $\boldsymbol{x}$ and the estimated state $\hat{\boldsymbol{x}}$. Let $\hat{\boldsymbol{p}}_s^c$ be the estimated relative position, and $\hat{\boldsymbol{R}}_s^c$ be the relative orientation of the sensor with respect to the coil expressed as a rotation matrix. The columns of $\hat{\boldsymbol{R}}_s^c$ are the unit axes of frame Ψ_s expressed in frame Ψ_c: $\hat{\boldsymbol{R}}_s^c = \begin{pmatrix}\hat{\boldsymbol{X}}_s^c & \hat{\boldsymbol{Y}}_s^c & \hat{\boldsymbol{Z}}_s^c\end{pmatrix}$. The estimated states are related to the true states by:

$$\begin{aligned} \hat{\boldsymbol{p}}_s^c &= \boldsymbol{p}_s^c + \delta\boldsymbol{p} \\ \hat{\boldsymbol{R}}_s^c &= \boldsymbol{R}_s^c \delta\boldsymbol{R} \approx \boldsymbol{R}_s^c \left(\boldsymbol{I} + \tilde{\delta\boldsymbol{\theta}}\right), \end{aligned} \tag{5.2}$$

with $\boldsymbol{I}$ the identity matrix, $\delta\boldsymbol{p}$ the position error, $\delta\boldsymbol{\theta}$ the orientation error. Consequently, the error state is equal to $\delta\boldsymbol{x} = \begin{pmatrix}\delta\boldsymbol{p} & \delta\boldsymbol{\theta}\end{pmatrix}^T$. The tilde operator ($\tilde{}$) defines the skew-symmetric matrix form of the standard vector product:

$$\tilde{\delta\boldsymbol{\theta}} = \begin{pmatrix} 0 & -\delta\theta_z & \delta\theta_y \\ \delta\theta_z & 0 & -\delta\theta_x \\ -\delta\theta_y & \delta\theta_x & 0 \end{pmatrix}. \tag{5.3}$$

To estimate the reduction of the state covariance, we exploit the equations of an Extended Kalman Filter (EKF). Let $\boldsymbol{P}_k$ be the covariance associated with the state $\delta\boldsymbol{x}_k$ at time instant k. For a Kalman filter, a linear update rule is specified that calculates the Kalman gain $\boldsymbol{K}_k$ which is

used to transform the difference between actual and predicted measurement from measurement space to state vector space:

$$\begin{aligned}
\delta \boldsymbol{x}_k &= \boldsymbol{K}_k \delta \boldsymbol{y}_k \\
\boldsymbol{P}_k &= \left(\boldsymbol{I} - \boldsymbol{K}_k \boldsymbol{H}_k\right) \boldsymbol{P}_k^- \\
\delta \boldsymbol{y}_k &= \hat{\boldsymbol{y}}_k^- - \boldsymbol{y}_k \\
\boldsymbol{K}_k &= \boldsymbol{P}_k^- \boldsymbol{H}_k^T \left(\boldsymbol{H}_k \boldsymbol{P}_k^- \boldsymbol{H}_k^T + \boldsymbol{R}_v\right)^{-1},
\end{aligned} \tag{5.4}$$

where $\boldsymbol{H}_k$ denotes a linearized version of the measurement model $\boldsymbol{h}(\boldsymbol{x})$. It should be noted that a minus superscript $()^-$ denotes the *a priori* estimation of a variable. Thus, by using the linearized measurement model $\boldsymbol{H}_k$, the *a posteriori* covariance $\boldsymbol{P}_k$ is obtained. Moreover, by calculating the reduction of the state uncertainty for each of the coils that can be actuated, the filter can decide which coil needs to be actuated such that the reduction of the state uncertainty is highest.

The nonlinear stochastic measurement model is derived in Section 5.2.2, and validated by experiments that are described in Section 5.2.4. The derivation of the linearized measurement is shown in Section 5.2.3. Two sources of error can be defined which may lead to divergence of the fusion filter. The first source of error is the use of a linearized approximation for the nonlinear measurement model to update the state and covariance (5.4). The linear approximation introduces errors that are not covered by the update equations and can cause the filter to diverge. Another source of error is the appearance of ferromagnetic objects in the vicinity of the source or sensor, which can cause the measured magnetic field to deviate from the generated magnetic field. The filter will attribute such a deviation to an error of the state which yields an incorrect state update that may lead to divergence of the filter as well. Both sources of errors will be analyzed and discussed in the following sections.

5.2.2 Measurement Model

The estimated measurement vector $\hat{\boldsymbol{y}}$ is given by the magnetic field generated by the source coil at the location of the sensor $\hat{\boldsymbol{B}}^c(\hat{\boldsymbol{p}}_s^c)$, expressed in sensor coordinates:

$$\hat{\boldsymbol{y}} = \boldsymbol{h}(\hat{\boldsymbol{x}}) = \hat{\boldsymbol{B}}^s = \left(\hat{\boldsymbol{R}}_s^c\right)^T \hat{\boldsymbol{B}}^c(\hat{\boldsymbol{p}}_s^c). \tag{5.5}$$

The expression for the magnetic field $\hat{\boldsymbol{B}}^c(\hat{\boldsymbol{p}}_s^c)$ at the location of the sensor generated by the actuated source coil is derived by applying the Biot-Savart law [101] (Appendix A.1), resulting in:

$$\hat{\boldsymbol{B}}^c(\hat{\boldsymbol{p}}_s^c) = \frac{\mu_0 N I}{2\pi\sqrt{(\sqrt{\hat{p}_x^2 + \hat{p}_y^2} + b)^2 + \hat{p}_z^2}} \begin{pmatrix} \frac{\hat{p}_x \hat{p}_z}{\hat{p}_x^2 + \hat{p}_y^2}\left(-K(k) + \frac{b^2 + \hat{p}_x^2 + \hat{p}_y^2 + \hat{p}_z^2}{(\sqrt{\hat{p}_x^2 + \hat{p}_y^2} - b)^2 + \hat{p}_z^2} E(k)\right) \\ \frac{\hat{p}_y \hat{p}_z}{\hat{p}_x^2 + \hat{p}_y^2}\left(-K(k) + \frac{b^2 + \hat{p}_x^2 + \hat{p}_y^2 + \hat{p}_z^2}{(\sqrt{\hat{p}_x^2 + \hat{p}_y^2} - b)^2 + \hat{p}_z^2} E(k)\right) \\ K(k) + \frac{b^2 - \hat{p}_x^2 - \hat{p}_y^2 - \hat{p}_z^2}{(\sqrt{\hat{p}_x^2 + \hat{p}_y^2} - b)^2 + \hat{p}_z^2} E(k) \end{pmatrix}, \tag{5.6}$$

with μ_0 the magnetic permeability of vacuum ($4\pi \cdot 10^{-7}$ T $\cdot$ m^2/A), N the number of windings, I the current applied, b the radius of the coil, and:

$$\begin{aligned} k &= \sqrt{\frac{4b\sqrt{\hat{p}_x^2+\hat{p}_y^2}}{(\sqrt{\hat{p}_x^2+\hat{p}_y^2}+b)^2+\hat{p}_z^2}} \\ K(k) &= \int_0^{\pi/2} \frac{1}{\sqrt{1-k^2\sin^2\phi}} d\phi \\ E(k) &= \int_0^{\pi/2} \sqrt{1-k^2\sin^2\phi} d\phi. \end{aligned} \tag{5.7}$$

It should be noted that the indices $()_s^c$ have been omitted for readability. Solving the elliptic integrals $E(k)$ and $K(k)$ for every time step can be rather time consuming. The expression for the magnetic flux density (5.6) can be simplified by assuming the point of interest satisfies $\sqrt{\hat{p}_x^2+\hat{p}_y^2+\hat{p}_z^2} \gg b$, which means the coil is viewed as a magnetic dipole resulting in:

$$\hat{\boldsymbol{B}}^c(\hat{\boldsymbol{p}}_s^c) = \frac{\mu_0 N I b^2}{4\left(\hat{p}_x^2+\hat{p}_y^2+\hat{p}_z^2\right)^{\frac{5}{2}}} \begin{pmatrix} 3\hat{p}_x\hat{p}_z \\ 3\hat{p}_y\hat{p}_z \\ 2\hat{p}_z^2-\hat{p}_x^2-\hat{p}_y^2 \end{pmatrix}. \tag{5.8}$$

5.2.3 Linearized Measurement Model

In order to determine the reduction of the uncertainty associated with the state and to determine which coil has to be actuated, the first-order linearized measurement model (Jacobian) needs to be derived. The Jacobian $\boldsymbol{H}$, consisting of the partial derivatives of the function $\boldsymbol{h}(\hat{\boldsymbol{x}})$ with respect to the error state $\delta\boldsymbol{x}$ is given by:

$$\boldsymbol{H} = \begin{pmatrix} \frac{\partial \hat{\boldsymbol{B}}^s}{\partial \delta \boldsymbol{p}} & \frac{\partial \hat{\boldsymbol{B}}^s}{\partial \delta \boldsymbol{\theta}} \end{pmatrix} = \begin{pmatrix} \left(\hat{\boldsymbol{R}}_s^c\right)^T \frac{\partial \hat{\boldsymbol{B}}^c}{\partial \delta \boldsymbol{p}} & \frac{\partial \left(\hat{\boldsymbol{R}}_s^c\right)^T}{\partial \delta \boldsymbol{\theta}} \hat{\boldsymbol{B}}^c \end{pmatrix}. \tag{5.9}$$

The partial derivatives of the estimated field with respect to the position error ($\left(\hat{\boldsymbol{R}}_s^c\right)^T \frac{\partial \hat{\boldsymbol{B}}^c}{\partial \delta \boldsymbol{p}}$) result in rather lengthy and complicated expressions for the analytical model (Appendix A.2). For the dipole approximation of the magnetic field, the results are more straightforward and as an example the partial derivative with respect to the first error state is given by:

$$\left(\hat{\boldsymbol{R}}_s^c\right)^T \frac{\partial \hat{\boldsymbol{B}}^c}{\partial \delta p_x} = \left(\hat{\boldsymbol{R}}_s^c\right)^T \frac{\mu_0 N I b^2}{4\left(\hat{p}_x^2+\hat{p}_y^2+\hat{p}_z^2\right)^{\frac{7}{2}}} \begin{pmatrix} -12\hat{p}_x^2\hat{p}_z+3\hat{p}_y^2\hat{p}_z+3\hat{p}_z^3 \\ -15\hat{p}_x\hat{p}_y\hat{p}_z \\ 3\hat{p}_x^3+3\hat{p}_x\hat{p}_y^2-12\hat{p}_x\hat{p}_z^2 \end{pmatrix}. \tag{5.10}$$

A complete derivation of the partial derivatives of the estimated field with respect to the position error are shown in Appendix A.2. The partial derivatives of the estimated field to the orientation are given by:

$$\frac{\partial \left(\hat{\boldsymbol{R}}_s^c\right)^T}{\partial \delta \boldsymbol{\theta}} \hat{\boldsymbol{B}}^c = \frac{\partial}{\partial \delta \boldsymbol{\theta}} \left(\boldsymbol{R}_s^c \delta \boldsymbol{R}\right)^T \hat{\boldsymbol{B}}^c = \frac{\partial}{\partial \delta \boldsymbol{\theta}} \left(\boldsymbol{I} - \tilde{\delta\boldsymbol{\theta}}\right) \left(\boldsymbol{R}_s^c\right)^T \hat{\boldsymbol{B}}^c = \frac{\partial}{\partial \delta \boldsymbol{\theta}} \left(\hat{\boldsymbol{B}}^s + \tilde{\hat{\boldsymbol{B}}}^s \delta\boldsymbol{\theta}\right) = \tilde{\hat{\boldsymbol{B}}}^s, \tag{5.11}$$

with $\hat{\boldsymbol{B}}^s$ the estimation of the magnetic field generated by the source at the location of the sensor expressed in sensor coordinates.

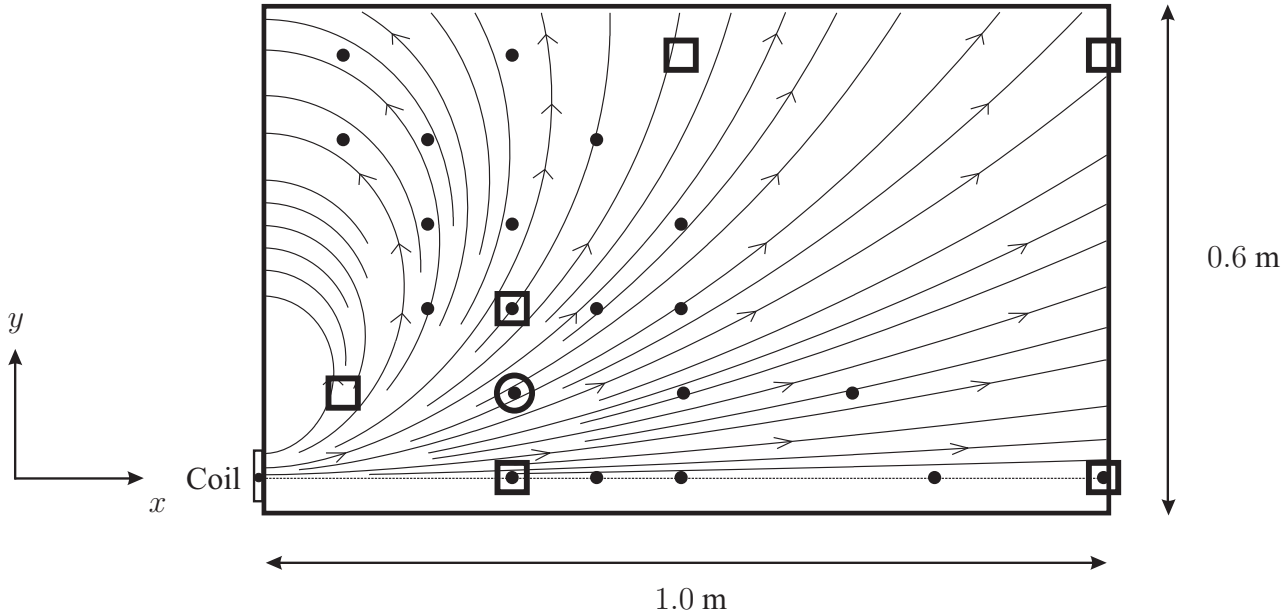

Figure 5.3: *Schematic drawing of the 2D measurement setup with the sensor positions used for validation of the nonlinear measurement model (dots), the linearized model (circle) and the influence of a magnetic disturbance (circle). The positions of the ferromagnetic object are indicated by the squares. The seventh position of the ferromagnetic object ($(x, y) = (2.0, 0.0)$ m) is not shown. The lines with arrows indicate the magnetic field lines of the magnetic field generated by the coil.*

5.2.4 Experimental Methods

To evaluate the performance of the stochastic magnetic measurement model, several aspects of the stochastic measurement model were validated by experiments. The measurement setup consisted of a x-y positioning table with a single coil around the x-axis at the origin as shown in Figure 5.3. It should be noted that the z-position was not varied during the measurements, since the magnetic field generated by the coils is axially symmetric. Moreover, the orientation of the sensor was not changed during the measurements as this will not affect the strength of the magnetic field, but the distribution of the individual components only. An error in the estimation of orientation will, however, affect the update of the states calculated by the fusion filter. The measurements were done using the magnetometer (thin film magnetoresistive) of a MTx sensor (Xsens Technologies B.V.). The signals were acquired at a sample rate of 100 Hz. The noise level of the sensors σ_v was determined to be 0.3 mG. During a measurement, the magnetometer measures the sum of the earth magnetic field and the actuated magnetic field. Pulse values were determined by subtracting the signal without actuation from the signal with actuation. The coil was a circular coil with 50 windings and a radius of 0.055 m. The coil was actuated each second at a current of 0.91 A using a pulse width of 100 ms (10 samples).

The experiment consisted of three parts. First, the accuracy of the nonlinear measurement model was validated by placing the sensor at known positions and measuring the responses. The positions are indicated by the dots in Figure 5.3, and were chosen to cover the largest part of the magnetic field in the measurement volume. The accuracy was evaluated by comparing the responses to a prediction of the magnetic field at the known positions using the nonlinear

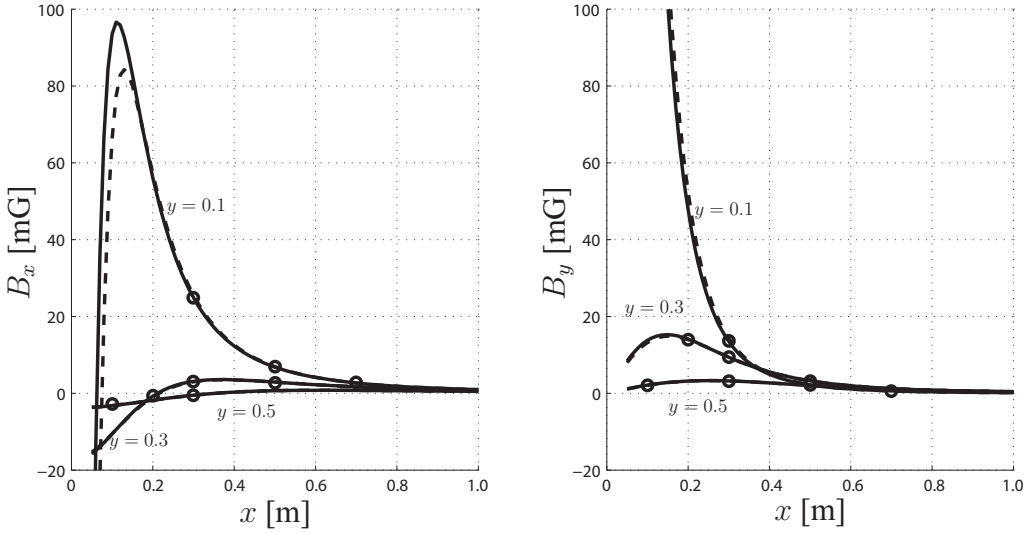

Figure 5.4: *Components of the magnetic field (B_x left, B_y right) for the predicted magnetic field (lines) and measured magnetic field (circles) for varying x position at constant y position at an actuation current of 0.91 A. The predictions were made using the analytical model (solid) and the dipole approximation (dashed).*

model. Both the dipole approximation as well as the analytical model were evaluated. Second, the accuracy of the linearized model was validated by placing the sensor at position $(x, y) = (0.3, 0.1)$ m, indicated by the circle in Figure 5.3. Subsequently, the position was varied around the initial position in steps of 5 mm in positive x and y direction with a maximum of 5 cm. The accuracy of the magnetic field change was evaluated by comparison to the change predicted by the Jacobian using the dipole approximation as well as the analytical model. Third, the influence of a ferromagnetic disturbance was evaluated by placing the sensor at a fixed position ($(x, y) = (0.3, 0.1)$ m, circle in Figure 5.3) and placing a ferromagnetic object (iron cylinder with radius and height of 0.05 m) at several positions around the sensor, as indicated by the squares in Figure 5.3. By comparing the disturbed response at each position of the ferromagnetic object to the undisturbed response, the influence of the disturbance is determined.

5.3 Results

5.3.1 Validation of the Nonlinear Measurement Model

For validation of the nonlinear measurement model, the sensor was placed at the positions indicated by the dots in Figure 5.3. A comparison between the measured magnetic field components and the predicted magnetic field components for varying x positions and a few constant y positions using the analytical model and the dipole approximation are shown in Figure 5.4. The analytical model is accurate, as confirmed by the rms differences which were calculated as 0.50 ± 0.22 mG (mean $\pm$ standard deviation) for the x direction, and 0.14 ± 0.06 mG for the y direction. Moreover, the figure clearly indicates the increasing error of the dipole approximation for sensor locations near the source. The rms differences using the dipole approximation were calculated as 0.53 ± 0.27 mG for the x direction, and 0.18 ± 0.15 mG for the y direction.

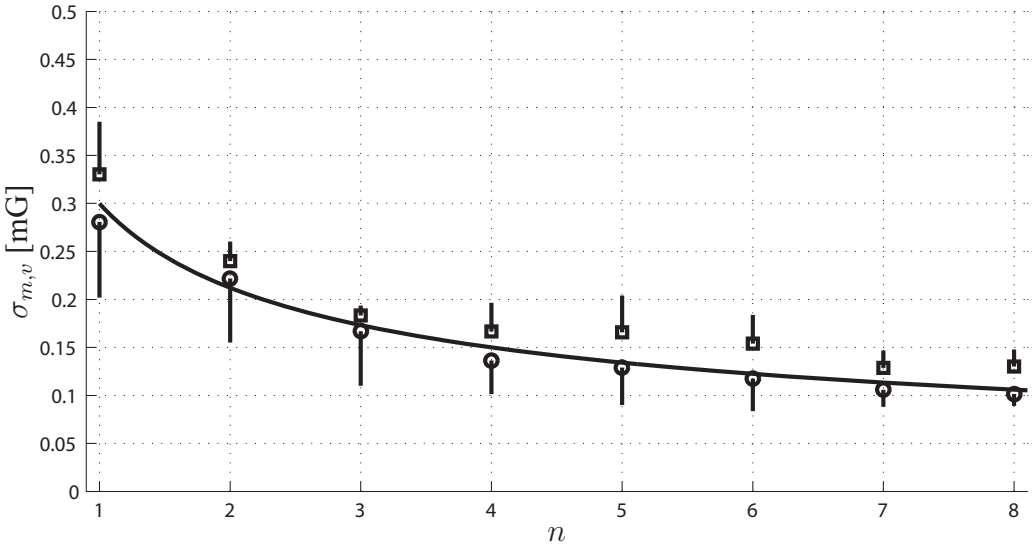

Figure 5.5: *Standard deviation of the sample mean $\sigma_{m,v}$ as a function of the number of samples n used to calculate the mean. The estimated average of $\sigma_{m,v}$ and its standard deviation are indicated by the dots (x: circle, y: square) and vertical lines, respectively. It should be noted that the standard deviation is only shown at a single side of the mean for visualization reasons. The solid line indicates the predicted decrease of $\sigma_{m,v}$.*

To construct Figure 5.4 and to calculate the rms differences, all samples except the first and the last of each pulse were used for averaging. The first and last samples were not used, because they may have occurred in the rising or falling edge of a pulse. To prevent the magnetic field to change by sensor movement during a pulse, the number of samples should be as small as possible. This will, however, decrease the accuracy which is graphically depicted in Figure 5.5. The figure shows the decrease of the standard deviation of the sample mean $\sigma_{m,v}$ as a function of the number of samples used to calculate the mean. The predicted $\sigma_{m,v}$ (solid line) is calculated by: $\sigma_{m,v} = \frac{\sigma_v}{\sqrt{n}}$, with n being the number of samples [102].

5.3.2 Validation of the Linearized Measurement Model

A comparison of the change of magnetic field components by an increase of the sensor position in x direction starting at position $(x, y) = (0.3, 0.1)$ m is shown in Figure 5.6. The figure clearly shows the error caused by the linear approximation of the nonlinear field using the Jacobian. As expected, the error increases more when the dipole approximation is used, compared to when the analytical model is used. In order to analyze the errors caused by the use of the linearized measurement model, the percentage difference between the magnetic fields estimated by the linearized and nonlinear model were calculated at a predefined uncertainty of the estimated position for the complete measurement volume (Figure 5.7). The predefined uncertainty, which can be viewed as the position change in Figure 5.6, was chosen to be 0.03 m for the x and y direction as an example. The percentage difference is calculated by dividing the magnitude of the field difference between the linearized model and the nonlinear model at the predefined uncertainty (0.03 m) by the magnitude of the field at the current position. The figure shows an increase in percentage difference due to the use of the linearized model for sensor locations near the source. Since we used a linear approximation of the nonlinear measurement model, the

error levels (Figure 5.7) can be viewed as the higher order terms of the Taylor approximation of the nonlinear measurement model, of which the second order term will be dominant. This is confirmed by the similar shape of the levels in Figure 5.7 compared to Figure 5.8, which shows the magnitude of the second order spatial derivative divided by the magnitude of the magnetic field.

5.3.3 Influence of a Ferromagnetic Disturbance

The influence of a ferromagnetic object on the measurements of the magnetic field is indicated by Figure 5.9. The figure shows the percentage difference for the x and y direction between the disturbed and undisturbed magnetic field with the sensor at a fixed position ($(x, y) = (0.3, 0.1)$ m), and varying positions of the ferromagnetic object (Figure 5.3). The percentage difference at the location of the sensor due to the use of the linearized model for an uncertainty of 0.03 m in x and y direction (Figure 5.7) is indicated by the solid and dashed line, respectively. From the figure it becomes clear that the measurements will be influenced only when the ferromagnetic object is located near or between the source and the sensor.

To analyze the effect of a ferromagnetic disturbance on the estimation of position and orientation, updates of the state and covariance were calculated in a disturbed and an undisturbed environment using (5.4). Assume the sensor to be located at position ($\hat{\boldsymbol{p}}_s^c = \begin{pmatrix} 0.3 & 0.1 & 0.0 \end{pmatrix}^T$

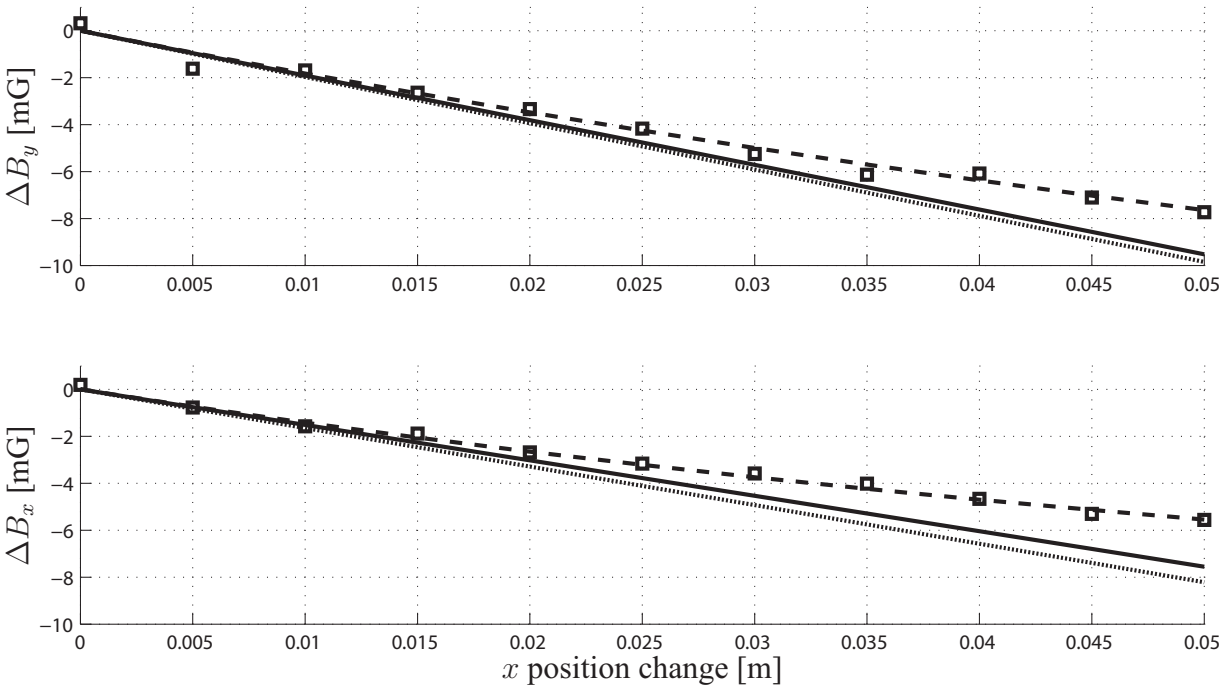

Figure 5.6: *Validation of the Jacobian by comparing the change of the magnetic field for the x direction (top figure) and y direction (bottom figure) due to an increase in positive x position of the sensor starting at $(x, y) = (0.3, 0.1)$ m. The actual field measured by the magnetometer is indicated by the squares, the prediction using the nonlinear model is indicated by the dashed line. The prediction of the field change using the Jacobian calculated from the analytical model is indicated by the solid line. The prediction of the field change using the Jacobian calculated from the dipole approximation is indicated by the dotted line.*

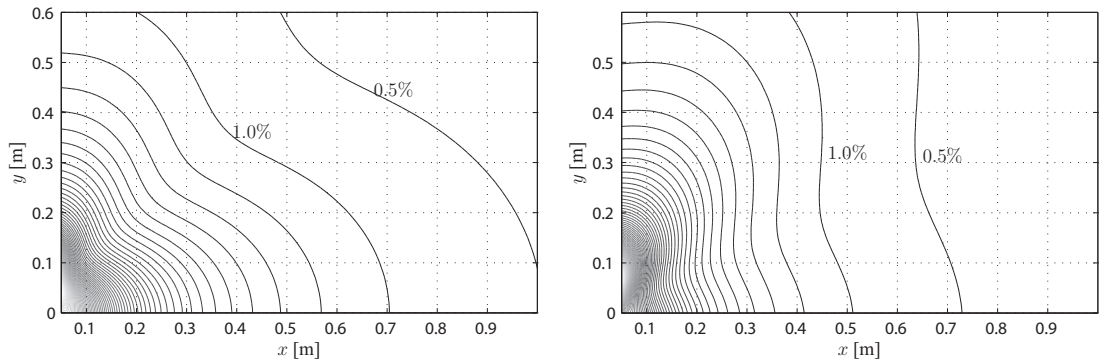

Figure 5.7: *Percentage difference between the magnetic fields estimated by the linearized and nonlinear model for a position uncertainty of* 0.03 *m in* x *direction (left) and* y *direction (right). Each line indicates an increase of* 0.5%.

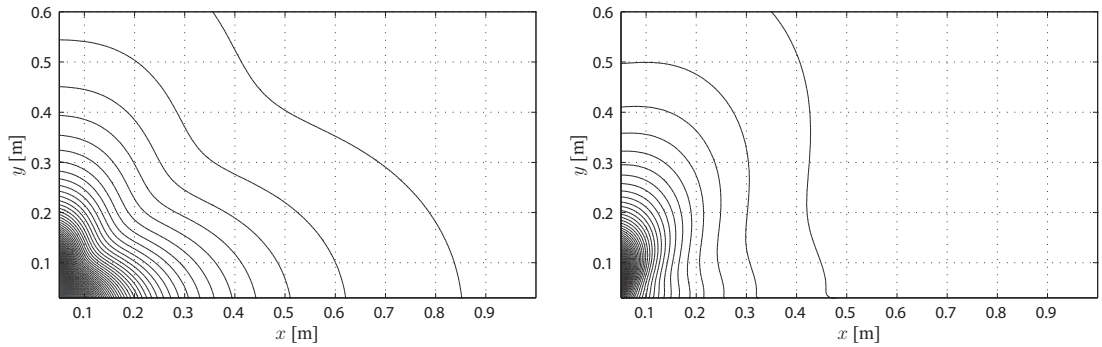

Figure 5.8: *Magnitude of the second order spatial derivative of the magnetic field to* x *(left) and* y *(right), divided by the magnitude of the magnetic field.*

m) and an orientation aligned with the coil frame ($\hat{\boldsymbol{R}}_s^c = \boldsymbol{I}$). The position and orientation error are assumed to be 0.01 m and 0.01 rad, respectively, which means for the covariance matrix $\boldsymbol{P}_k^- = 0.01^2 \cdot \boldsymbol{I}$. The measurement noise is assumed to be uncorrelated, which means the covariance is given by $\boldsymbol{R}_v = \sigma_v^2 \cdot \boldsymbol{I}$. The percentage differences between the calculated update using the measurement with a ferromagnetic object between the source and the sensor ($\boldsymbol{p} = \begin{pmatrix} 0.1 & 0.1 & 0.0 \end{pmatrix}^T$ m, Figure 5.9) and the correct update (initial position and orientation error: $\delta\boldsymbol{x} = \begin{pmatrix} 0.01 & 0.01 & 0.01 & 0.01 & 0.01 & 0.01 \end{pmatrix}^T$) were calculated to be 81% for the x direction, 47% for the y direction, and 92% for the z direction. If the undisturbed measurement is used, the percentage differences were calculated to be 6%, 18%, and 6% for the x, y, and z directions, respectively. Yet, the reduction of the covariance $\boldsymbol{P}_k$ is updated equally, yielding inconsistent behaviour of the filter in a disturbed environment.

5.4 Discussion

In this study, a stochastic magnetic measurement model is proposed that can be used in a fusion filter to estimate relative positions and orientations. The model is used to predict the magnetic field generated by a single coil, measured by a remote 3D magnetic sensor, based on an estimation of the relative position and orientation of the remote sensor with respect to the source. Compared to existing models (e.g. [34]), the calculations are not based on the dipole

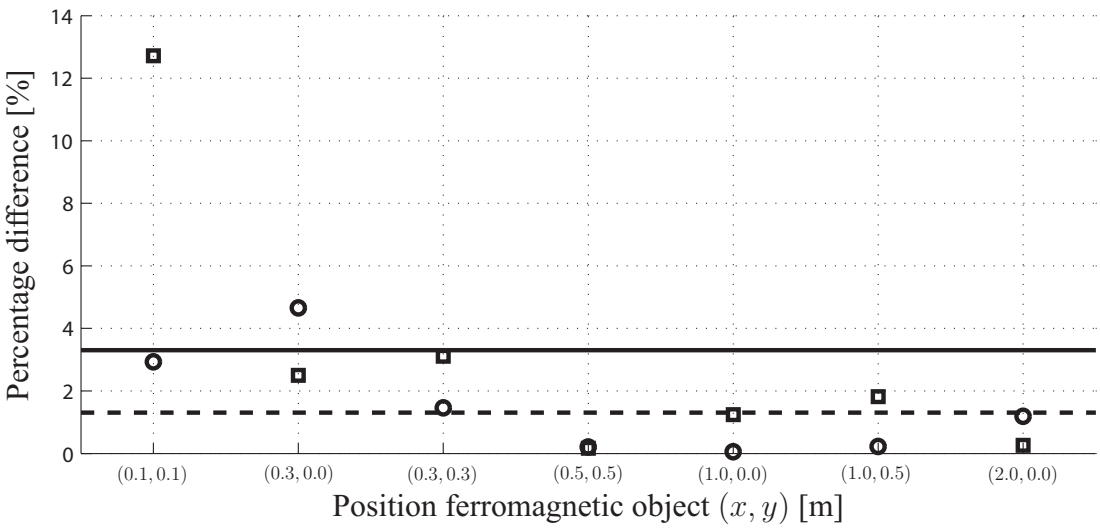

Figure 5.9: *Percentage difference between measured magnetic field (x circles, y squares) with ferromagnetic disturbance and undisturbed field at sensor position $(x, y) = (0.3, 0.1)$ m, and varying positions of the ferromagnetic object. The percentage difference due to the use of the linearized model at the position of the sensor with an uncertainty of 0.03 m is indicated by lines (x uncertainty solid, y uncertainty dashed).*

approximation of the source, and do not require the source coils to be mounted orthogonally or to share the same origin. The model is accurate, which is confirmed by the small rms differences between the predicted magnetic field and the measured magnetic field. When the dipole approximation is used, the errors increase as expected, especially for sensor locations near the source coil. The use of a linearized measurement model to update the state, and the appearance of a ferromagnetic object in the vicinity of source and sensor were defined as two sources of error that may lead to divergence of the fusion filter. It appeared that the linearized model introduces errors which generally increase for sensor locations near the source. Moreover, it was shown that the errors are dependent on the second order spatial derivative of the magnetic field. As expected [103, 104], it appeared that a ferromagnetic object influences the measurements only if it is located near or between the source and sensor, making the system insensitive for most ferromagnetic objects in the environment. It was shown in Section 5.3.3 that a ferromagnetic object in the vicinity of the sensor may lead to inconsistent behaviour of the fusion filter. It should be noted that a part of the error for both the disturbed and undisturbed case is caused by the use of the linearized model. To prevent inconsistent behaviour of the filter, the filter should update regularly to limit the growth of the state uncertainty. Moreover, it is important to remove any ferromagnetic objects in the vicinity of the source or sensor. Unlike heading estimation systems using the earth magnetic field [105], the proposed measurement system is insensitive to ferromagnetic objects in the environment outside the range of the configuration.

The disturbance due to a ferromagnetic object in the vicinity of the source or sensor can be caused by two phenomena, eddy currents and ferromagnetism. Eddy currents are induced in conductive objects in the vicinity of the source or sensor by a changing magnetic field, which occurs during the rising and falling edges of a magnetic pulse. After the pulse has reached its steady state value, the eddy currents decay at an exponential rate with a time constant defined by the ratio between inductance and resistance of the object [101]. For the iron object used in the experiments, the time constant will be in the order of micro seconds. This means that the eddy

currents did not have a noticeable effect on the experiments performed in the present study, since the sample time was set to 10 ms. The magnetization field produced by ferromagnetic materials in the vicinity of the source or sensor persists while the magnetic actuation is applied, where the magnitude of the magnetization field depends on the permeability of the material. This means that the disturbances presented in Figure 5.9 can be attributed to ferromagnetism.

Figure 5.5 indicates that a large number of samples is preferable for accuracy, but must be kept small to limit the disturbance caused by movements during a pulse. The time needed to acquire enough samples can be decreased by increasing the sample frequency of the magnetometers. However, as stated, eddy currents will be induced due to the rising and falling edge of a pulse, which will generate secondary magnetic fields in conducting objects near the source or sensor. Before sampling at high frequency, some time should be allowed for the eddy currents to decay. When sampling at high frequency, the bandwidth of the magnetometer noise should be kept in mind to prevent correlation between measurement noise samples.

The measurement setup used in this study was able to generate constant (DC) magnetic fields only. It could be interesting to investigate the use of time varying (AC) magnetic fields. The main reason to use DC magnetic fields is they are less sensitive to metallic object interference, since only the rising and falling edge of a pulse will generate eddy currents. AC magnetic fields offer the possibility to actuate multiple coils simultaneously while less energy is used. However, the changing magnetic field induces eddy currents continuously, which need to be taken into account. Moreover, the equations used to predict the magnetic field will become time dependent which increases the complexity. Still, from an energetic point of view, it is interesting to investigate the possibility of using AC magnetic fields.

The coil used for the experiments was a circular coil consisting of 50 windings which were assumed to be of infinitesimal thickness. In reality, however, each individual winding will have a certain thickness and the coil does not necessarily have to be a perfect circular shape. This incorrect assumption introduces a systematic error into the system, that will be different for each coil configuration. An improvement could be to model each individual coil by applying the Biot-Savart law [101], or by using a numerical lookup table for the magnetic field at each position and orientation. In principle, for the method proposed, any coil geometry can be used, as long as the mapping function $\boldsymbol{h}(\boldsymbol{x})$ and its partial derivatives are known. For human motion applications, the coils could be placed around body segments or integrated within clothes such that it does not impede normal functioning. Moreover, the dimensions of the coil (e.g. number of windings, coil radius) can be optimized with respect to the range that should be covered by that coil. Also, several coil radii or higher actuation currents can be used when large distances need to be covered. For a sufficient signal to noise ratio, the range of the coil used in the current setup is limited to about 80 cm.

The measurement model proposed in the present study will be used in an adaptive filter structure in (Chapter 6). The state variables, the position and orientation of the source and sensors, will be estimated using the accelerometer and gyroscope signals of inertial sensors. The filter estimates the uncertainty associated with each state variable. If the uncertainty associated with one of the state variables exceeds a predefined threshold, the filter decides to perform a magnetic actuation. In case of a multiple coil configuration, the equations used to update the state (5.4) can be used to choose the coil resulting in the largest reduction of the uncertainty. Also, the current applied can be chosen such that the uncertainty reduces as desired, or that a certain signal to noise ratio is achieved. The signal to noise ratio can be calculated easily by dividing the predicted field by the noise level. The final objective of the fusion filter is to achieve maximal accuracy at minimal energy consumption.

6

Ambulatory Human Motion Tracking by Fusion of Inertial and Magnetic Sensing with Adaptive Actuation

H.M. Schepers, D. Roetenberg, and P.H. Veltink

Submitted

Abstract

Over the last years, inertial sensing has proven to be a suitable ambulatory alternative to traditional human motion tracking based on optical position measurement systems which are generally restricted to a laboratory environment. Besides many advantages, a major drawback is the inherent drift caused by integration of acceleration and angular velocity to obtain position and orientation. Additionally, inertial sensing can not be used to estimate relative positions and orientations of sensors with respect to each other. To overcome these drawbacks, this study presents an Extended Kalman Filter for fusion of inertial and magnetic sensing that is used to estimate relative positions and orientations. In between magnetic updates, change of position and orientation are estimated using inertial sensors. The system decides to perform a magnetic update only if the estimated uncertainty associated with the relative position and orientation exceeds a predefined threshold. The filter is able to provide a stable and accurate estimation of relative position and orientation for several types of movements, as indicated by the average rms error being 0.033 m for the position and 3.6 degrees for the orientation.

6.1 Introduction

Traditionally, biomechanical studies employ optical motion tracking systems for the determination of position and orientation in a local, room-based coordinate system. This constrains the experiments to the calibrated volume of the camera system, although the cameras may move. As an alternative to the optical motion tracking system, several research groups propose the use of inertial sensors (accelerometers and gyroscopes) as an alternative. Besides the many advantages of these sensors compared to optical measurement systems, the inherent drift due to the unavoidable integration over time of sensor signals to obtain position and orientation introduces large errors. Moreover, it is not possible to estimate positions of inertial sensor modules with respect to each other. Although the integration drift can be reduced by using suitable estimation algorithms [28, 51, 96, 16], by using the orientations of individual body segments in a linked segment model [106, 107], or by applying suitable initial and final conditions and a limited integration time [70, 56], a stable and robust solution to estimate relative positions of sensors with respect to each other is required.

The estimation of relative positions between body segments, preferably in an ambulatory environment, is important in many applications. An example is the relation between the center of mass and the center of pressure for balance assessment. In Chapter 4, we proposed a method to estimate this relation by using shoes instrumented with force/moment sensors and inertial sensors. The results were promising, but the relative position between the feet as well as the vertical distance between center of mass and center of pressure could not be assessed. Other examples are the estimation of relative positions in virtual reality applications [33], or to quantify mechanical loading [108].

A solution for the estimation of relative body positions is to fuse an inertial sensor system with a magnetic tracking system. An advantage of fusion with magnetic tracking [33] compared to other tracking solutions such as optical [30], acoustical [31], Ultra-Wide Band (UWB) [32] or GPS [29] is that it does not suffer from loss or degradation of the signal which can occur especially in indoor environments, or line-of-sight problems since the human body is transparent for the magnetic field applied. Roetenberg *et al.* [34] proposed an ambulatory magnetic position and orientation measurement system, that was fused with an inertial sensor system using a complementary Kalman filter structure in a successive study [35]. Although the system is able to estimate relative body positions and orientations accurately using a measurement system worn on the body, some important aspects of the system need to be improved. First, the estimation algorithm is based on the dipole approximation of the source and requires all three coils to be mounted orthogonally and to share the same origin. Second, all source coils need to be actuated every update with a fixed update rate. Third, the fusion filter first estimates the position and orientation from the magnetic measurements which are then fed into the fusion filter as a measurement input. This means, the stochastic characteristics of the magnetic measurement system are not propagated through the fusion filter.

In order to assess these aspects, this study proposes and evaluates an alternative algorithm for relative position and orientation estimation that does not depend on a fixed coil configuration or dipole approximation, allows an optimal choice of actuation parameters, and uses the actual magnetic field that is measured as an input to the fusion filter. A complementary Kalman filter structure is presented that uses a measurement model which has been presented in Chapter 5. The filter predicts the position and orientation based on the signals measured by the accelerometer and gyroscope of the inertial sensor. If the uncertainty associated with the relative position or orientation exceeds a predefined threshold, the system decides to perform a

magnetic actuation. Moreover, only the coil that delivers most information is actuated. In this way, the system achieves high accuracy at relatively low energy consumption.

6.2 Methods

6.2.1 Relative Position and Orientation Determination

Change of position and orientation can be estimated by integration of acceleration and angular velocity signals obtained from inertial sensor modules. In this study, inertial sensing is fused with a magnetic measurement system to estimate relative position and orientation of the sensor with respect to the magnetic source, $\boldsymbol{p}_s^c$ and $\boldsymbol{R}_s^c$, respectively. Figure 6.1 shows the measurement system used to estimate the relative position and orientation of an Inertial and Magnetic Measurement System (IMMS) with respect to the magnetic source. The IMMS contains a 3D accelerometer, a 3D gyroscope, and a 3D magnetometer. A schematic overview of a configuration with a coil around the z-axis is shown in Figure 6.2. The global frame is denoted by Ψ_g, the magnetic source frame by Ψ_c, the coil frame by Ψ_{cz}, the sensor frame by Ψ_s and the estimated sensor frame by $\hat{\Psi}_s$. It should be noted that the coil frame Ψ_{cz} is rigidly connected to magnetic source frame Ψ_c. The reason to include both is that the magnetic source can have multiple coils attached to it with individual relative positions and orientations with respect to the magnetic source. Both the movement of the source and sensor should be estimated, since the source and sensor can move independently. Orientation is estimated by integration of angular

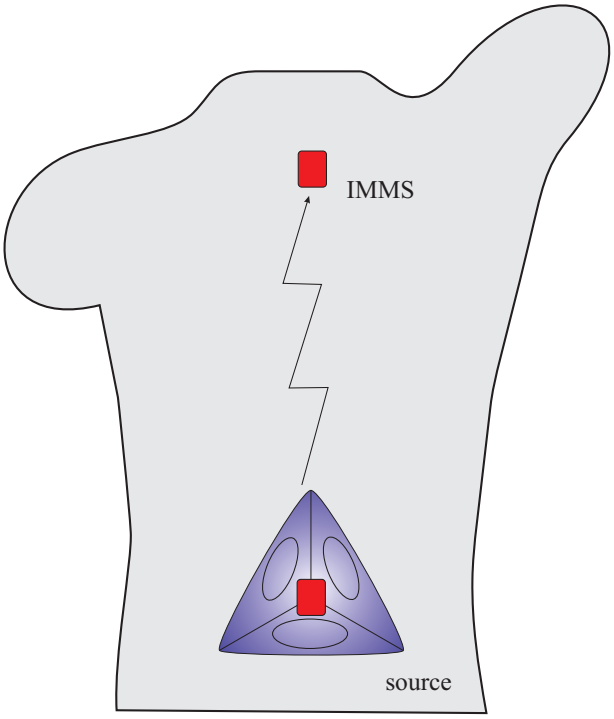

Figure 6.1: *Overview of the measurement system used to estimate relative positions and orientations of an Inertial and Magnetic Measurement System (IMMS) with respect to the source. The source consists of three circular coils that are mounted orthogonally with respect to each other. An additional IMMS is mounted on the source to estimate its movement.*

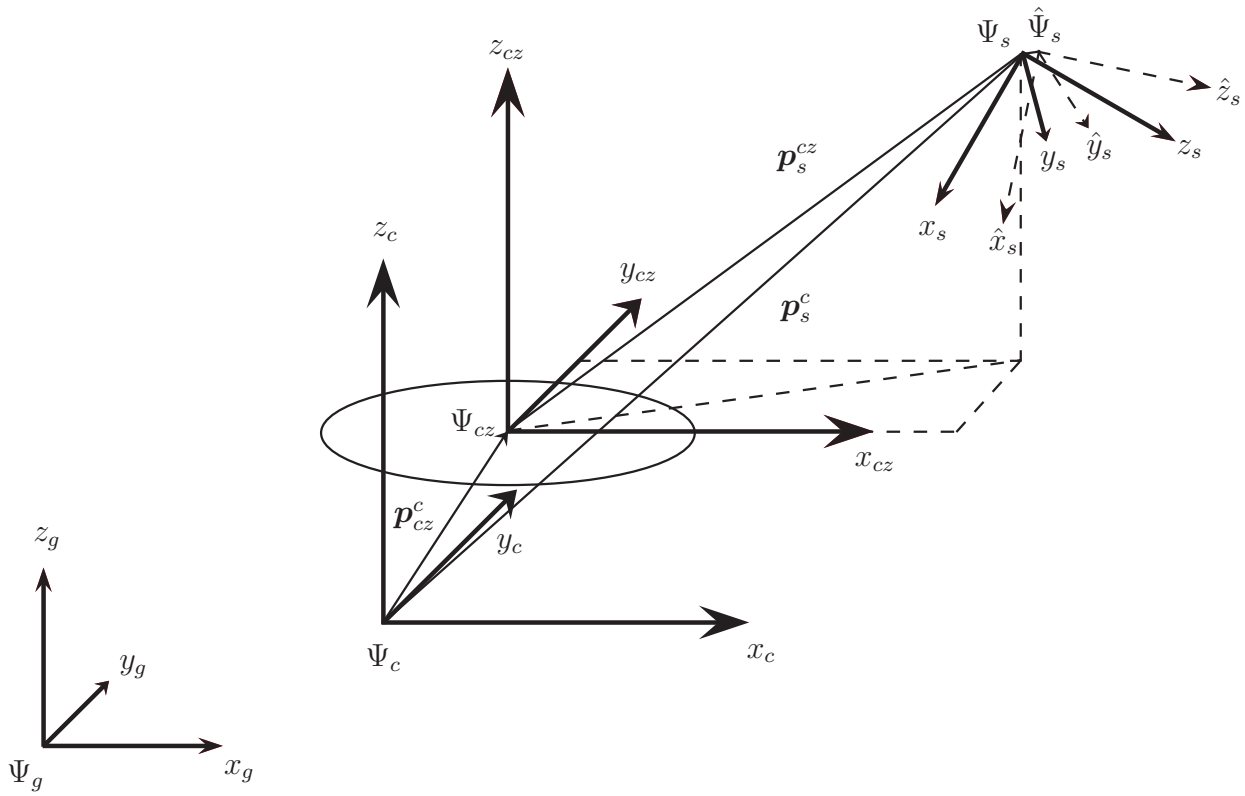

Figure 6.2: *Relation between true sensor frame Ψ_s, estimated sensor frame $\hat{\Psi}_s$, magnetic source frame Ψ_c, local coil frame Ψ_{cz} and global frame Ψ_g with a coil around the z axis. The relative position of the sensor with respect to the magnetic source is denoted by $\boldsymbol{p}_s^c$, the relative position of the coil with respect to the magnetic source by $\boldsymbol{p}_{cz}^c$, and the relative position of the sensor with respect to the coil by $\boldsymbol{p}_s^{cz}$.*

velocity using the following differential equation [59]:

$$\dot{\boldsymbol{R}}_s^g = \boldsymbol{R}_s^g \tilde{\boldsymbol{\omega}}_s^{s,g}, \tag{6.1}$$

where $\boldsymbol{R}_s^g$ denotes the rotation matrix describing the orientation of the sensor frame Ψ_s with respect to the global frame Ψ_g. The columns of $\boldsymbol{R}_s^g$ are the unit axes of frame Ψ_s expressed in frame Ψ_g: $\boldsymbol{R}_s^g = \begin{pmatrix} \boldsymbol{X}_s^g & \boldsymbol{Y}_s^g & \boldsymbol{Z}_s^g \end{pmatrix}$. The angular velocity $\boldsymbol{\omega}_s^{s,g}$ of frame Ψ_s with respect to Ψ_g, expressed in Ψ_s as measured by the inertial sensor is represented in skew-symmetric matrix form, indicated by the tilde operator ($\tilde{}$):

$$\tilde{\boldsymbol{\omega}}_s^{s,g} = \begin{pmatrix} 0 & -\omega_z & \omega_y \\ \omega_z & 0 & -\omega_x \\ -\omega_y & \omega_x & 0 \end{pmatrix}, \tag{6.2}$$

where the indices $()_s^{s,g}$ have been omitted for readability. The accelerometer signal consists of a sensor acceleration component $\boldsymbol{a}^s$ and a gravitational acceleration component $\boldsymbol{g}^s$: $\boldsymbol{s}^s = \boldsymbol{a}^s - \boldsymbol{g}^s$. The orientation $\boldsymbol{R}_s^g$ is used to remove the gravitational acceleration ($\boldsymbol{a}^g = \boldsymbol{R}_s^g \boldsymbol{s}^s + \boldsymbol{g}^g$) [70], and the change of position in global coordinates is obtained by double integration of the sensor acceleration component $\boldsymbol{a}^g$. It should be noted that the orientation of the source with respect to the global $\boldsymbol{R}_c^g$ is obtained in a similar way using the acceleration $\boldsymbol{s}^c$ measured by the accelerometer of the inertial sensor attached to the source, and its angular velocity $\boldsymbol{\omega}_c^{c,g}$ measured by the gyroscope.

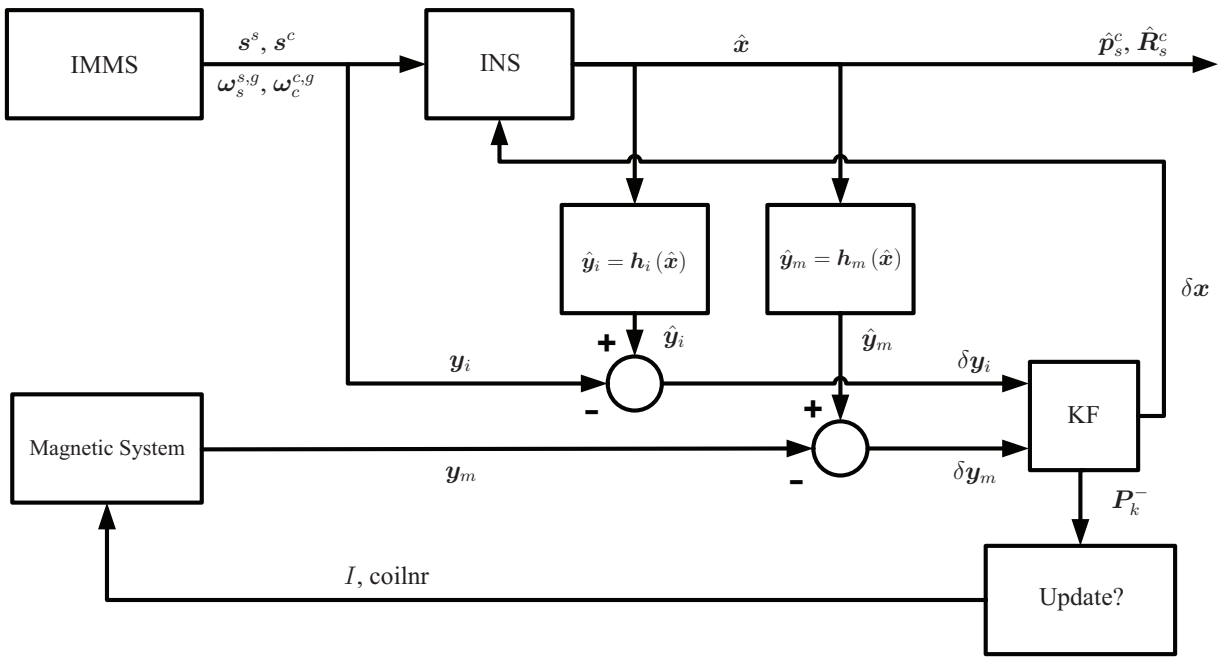

Figure 6.3: *Structure of the Extended Kalman Filter (EKF). Measurements obtained from the Inertial and Magnetic Measurement System (IMMS) are used to estimate the position and orientation of the sensor with respect to the source ($\hat{\boldsymbol{p}}_s^c$ and $\hat{\boldsymbol{R}}_s^c$) in an Inertial Navigation System (INS). A Kalman Filter (KF) uses an inclination update $\delta\boldsymbol{y}_i$ and a magnetic update $\delta\boldsymbol{y}_m$ to improve the estimation of $\hat{\boldsymbol{p}}_s^c$ and $\hat{\boldsymbol{R}}_s^c$. Based on an estimation of the uncertainty of the position and orientation $\boldsymbol{P}_k^-$, the system decides if a magnetic update is needed. It also decides which coil needs to be actuated (coilnr) and which actuation current (I) should be used.*

The relative orientation of the sensor with respect to the magnetic source $\boldsymbol{R}_s^c$ is obtained by:

$$\dot{\boldsymbol{R}}_s^c = \boldsymbol{R}_s^c \tilde{\boldsymbol{\omega}}_s^{s,c}, \tag{6.3}$$

where the angular velocity is given by the difference between the angular velocities of the sensor and the source, both expressed in the same coordinate system:

$$\boldsymbol{\omega}_s^{s,c} = \boldsymbol{\omega}_s^{s,g} - \left(\boldsymbol{R}_s^g\right)^T \boldsymbol{R}_c^g \boldsymbol{\omega}_c^{c,g}. \tag{6.4}$$

Subsequently, the relative position $\boldsymbol{p}_s^c$ is obtained by:

$$\begin{aligned}
\boldsymbol{a}_s^c &= \left(\boldsymbol{R}_c^g\right)^T \left(\boldsymbol{R}_s^g \boldsymbol{s}^s - \boldsymbol{R}_c^g \boldsymbol{s}^c\right) = \boldsymbol{R}_s^c \boldsymbol{s}^s - \boldsymbol{s}^c \\
\boldsymbol{v}_s^c &= \boldsymbol{v}_0 + \int_{t_0}^{t} \boldsymbol{a}_s^c(\tau) d\tau \\
\boldsymbol{p}_s^c &= \boldsymbol{p}_0 + \int_{t_0}^{t} \boldsymbol{v}_s^c(\tau) d\tau.
\end{aligned} \tag{6.5}$$

6.2.2 Filter Structure

In this study, a complementary filter, commonly used for inertial navigation [102], is designed which operates on the errors of the state variables using a feedback structure (Figure 6.3).

The inertial measurements are not used purely as measurements, but rather as an input of the process model to form the reference trajectory against which the measurements of inclination and magnetic field are compared. The position and velocity change over time are extracted from measured inertial acceleration (6.5) and the orientation is estimated from measured angular velocity (6.3). It is the actual measurement minus the predicted measurement that forms the measurement error that is fed into the fusion filter.

We chose to use an Extended Kalman Filter (EKF) that operates on the error states to fuse inertial with magnetic sensing. The error states for the filter are chosen as:

$$\delta \boldsymbol{x} = \begin{pmatrix} \delta \boldsymbol{p} & \delta \boldsymbol{v} & \delta \boldsymbol{\theta} & \delta \boldsymbol{a} & \delta \boldsymbol{\omega} \end{pmatrix}^T, \tag{6.6}$$

where $\delta \boldsymbol{p}$ denotes the position error, $\delta \boldsymbol{v}$ the velocity error, $\delta \boldsymbol{\theta}$ the orientation error, $\delta \boldsymbol{a}$ the accelerometer bias, and $\delta \boldsymbol{\omega}$ the gyroscope bias. In general, the state space equations are given by:

$$\begin{aligned} \delta \dot{\boldsymbol{x}} &= \boldsymbol{f}(\delta \boldsymbol{x}) + \boldsymbol{w}_x & (6.7) \\ \delta \boldsymbol{y} &= \boldsymbol{h}(\hat{\boldsymbol{x}}) - \boldsymbol{y} + \boldsymbol{w}_y, & (6.8) \end{aligned}$$

where $\boldsymbol{f}(\delta \boldsymbol{x})$ denotes the function used to propagate the state vector $\delta \boldsymbol{x}$ in time, $\boldsymbol{y}$ the measurement, and $\boldsymbol{h}(\hat{\boldsymbol{x}})$ the function which maps the estimated state vector $\hat{\boldsymbol{x}}$ to the predicted measurement $\hat{\boldsymbol{y}}$. The additive process and measurement noises are denoted by $\boldsymbol{w}_x$ and $\boldsymbol{w}_y$ with covariances $\boldsymbol{Q}_x$ and $\boldsymbol{Q}_y$, respectively. The measurement model consists of a magnetic update $\delta \boldsymbol{y}_m$ and an inclination update $\delta \boldsymbol{y}_i$. The inclination update is necessary, since an inaccurate estimation of inclination introduces integration drift caused by an incorrect removal of gravitational acceleration.

The recursive algorithm for a Kalman filter consists of a prediction step and an update step. Since the EKF resets the error states to zero immediately after a measurement, only the covariance is updated in the prediction step:

$$\boldsymbol{P}_k^- = \boldsymbol{F}_{k-1} \boldsymbol{P}_{k-1} \boldsymbol{F}_{k-1}^T + \boldsymbol{Q}_{x,k-1}, \tag{6.9}$$

where $\boldsymbol{P}_k^-$ denotes the error covariance associated with the state $\delta \boldsymbol{x}$ at time instant k, and $\boldsymbol{F}_k$ denotes the discrete process model that propagates the state in time. It should be noted that a minus superscript $()^-$ denotes the *a priori* estimate. If a measurement becomes available, the state and covariance are updated resulting in the *a posteriori* estimate:

$$\begin{aligned} \delta \hat{\boldsymbol{x}}_k &= \boldsymbol{K}_k \delta \boldsymbol{y}_k \\ \boldsymbol{P}_k &= (\boldsymbol{I} - \boldsymbol{K}_k \boldsymbol{H}_k) \boldsymbol{P}_k^- \\ \delta \boldsymbol{y}_k &= \hat{\boldsymbol{y}}_k^- - \boldsymbol{y}_k \\ \boldsymbol{K}_k &= \boldsymbol{P}_k^- \boldsymbol{H}_k^T \left(\boldsymbol{H}_k \boldsymbol{P}_k^- \boldsymbol{H}_k^T + \boldsymbol{Q}_{y,k} \right)^{-1}, & (6.10) \end{aligned}$$

with $\boldsymbol{K}_k$ the Kalman gain, $\boldsymbol{H}_k$ the linearized measurement model, and $\boldsymbol{I}$ the identity matrix. Based on an estimation of the uncertainty associated with the position and orientation, represented on the diagonal of the covariance matrix $\boldsymbol{P}_k$, the system decides when a magnetic update is necessary. To decide which coil needs to be actuated, the covariance update (6.10) is calculated for each of the source coils that can be actuated. The system chooses to actuate only that coil with the highest contribution to the reduction of the uncertainty.

In Section 6.2.3, it is shown that the prediction of the state (6.7) can be described by a linear equation using a single matrix ($\boldsymbol{f}(\delta \boldsymbol{x}) = \boldsymbol{F} \delta \boldsymbol{x}$). The nonlinear measurement models for the magnetic update $\boldsymbol{h}_m(\hat{\boldsymbol{x}})$ and the inclination update $\boldsymbol{h}_i(\hat{\boldsymbol{x}})$ as well as their linearized versions are described in Section 6.2.4.

6.2.3 Process Model

The error equations that comprise the process model can be derived by writing the derivative of the state as a function of the state itself, according to (6.7). A complete derivation of the process model is shown in Appendix B. The error state $\delta\boldsymbol{x}$ denotes the difference between the true state $\boldsymbol{x}$ and an estimation of the state $\hat{\boldsymbol{x}}$. For the position error, velocity error, accelerometer bias, and gyroscope bias, the relation is simply given by:

$$\hat{\boldsymbol{x}} = \boldsymbol{x} + \delta\boldsymbol{x}. \tag{6.11}$$

For the orientation error $\delta\boldsymbol{\theta}$, rotation matrices are used:

$$\hat{\boldsymbol{R}}_s^c = \boldsymbol{R}_s^c \delta\boldsymbol{R} \approx \boldsymbol{R}_s^c \left(\boldsymbol{I} + \tilde{\delta\boldsymbol{\theta}}\right) \Rightarrow \tilde{\delta\boldsymbol{\theta}} \approx \left(\boldsymbol{R}_s^c\right)^T \hat{\boldsymbol{R}}_s^c - \boldsymbol{I}. \tag{6.12}$$

The derivative of the orientation error is found by applying (6.12), (6.3), and neglecting the product of errors:

$$\dot{\tilde{\delta\boldsymbol{\theta}}} = \left(\dot{\boldsymbol{R}}_s^c\right)^T \hat{\boldsymbol{R}}_s^c + \left(\boldsymbol{R}_s^c\right)^T \dot{\hat{\boldsymbol{R}}}_s^c \approx \tilde{\delta\boldsymbol{\omega}} - \tilde{\boldsymbol{\omega}}_s^{s,c} \tilde{\delta\boldsymbol{\theta}} + \tilde{\delta\boldsymbol{\theta}} \tilde{\boldsymbol{\omega}}_s^{s,c}. \tag{6.13}$$

The vector representation of the orientation error $\dot{\delta\boldsymbol{\theta}}$ is found by inspecting the individual terms of the skew-symmetric matrix $\dot{\tilde{\delta\boldsymbol{\theta}}}$:

$$\dot{\delta\boldsymbol{\theta}} = \delta\boldsymbol{\omega} - \tilde{\boldsymbol{\omega}}_s^{s,c} \delta\boldsymbol{\theta}. \tag{6.14}$$

The derivative of the velocity error is found by applying (6.5), (6.11), (6.12) and neglecting the product of errors:

$$\dot{\delta\boldsymbol{v}} = \dot{\hat{\boldsymbol{v}}}_s^c - \dot{\boldsymbol{v}}_s^c = \boldsymbol{R}_s^c \delta\boldsymbol{a} - \boldsymbol{R}_s^c \tilde{\boldsymbol{s}}^s \delta\boldsymbol{\theta}, \tag{6.15}$$

and the derivative of the position:

$$\dot{\delta\boldsymbol{p}} = \delta\boldsymbol{v}. \tag{6.16}$$

The accelerometer bias and gyroscope bias are modeled as first order Markov processes:

$$\begin{aligned} \dot{\delta\boldsymbol{a}} &= -\beta_a \delta\boldsymbol{a} + \sqrt{2\sigma_a^2 \beta_a}\boldsymbol{u} \\ \dot{\delta\boldsymbol{\omega}} &= -\beta_\omega \delta\boldsymbol{\omega} + \sqrt{2\sigma_\omega^2 \beta_\omega}\boldsymbol{u}, \end{aligned} \tag{6.17}$$

where $\boldsymbol{u}$ denotes unity white noise. Summarizing, the following state equations have been found:

$$\begin{aligned} \dot{\delta\boldsymbol{p}} &= \delta\boldsymbol{v} \\ \dot{\delta\boldsymbol{v}} &= \boldsymbol{R}_s^c \delta\boldsymbol{a} - \boldsymbol{R}_s^c \tilde{\boldsymbol{s}}^s \delta\boldsymbol{\theta} \\ \dot{\delta\boldsymbol{\theta}} &= \delta\boldsymbol{\omega} - \tilde{\boldsymbol{\omega}}_s^{s,c} \delta\boldsymbol{\theta} \\ \dot{\delta\boldsymbol{a}} &= -\beta_a \delta\boldsymbol{a} \\ \dot{\delta\boldsymbol{\omega}} &= -\beta_\omega \delta\boldsymbol{\omega}. \end{aligned} \tag{6.18}$$

6.2.4 Measurement Model

This section describes the measurement models that are used to update the estimation of the state. First, the model for the magnetic update $\boldsymbol{h}_m(\hat{\boldsymbol{x}})$ and its linearized version $\boldsymbol{H}_m$ are described, followed by the model for the inclination update $\boldsymbol{h}_i(\hat{\boldsymbol{x}})$ and its linearized version $\boldsymbol{H}_i$.

Magnetic Update

The magnetic measurement model is used to predict the field generated by the source coil at the location of the sensor based on an estimation of the position and orientation of the sensor. Figure 6.2 shows a configuration with a coil around the z axis, which means frames Ψ_{cz} and Ψ_c are aligned. The position of both frames with respect to each other is denoted by $\boldsymbol{p}_{cz}^c$. Applying the measurement model proposed in Chapter 5 to the configuration shown in Figure 6.2 results in:

$$\hat{\boldsymbol{y}}_m = \boldsymbol{h}_m(\hat{\boldsymbol{x}}) = \hat{\boldsymbol{B}}^s = \left(\hat{\boldsymbol{R}}_s^{cz}\right)^T \hat{\boldsymbol{B}}^{cz}, \tag{6.19}$$

where $\hat{\boldsymbol{B}}^s$ denotes the magnetic field measured by the sensor, and $\hat{\boldsymbol{R}}_s^{cz} = \left(\boldsymbol{R}_{cz}^c\right)^T \hat{\boldsymbol{R}}_s^c$ denotes the relative orientation of the sensor with respect to the coil. The magnetic field that is generated by the source coil at the location of the sensor expressed in coil coordinates is given by (Appendix A.1):

$$\hat{\boldsymbol{B}}^{cz}(\hat{\boldsymbol{p}}_s^{cz}) = \frac{\mu_0 N I}{2\pi\sqrt{(\sqrt{\hat{p}_x^2+\hat{p}_y^2}+b)^2+\hat{p}_z^2}} \begin{pmatrix} \frac{\hat{p}_x\hat{p}_z}{\hat{p}_x^2+\hat{p}_y^2}\left(-K(k)+\frac{b^2+\hat{p}_x^2+\hat{p}_y^2+\hat{p}_z^2}{(\sqrt{\hat{p}_x^2+\hat{p}_y^2}-b)^2+\hat{p}_z^2}E(k)\right) \\ \frac{\hat{p}_y\hat{p}_z}{\hat{p}_x^2+\hat{p}_y^2}\left(-K(k)+\frac{b^2+\hat{p}_x^2+\hat{p}_y^2+\hat{p}_z^2}{(\sqrt{\hat{p}_x^2+\hat{p}_y^2}-b)^2+\hat{p}_z^2}E(k)\right) \\ K(k)+\frac{b^2-\hat{p}_x^2-\hat{p}_y^2-\hat{p}_z^2}{(\sqrt{\hat{p}_x^2+\hat{p}_y^2}-b)^2+\hat{p}_z^2}E(k) \end{pmatrix}, \tag{6.20}$$

with μ_0 the magnetic permeability of vacuum ($4\pi \cdot 10^{-7}$ T $\cdot$ m^2/A), N the number of windings, I the current applied, and b the radius of the coil. It should be noted that the indices $()_s^{cz}$ have been omitted for readability. The relative position of the sensor with respect to the coil is given by $\hat{\boldsymbol{p}}_s^{cz} = \left(\boldsymbol{R}_{cz}^c\right)^T(\hat{\boldsymbol{p}}_s^c - \boldsymbol{p}_{cz}^c)$, and

$$\begin{aligned} k &= \sqrt{\frac{4b\sqrt{\hat{p}_x^2+\hat{p}_y^2}}{(\sqrt{\hat{p}_x^2+\hat{p}_y^2}+b)^2+\hat{p}_z^2}} \\ K(k) &= \int_0^{\pi/2} \frac{1}{\sqrt{1-k^2\sin^2\phi}}d\phi \\ E(k) &= \int_0^{\pi/2} \sqrt{1-k^2\sin^2\phi}\,d\phi. \end{aligned} \tag{6.21}$$

The linearized model is given by:

$$\boldsymbol{H}_m = \frac{\partial\hat{\boldsymbol{y}}_m}{\partial\delta\boldsymbol{x}} = \begin{pmatrix}\left(\hat{\boldsymbol{R}}_s^{cz}\right)^T \frac{\partial\hat{\boldsymbol{B}}^{cz}}{\partial\delta\boldsymbol{p}} & \boldsymbol{0} & \tilde{\hat{\boldsymbol{B}}}^s & \boldsymbol{0} & \boldsymbol{0}\end{pmatrix}. \tag{6.22}$$

The partial derivatives of the estimated field with respect to the position error $\left(\left(\hat{\boldsymbol{R}}_s^{cz}\right)^T \frac{\partial\hat{\boldsymbol{B}}^{cz}}{\partial\delta\boldsymbol{p}}\right)$ result in a rather lengthy and complicated expressions, which are shown in Appendix A.2.

Inclination Update

The inclination can be updated only during periods of low acceleration. Therefore, the measured acceleration is tested in advance for deviations from the gravitational acceleration. In case of significant deviations, the measurement noise is set to extremely high values such that the

acceleration is not used to update the inclination during these intervals. The measurement equation for the inclination update is given by:

$$\hat{\boldsymbol{y}}_i^s = \boldsymbol{h}_i\left(\hat{\boldsymbol{x}}\right) = \left(\hat{\boldsymbol{R}}_s^g\right)^T \boldsymbol{g}^g + \delta\boldsymbol{a} = \left(\hat{\boldsymbol{R}}_s^c\right)^T \left(\hat{\boldsymbol{R}}_c^g\right)^T \boldsymbol{g}^g + \delta\boldsymbol{a}, \tag{6.23}$$

where $\boldsymbol{g}^g$ denotes the gravitational acceleration in global coordinates.

The linearized model is given by:

$$\boldsymbol{H}_i = \frac{\partial \hat{\boldsymbol{y}}_i^s}{\partial \delta \boldsymbol{x}} = \begin{pmatrix} \boldsymbol{0} & \boldsymbol{0} & \tilde{\hat{\boldsymbol{g}}}^s & \boldsymbol{I} & \boldsymbol{0} \end{pmatrix}, \tag{6.24}$$

with $\hat{\boldsymbol{g}}^s$ being the estimated inclination in sensor coordinates.

6.2.5 Experimental Methods

The measurement system, as shown in Figure 6.1, consisted of two IMMS modules (MTx with Xbus, Xsens Technologies B.V.), and three coils mounted orthogonal with respect to each other. Each coil was a circular coil with 50 windings and a radius of 0.055 m. The IMMS modules were sampled at 100 Hz. The maximum current that could be delivered by the driving electronics was 1.5 A. The driving electronics were controlled realtime by sending messages to the Xbus via a wireless Bluetooth connection. At certain time instants, the magnetic system generates magnetic pulses that were measured by the magnetometer of the IMMS. For each pulse, the mean and standard deviation were calculated which were both fed into the EKF. For validation, the relative position and orientation estimated by the fusion filter were compared to a reference optical position measurement system (Vicon, Oxford Metrics). Three markers with a diameter of 25 mm were attached to each IMMS. The reference data was obtained at a sample frequency of 100 Hz.

During the experiments, the system decided realtime when an actuation was required and which of the three coils should be actuated based on an estimation of the uncertainty associated with the position and orientation. The actuation current (1.3 A) and pulse duration (30 ms) were fixed. The complete experiment consisted of three parts. In the first experiment, the three source coils with IMMS were placed on a flat surface. An IMMS was moved around the source while varying the position and orientation. In the second experiment, the three source coils with IMMS were attached to the lower back of a subject, and the subject performed several movements with respect to the standing posture. With an IMMS attached to the back at the level of the first thoracic vertebra, the subject performed flexion/extension and rotation of the back. With an IMMS attached to the upper leg, the subject performed hip flexion/extension, and with an IMMS attached to the upper arm, the subject performed shoulder abduction/adduction. In the third experiment, the subject walked through the laboratory at a self selected speed. The IMMS was attached to the upper leg and to the back at the level of the first thoracic vertebra.

6.3 Results

Figure 6.4 shows the relative position of the sensor with respect to the source for a representative trial of the first experiment, where the sensor was moved around the source coils which were not moving. The position error is defined as the difference between the estimated relative position by the ambulatory system and the reference system. Similarly, the orientation error is defined as

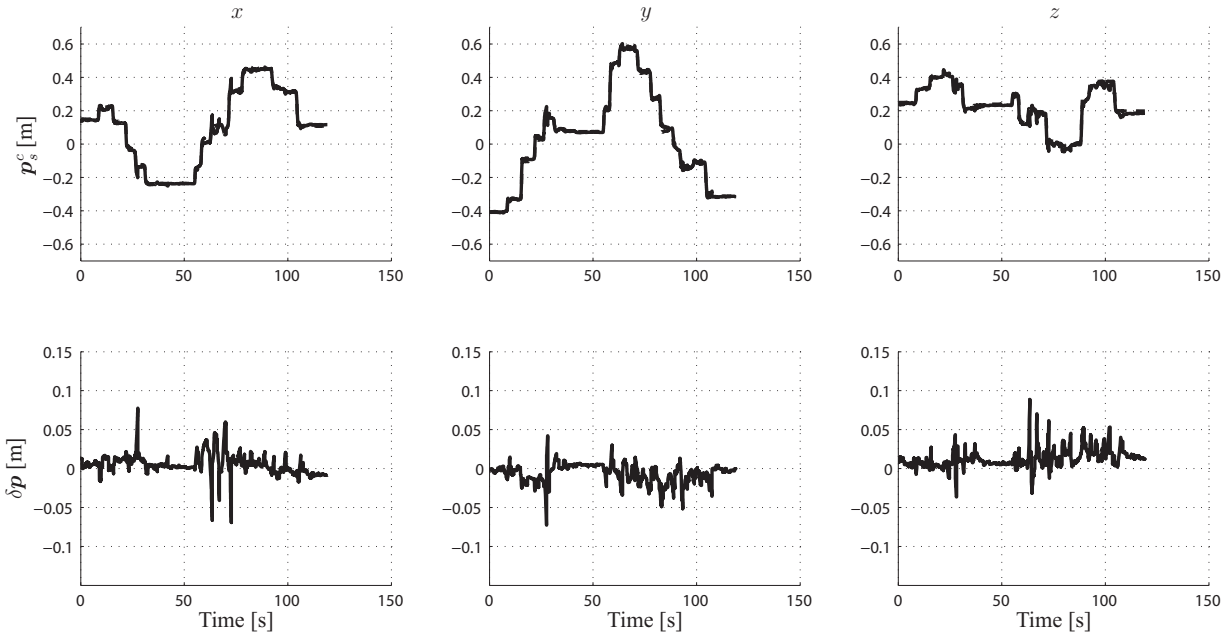

Figure 6.4: *Relative position of the sensor with respect to the source for a representative trial of experiment 1. Top figures: x, y and z coordinates estimated by the fusion filter (solid) and reference system (dashed). Bottom figures: Position error.*

the smallest angle about which the relative orientation of the sensor with respect to the source estimated by the ambulatory system has to be rotated to coincide with the relative orientation estimated by the reference system. The rms errors, averaged over 10 trials were calculated to be 0.028 ± 0.004 m (mean $\pm$ standard deviation) for the position and 3.1 ± 0.6 degrees for the orientation. A major part of the position error can be attributed to the peaks shown in the bottom figures of Figure 6.4, which are caused by the experimental setup. During the peaks, a certain amount of data was queued in the input buffer causing the filter propagate slightly delayed data. If the filter then decides to perform a magnetic update, the input buffer must be emptied before the filter can process the response to the magnetic update causing the error to increase. The position error can be decreased by using the updated position after a magnetic actuation to reduce the drift between updates [70]. This resulted in a remaining rms position error of 0.022 ± 0.004 m averaged over 10 trials.

As mentioned, the system decides realtime if it is required to actuate based on an estimate of the uncertainty associated with the relative position and orientation. Moreover, the system chooses which coil should be updated such that maximum information is obtained. An overview of the choices made by the filter for a trial where the IMMS was moved around the source are shown in Figure 6.5. Each dot represents a magnetic update and the coil that has been actuated is depicted by the value on the vertical axis. The right figure indicates that the choice of the coil to be actuated is indeed dependent on the location of the sensor.

During time intervals when the relative position and orientation of the sensor with respect to the source do not change, the time intervals between updates should increase. This is shown in Figure 6.6, which shows the relative distance between source and sensor and the time instances of the magnetic updates. As can be seen, the time intervals between magnetic updates increase when the sensor is not moving, and decrease during movements. The bottom line indicates the uncertainty associated with the x position error $\sigma_{\delta p_x}$, which remains bounded due to the magnetic updates.

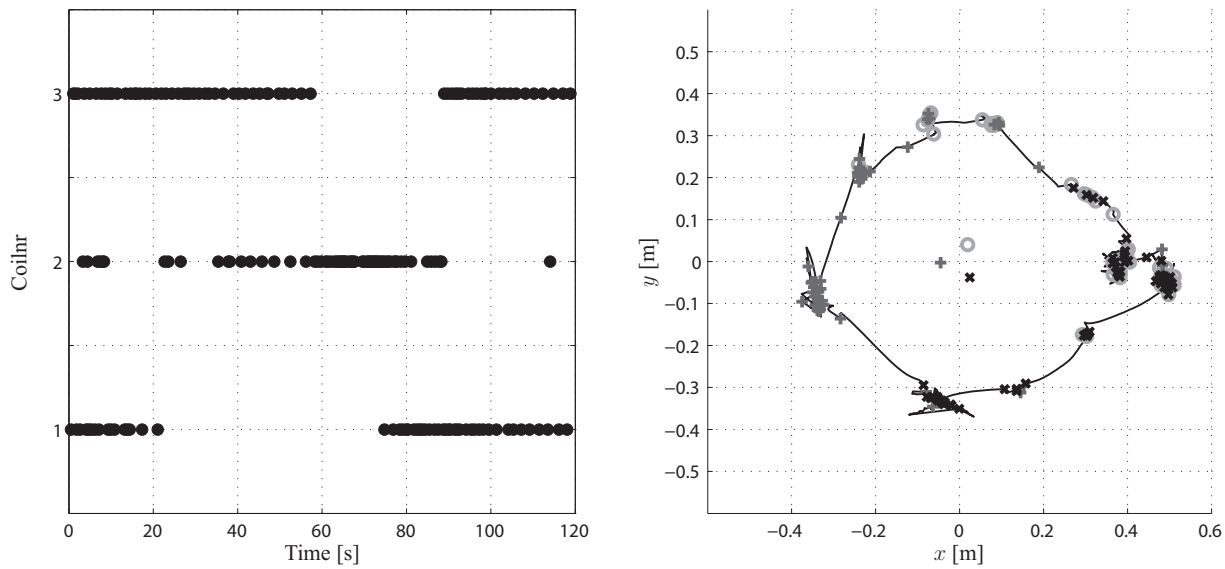

Figure 6.5: *The left figure shows the time instances and coil number of the coil that has been actuated. The right figure shows a top view of the relative position of the sensor with respect to the source. Each point indicates the position after a magnetic update (x: circle; y: plus sign; z: cross). The origins of the source coils are indicated in the center of the figure (x: circle; y: plus sign; z: cross).*

An example of the relative position of the sensor with respect to the source for a shoulder abduction/adduction trial with an IMMS attached to the upper arm is shown in Figure 6.7. The solid line indicates the estimation by the fusion filter, the dashed line indicates the estimation by the reference system. The rms position error was 0.025 ± 0.012 m, the rms orientation error was 2.8 ± 0.7 degrees averaged over 5 trials.

The bottom figure of Figure 6.8 shows the relative position of the sensor with respect to the

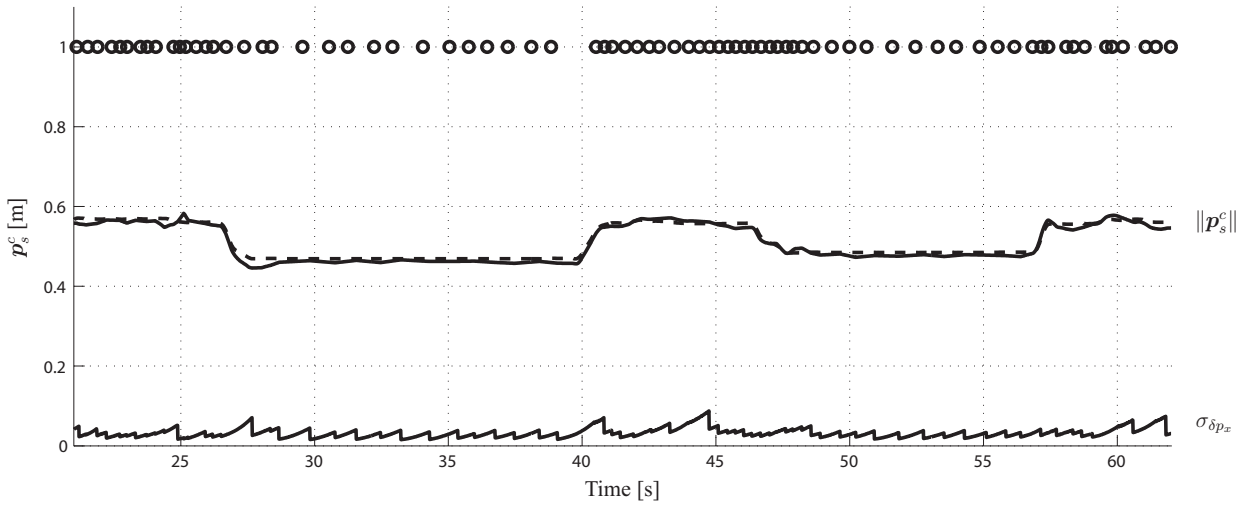

Figure 6.6: *Decreasing update rate when the sensor is not moving. The relative distance between sensor and source is indicated by the solid line for the fusion filter and the dashed line for the reference system. The time instances of the magnetic updates are indicated by the dots. The bottom line indicates the uncertainty associated with the x position error $\sigma_{\delta p_x}$.*

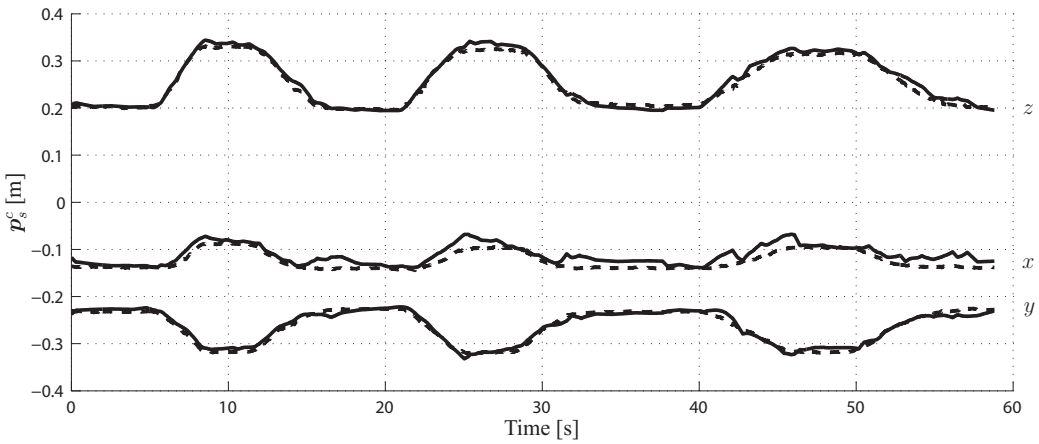

Figure 6.7: *Relative position of the sensor with respect to the source for shoulder abduction/adduction with an IMMS attached to the upper arm, estimated by the fusion filter (solid) and reference system (dashed).*

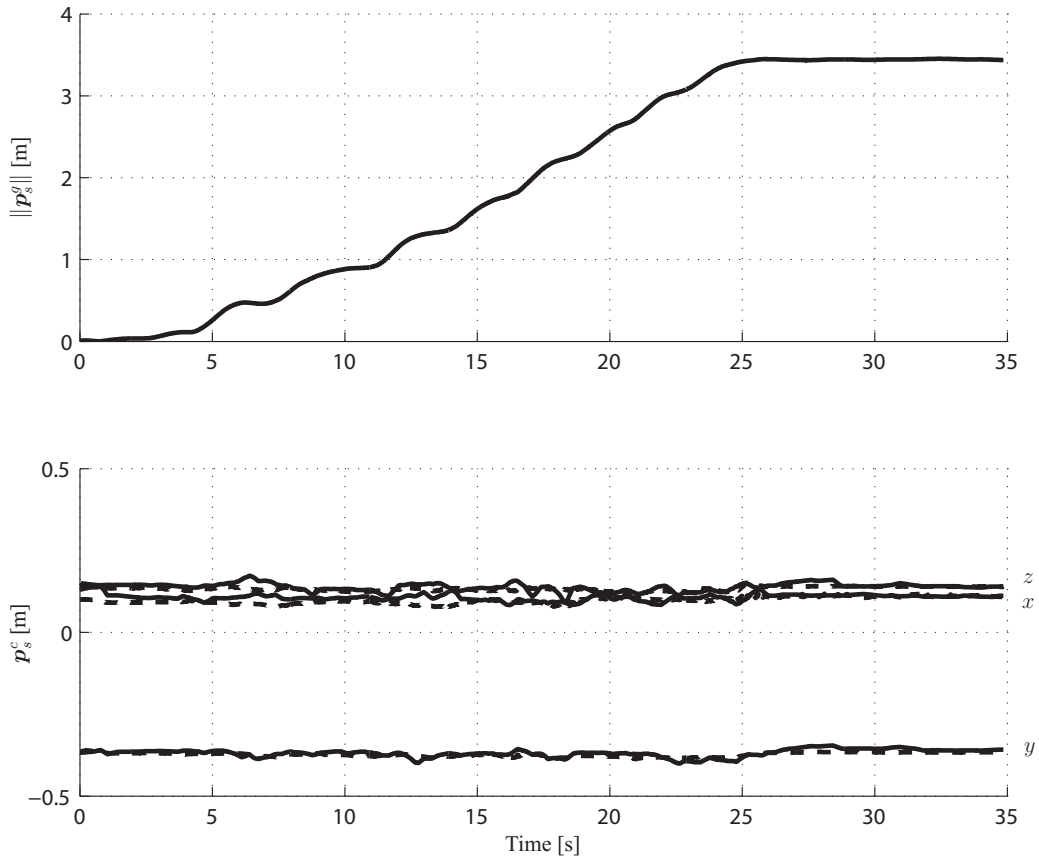

Figure 6.8: *Representative trial of a subject during walking with the source attached to the lower back and an IMMS at the level of the first thoracic vertebra. Top figure: distance traveled by the subject estimated by the reference system. Bottom figure: relative position of the sensor with respect to the source estimated by the fusion filter (solid) and reference system (dashed).*

Table 6.1: *Mean and standard deviation (std) of rms position and orientation error for all movements that were performed during the experiments. The number of trials for each movement is indicated by n.*

Exp nr	IMMS location	Movement	rms pos. error [m]		rms ori. error [deg]		n
			mean	std	mean	std	
1	Around source	Random	0.022	0.004	3.1	0.6	10
2	Spine (T1)	Flexion	0.035	0.003	4.5	0.7	5
	Spine (T1)	Rotation	0.028	0.006	4.3	0.3	5
	Upper Leg	Hip flexion	0.062	0.011	3.6	0.9	5
	Upper Arm	Shoulder abd.	0.025	0.012	2.8	0.7	5
3	Spine (T1)	Walking	0.026	0.004	3.6	0.4	6
	Upper Leg	Walking	0.047	0.010	3.6	1.0	5

source for a representative walking trial with the IMMS attached to the back at the level of the first thoracic vertebra. Despite the movement of source and sensor as indicated by the top figure of Figure 6.8, the filter is able to provide a stable estimate of the relative position and orientation. The rms errors, averaged over 6 trials, were calculated to be 0.026 ± 0.004 m for the position and 3.6 ± 0.4 degrees for the orientation. A complete overview of the position and orientation errors for all experiments that were performed is shown in Table 6.1.

6.4 Discussion

The adaptive filter proposed in the present study allows accurate ambulatory tracking of relative positions and orientations on the human body. The change of position and orientation is estimated using inertial sensing. A fusion filter (EKF) estimates the uncertainty associated with the position and orientation and a magnetic coil is actuated only if the uncertainty associated with the position or orientation exceeds a predefined threshold. Moreover, the coil delivering most information is actuated only. The actuation current and pulse duration were fixed during the experiments. In future experiments, these parameters can also be tuned adaptively such that maximal accuracy is achieved at minimal energy consumption.

The results indicate that the filter is able to provide a stable estimate of relative position and orientation for several types of movements. Although a previous study [35] showed higher accuracy for the relative position (position error approximately 5 times smaller), and comparable accuracy for the relative orientation, significant improvements were achieved for the update rate (average time between magnetic actuation of 547 ms using single coil actuation instead of 600 ms using three coils actuation), and pulse width (30 ms instead of 60 ms). Moreover, the orientation of source and sensor reported in [35] were obtained from a separate Kalman Filter, whereas this study estimates the orientation of source and sensor in a single filter running realtime. In order to achieve higher accuracy, it is suggested to improve the experimental setup such that the cause of the error peaks reported in Section 6.3 is removed. An improved setup should also allow multiple coils to be actuated simultaneously during rapid movement periods, which is not possible using the current setup. Another suggestion to improve the accuracy is to apply a Kalman smoothing algorithm in an off-line analysis that propagates the filter backward in time [109].

The presence of nearby ferromagnetic materials can influence the accuracy of the filter negatively. In Chapter 5, it was shown that a ferromagnetic material influences the measurements only if it was located near the sensor or between the source and sensor. It is therefore important to remove any ferromagnetic objects from the body during the measurements. During periods of no actuation, the magnetometers can be used to detect ferromagnetic disturbances. In an undisturbed environment, the magnetometer will measure a homogeneous earth magnetic field. In case of a nearby ferromagnetic object, the magnetometer can be used to detect the inhomogenity of the magnetic field caused by the ferromagnetic object. By increasing the measurement noise of the magnetic update during these periods, the filter relies less on the disturbed measurement.

Despite the promising results, several aspects of the proposed system can be improved. An improvement could be to reuse the energy of the magnetic field for future actuation. The hardware used for the experiments is designed such that it dissipates all energy needed to build up the magnetic field. During the pull down phase of the current pulse, the change of magnetic field can be used to induce a current in another source coil. The electrical energy can be stored and used to build up the field for the next actuation.

Another improvement would be to use an adaptive instead of a fixed threshold to decide if the magnetic system should actuate, by taking sensor location into account. If the sensor is located near the source, a relatively small amount of energy is required for an update. If the sensor is located far from the source, much energy is required for an update while the reduction of the uncertainty will be small since the signal to noise ratio will be low. This means that by adapting the uncertainty threshold and actuation parameters based on the relative distance between source and sensor such that the system increases the update rate for sensor locations near the source, the overall energy consumption can be decreased.

It should be noted that other effective solutions exist to obtain an estimate of relative orientation of sensors with respect to each other. Accelerometers provide an estimate of inclination during periods of low acceleration (Section 6.2.4). Similarly, magnetometers provide an estimate of heading using the earth magnetic field [28, 16, 17]. The heading accuracy depends on the amount of earth magnetic field disturbance [105]. Moreover, the earth magnetic field does hardly provide heading information if the direction of the magnetic field is close to the vertical, which may occur in a disturbed environment. A major advantage of the system proposed is that it does not need the earth magnetic field for an accurate estimation of relative position and orientation.

In the first part of this thesis, we proposed an instrumented shoe that can be used to assess ankle and foot dynamics (Chapter 2), foot placement during walking (Chapter 3), and center of mass movement during walking (Chapter 4) in an ambulatory environment. An important aspect missing in the instrumented shoe principle is the estimation of relative positions, for example the distance between the feet or the distance between the center of mass and the feet. Although these distances can not be covered using the setup used in the present study, the coil dimensions can be optimized to be suitable. Concluding, the ambulatory tracking system is expected to provide a valuable contribution to human movement analysis, as it allows relative positions and orientations to be estimated using a wearable system.

7

General Discussion

7.1 Introduction

This thesis had two objectives to overcome some essential limitations of existing systems for ambulatory assessment of human body kinematics and kinetics. Chapters 2 to 4 dealt with the first objective, which was to develop and evaluate a method that can be used to assess the 3D GRF, the CoP trajectory, the CoM trajectory, and the movement of the foot using an instrumented shoe. In Chapter 2, the instrumented shoe was introduced, and used to assess ankle and foot dynamics and the movement of foot and ankle during walking. The GRF and ankle moment, estimated from two 6D force/moment sensors and two inertial sensors attached to the shoe, showed good correspondence with the GRF measured by a force plate. The reproduction of the ankle power showed larger differences, which were caused by an inaccurate estimation of the angular velocity by the reference system due to the use of a single segment foot model. The instrumented shoe was used in Chapter 3 to assess lateral foot placement and stride length during human walking. A comparison with a reference optical position measurement system revealed that lateral foot placement and stride length can be accurately estimated using the instrumented shoe. Additionally, the ambulatory system was able to discriminate between different walking conditions, like the reference system. Chapter 4 proposed a method to assess the CoM displacement continuously during walking using the instrumented shoe. The displacement of the CoM was estimated by fusing low-pass filtered CoP data with high-pass filtered double integrated CoM acceleration. The CoM estimation using the ambulatory measurement system was compared to CoM estimation using an optical reference system, based on the segmental kinematics method. The results indicated that the instrumented shoe concept allows continuous estimation of CoM displacement under ambulatory conditions.

The second objective was to develop and evaluate a method that can be used to estimate relative positions and orientations on the human body by fusion of inertial and magnetic sensing using a tightly coupled filter structure. The method should not be dependent on a specific coil configuration and should allow the instants of actuation to be chosen adaptively based on the uncertainty of the estimated position and orientation. Furthermore, the number of actuations and the actuation parameters should be chosen such that the system achieves maximal accuracy at minimal energy consumption. A stochastic magnetic measurement model that can be used to predict the magnetic field generated by the source coil at the location of the sensor based on an estimation of the relative position and orientation of the sensor with respect to the source was described in Chapter 5. The measurement model was used in a realtime Extended Kalman Filter (EKF) with a tightly coupled structure in Chapter 6. Inertial sensors were used to predict the change of position and orientation between magnetic updates. An estimation of the uncertainty associated with the relative position and orientation by the EKF was used to decide if a magnetic update was needed. In case of an actuation, the system chose to actuate only that coil delivering most information for the reduction of the uncertainty. Two sources of error were defined that could lead to divergence of the fusion filter, being the use of a linearized version of the nonlinear measurement model to update the estimate of position and orientation, and the appearance of ferromagnetic objects in the vicinity of source or sensor. It appeared that the linearized model introduced errors which generally increased for sensor locations near the source, and that a ferromagnetic object influenced the measurements only if it was located near or between the source and sensor. It was shown that the filter should update regularly, to prevent inconsistent behaviour of the fusion filter.

The remainder of this chapter discusses some aspects related to the objectives of this thesis. The final section proposes some recommendations for future research.

7.2 Force and Movement Sensing Using an Instrumented Shoe

The instrumented shoe was used to assess several important gait variables during walking, such as the GRF, CoM movement, CoP movement, and joint moments. Although the instrumented shoe was able to estimate these variables accurately, the design of the shoe could raise questions about its influence on the walking pattern. The force transducers were mounted between aluminum plates that were used to attach the sensors to the shoe. Moreover, two inertial sensors were rigidly connected to the force transducers by aluminum frames. The aluminum objects were not strictly necessary for proper functioning of the shoe. Moreover, the inertial sensor was a commercial sensor with much more functionality such as a magnetometer and a digital processing unit for signal processing, which were not used for the analysis with the instrumented shoe. This means the height and weight can be significantly reduced by mounting the accelerometers and gyroscopes together with the force transducers beneath the shoe. Possibly, the commercial force transducers can be replaced by smaller custom made transducers. Still, the purpose was not to present an optimal design of the shoe, but to present methods to extract important gait variables. In principle, an improvement to the design will not affect the functionality of the presented methods. It should be noted that the influence of the shoe on the walking pattern appeared to be small, which was reported by several users wearing the shoes, and shown in an evaluation study of Liedtke *et al.* [61]. In that study, several gait parameters were estimated for a group of healthy subjects wearing the instrumented shoes, light, normal and heavy weight shoes. Only the maximum GRF revealed significant differences between the shoe types, but these could not be attributed to individual shoe types. Additionally, the differences were considered irrelevant, since they were small compared to the body weight of the subjects.

The current version of the algorithm is not able to provide a stable estimate of the position of both feet with respect to each other for a long period of time, and requires an independent initial estimation of this relative distance. Yet, for an accurate estimation of the CoM and its relation to the CoP, this is essential. The trials for the experiments described in this thesis were relatively short (less than one minute), which limits the drift. However, information about the distance between the feet can be obtained during walking using other sources of information, for example by applying Newton's second law applied for rotational motion. Using the GRFs as measured by the instrumented shoe, and applying the assumption that the product of angular acceleration and moment of inertia will be small during walking, allows the lateral distance between both feet to be estimated (Chapter 4). Also, a biomechanical model applying joint constraints [110], or a fusion filter using adaptive actuation as described in Chapter 6 may be used. This also holds if it is desired to relate the lateral foot placement and stride length (Chapter 3) of both feet with respect to each other. Nevertheless, for most biomechanical applications the presented methods will suffice, as most information can be obtained by relating the current stride to a small number of consecutive strides.

7.3 Relative Position and Orientation Estimation

The fusion filter presented in Chapter 6 was designed to estimate relative position and orientation of a remote sensor with respect to the source. In the state vector, only the biases of the gyroscope and accelerometer of the remote sensor were included. For a future design of the filter, it

is advisable to include the biases of the inertial sensor attached to the source as well. Also, the inclination update was applied to the remote sensor only. An improvement would be to either include an inclination update for the inertial sensor attached to the source, or a more advanced Kalman Filter for the estimation of orientation [28] running parallel to EKF described in Chapter 6.

The theory presented in Chapter 5 and Chapter 6 was validated using a specific experimental setup that consisted of three identical source coils in an orthogonal arrangement. However, the theory can be applied for any configuration and coil shape as long as the orientation of the coil, and the mapping function used to predict the magnetic field are known, either analytically or numerically. This opens possibilities to integrate the coils in garments such that they do not impede normal functioning. Also, the current configuration is designed to have a central source with several remote sensors. An alternative would be to attach source coils to several segments which can also introduce redundancy.

We chose to use magnetic sensing as an aiding system to complement inertial sensing. For most biomechanical application, this will probably be the best option since the human body is transparent for the field applied. Also, the accuracy is high enough to estimate the relative position and orientation of segments with respect to each other. The accuracy can be improved by combining the system with a biomechanical model of the human body and applying the joint constraints [110]. If it is desired to estimate the position and orientation of a person with respect to its environment, several alternatives may be considered. A suitable alternative for indoor applications that has recently risen considerable interest is Ultra-Wide Band (UWB) positioning [32]. For outdoor applications, GPS might be a suitable alternative [29]. If the purpose is to estimate only the orientation with respect to the global frame, an inertial and magnetic measurement unit will suffice [15, 16, 17, 20].

The experimental setup that was used to evaluate the accuracy of the fusion filter (Chapter 6) was designed to generate direct current (DC) excitations only. An alternative would be to use alternating current (AC) excitation. The major advantage of DC excitation is that it is less susceptible to disturbances caused by secondary magnetic fields generated by eddy currents induced in conducting objects in the environment of the configuration, although it is important to wait for the initial transient to decay. However, as stated in Chapter 5, the magnetic measurements are influenced only if a disturbing object is located near or between the source or sensor, making the system insensitive to most disturbing objects in the environment. Removal of any ferromagnetic objects in the vicinity of source and sensor eliminates distortions due to eddy currents, and enables the use of AC excitation. The major advantages of AC excitation is that multiple coils can be actuated simultaneously by applying specific band filters. Such a specific band filter will also reduce the measurement noise, which will result in a better signal to noise ratio.

In Chapter 6, a tightly coupled EKF was used that operates on the error states. It appeared in Chapter 5 that the use of a linearized version of the nonlinear model introduced errors that are related to the second order spatial derivatives of the magnetic field. An EKF only propagates the sample mean through the nonlinearity, whereas the covariance is propagated using first order linearizations. In order to include higher order terms in the equations of the filter, alternative filter solutions may be considered. Possible alternatives are the Unscented Kalman Filter (UKF) [111], or the Particle Filter (PF) [112]. The UKF uses a deterministic sampling technique known as the unscented transform to pick a minimal set of so-called sigma points around the mean. These sigma points are propagated through the nonlinear functions, and the covariance of the estimate is recovered. The result is a filter which more accurately

captures the true mean and covariance. In addition, this technique removes the requirement to explicitly calculate the Jacobians, which was required for the EKF. The PF represents the probability density functions by a set of randomly chosen weighted samples. In contrast to the EKF, which applies an optimal filter to an approximate model, the PF approximates the optimal solution numerically based on the underlying physical model. It should be noted that, if the assumptions for the Kalman Filter are valid, no PF can outperform it. Additionally, compared to the EKF, the UKF and the PF may require much more computational time due to sampling of the probability density function.

The second objective states that the magnetic system should achieve maximal accuracy at minimal energy consumption. Although this was not completely fulfilled in this thesis, the methods that were presented do allow this aspect to be implemented. The fusion filter was able to decide realtime if an actuation was needed and which coil should be actuated in order to achieve the largest reduction of the uncertainty. The actuation current, pulse width and the threshold that was used to decide if an actuation was necessary were fixed, but can be made adaptive by including the relative position and orientation in the update criterion. Also, inactive coils can be used to store the energy of the magnetic field when the actuation of a coil has finished, which can then be used for a subsequent actuation.

7.4 Recommendations for Future Research

Chapter 2 was about ambulatory assessment of ankle and foot dynamics. Several applications require the dynamics of other joints in the human body to be estimated. To do so, the GRF and CoP estimated by the instrumented shoes can be used, but an accurate estimation of the position of the joints is required as well. This can be achieved by using estimated orientations in a kinematic chain model of the human body, or by applying the fusion filter described in Chapter 6.

Apart from estimation of interaction forces between the human body and the ground as was described in the first part of this thesis using instrumented shoes, it would be interesting to assess other interactions of the human body with the environment. An example is the assessment of power transfer between the human body and the environment at any time, and the work performed, which are important quantities when evaluating and optimizing the physical interaction in sports, physical labor and rehabilitation [113]. The power is calculated by summing the inner product of force and velocity, and of moment and angular velocity. The majority of the methods presented in Chapter 2 can be used to achieve this. However, if the power transfer needs to be assessed in a daily life environment, it is essential that the sensors for force and movement sensing are miniaturized. Also, force and movement have to be measured in the same coordinate frame. Besides the assessment of power transfer between the human body and its environment, the measured quantities can also be used to provide information about the dynamic characteristics of the load and the human body [113]. These aspect are currently being investigated in the ‘PowerSensor’ project financed by the Dutch Technical Sciences Foundation (STW).

Although the measurement systems presented in this thesis were ambulatory in the sense that the data was transmitted to a PC through a wireless connection, the individual sensors were connected via cables on the body. Recent improvements in small and compact power supplies such as fuel cells, allow the connections between sensors to become wireless. The removal of cable connections is also advantageous if the measurement systems are going to be used during

daily life activities.

The assessment of the GRF beneath the sole of the shoe is complementary to the assessment of the pressure distribution inside the shoe using pressure measuring insoles. The combination of 3D force sensing beneath the shoe and pressure sensing inside the shoe can be used to assess the individual force components under specific areas of the foot inside the shoe, which is interesting for the diagnosis and treatment of pathological foot disorders for example. By comparison of the vertical GRF under the shoe with the pressure at specific locations inside the shoe and assuming that the horizontal force components will scale similarly [114], allows the local distribution of loads under the foot inside the shoe to be estimated. The systems can be aligned by the CoP that is estimated by both measurement systems. The resulting system will be redundant for some quantities, which means it can also be used for calibration.

Concluding, the methods that were presented in this thesis are expected to provide a valuable contribution to the ambulatory assessment of several important variables for biomechanical analysis. Especially, the combination of the instrumented shoe concept with relative position and orientation tracking will allow accurate assessment of human body kinematics and kinetics for extended periods of time without impeding natural movements.

A

Derivation of the Stochastic Magnetic Model

A.1 Magnetic Flux Density

This section describes the derivation of the expression for the magnetic flux density $\boldsymbol{B}$ at the location of the sensor generated by the source coil. In general, the magnetic flux density $\boldsymbol{B}$ is calculated by the curl of the magnetic potential $\boldsymbol{A}$:

$$\boldsymbol{B} = \boldsymbol{\nabla} \times \boldsymbol{A}. \tag{A.1}$$

The magnetic potential $\boldsymbol{A}$ of a current-carrying thin wire circuit is found by [101]:

$$\boldsymbol{A} = \frac{\mu_0 I}{4\pi} \oint_{C'} \frac{d\ell'}{R'}, \tag{A.2}$$

with μ_0 being the magnetic permeability of vacuum ($4\pi \cdot 10^{-7}$ T $\cdot$ m^2/A). Since the magnetic field is axial symmetric, we will derive the expressions using cylindrical coordinates. Figure A.1 shows a circular loop of wire with radius b that carries a current I. For every $Id\ell'$ there is another symmetrically located differential current element on the other side of the x-axis that will contribute to an equal amount to $\boldsymbol{A}$ in the negative y direction, but will cancel the contribution of $Id\ell'$ in the positive x direction. The magnetic potential $\boldsymbol{A}$ can be written as:

$$\boldsymbol{A} = \begin{pmatrix} A_r \\ A_\phi \\ A_z \end{pmatrix} = \begin{pmatrix} 0 \\ A_\phi \\ 0 \end{pmatrix}. \tag{A.3}$$

The distance R' can be expressed as:

$$R' = \sqrt{r^2 + b^2 + z^2 - 2br\sin\phi'}, \tag{A.4}$$

which means A_ϕ is given by:

$$A_\phi = \frac{\mu_0 I}{2\pi} \int_{-\pi/2}^{\pi/2} \frac{b\sin\phi'}{\sqrt{r^2 + b^2 + z^2 - 2br\sin\phi'}} d\phi'. \tag{A.5}$$

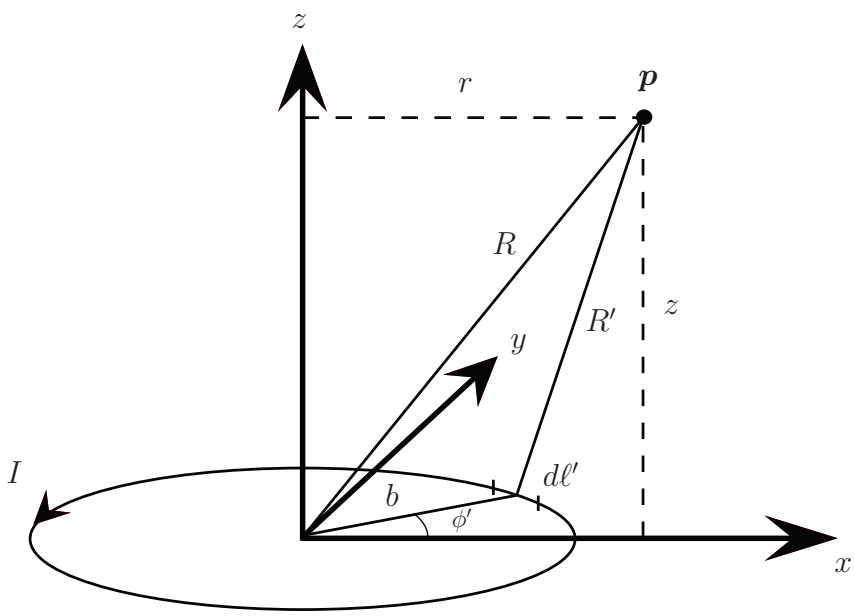

Figure A.1: *Circular wire loop of radius b carrying a current I.*

If the point of interest satisfies $R = \sqrt{r^2 + z^2} \gg b$, (A.5) can be simplified, resulting in the dipole approximation of the magnetic flux density, which is shown in Section A.1.2. The next section describes the analytical derivation of the magnetic flux density.

A.1.1 Analytical Derivation

This section derives the magnetic flux density at a remote location $\boldsymbol{p}$ generated by the circular coil shown in Figure A.1. The integral of (A.5) is solved using elliptic integrals which are given by:

$$\begin{aligned} E(k) &= \int_0^{\pi/2} \sqrt{1 - k^2 \sin^2\theta} d\theta \\ K(k) &= \int_0^{\pi/2} \frac{1}{\sqrt{1 - k^2 \sin^2\theta}} d\theta \\ k &= \sqrt{\frac{4br}{(r+b)^2 + z^2}}, \end{aligned} \tag{A.6}$$

where $\phi' = \frac{3}{2}\pi + 2\theta$, which means $d\phi' = 2d\theta$, and $\sin\phi' = \sin\left(\frac{3}{2}\pi + 2\theta\right) = -\cos 2\theta = 2\sin^2\theta - 1$, which means:

$$\begin{aligned} A_\phi &= \frac{\mu_0 I}{2\pi} \int_{-\pi/2}^{\pi/2} \frac{b \sin\phi'}{\sqrt{r^2 + b^2 + z^2 - 2br\sin\phi'}} d\phi' \\ &= \frac{\mu_0 I}{2\pi} \int_0^{\pi/2} \frac{b\left(2\sin^2\theta - 1\right)}{\sqrt{r^2 + b^2 + z^2 - 2br\left(2\sin^2\theta - 1\right)}} 2d\theta \\ &= \frac{\mu_0 I}{\pi} \int_0^{\pi/2} \frac{b\left(2\sin^2\theta - 1\right)}{\sqrt{(r+b)^2 + z^2 - 4br\sin^2\theta}} d\theta \\ &= \frac{\mu_0 I}{\pi} \int_0^{\pi/2} \frac{\sqrt{\frac{1}{(r+b)^2+z^2}} b\left(2\sin^2\theta - 1\right)}{\sqrt{1 - \frac{4br}{(r+b)^2+z^2}\sin^2\theta}} d\theta \\ &= \frac{\mu_0 I}{\pi k} \frac{1}{\sqrt{4br}} \int_0^{\pi/2} \frac{k^2 b\left(2\sin^2\theta - 1\right)}{\sqrt{1 - k^2\sin^2\theta}} d\theta \\ &= \frac{\mu_0 I}{2\pi k} \sqrt{\frac{b}{r}} \int_0^{\pi/2} \frac{2\left(k^2\sin^2\theta - \frac{1}{2}k^2\right)}{\sqrt{1 - k^2\sin^2\theta}} d\theta \\ &= \frac{\mu_0 I}{\pi k} \sqrt{\frac{b}{r}} \int_0^{\pi/2} \frac{1 - \frac{1}{2}k^2 - \sqrt{1 - k^2\sin^2\theta}\sqrt{1 - k^2\sin^2\theta}}{\sqrt{1 - k^2\sin^2\theta}} d\theta \\ &= \frac{\mu_0 I}{\pi k} \sqrt{\frac{b}{r}} \left[\int_0^{\pi/2} \frac{1 - \frac{1}{2}k^2}{\sqrt{1 - k^2\sin^2\theta}} d\theta - \int_0^{\pi/2} \sqrt{1 - k^2\sin^2\theta} d\theta\right] \\ &= \frac{\mu_0 I}{\pi k} \sqrt{\frac{b}{r}} \left[\left(1 - \frac{1}{2}k^2\right) K(k) - E(k)\right]. \end{aligned} \tag{A.7}$$

Using cylindrical coordinates, (A.1) is for the configuration shown in Figure A.1 given by:

$$\boldsymbol{B} = \boldsymbol{\nabla} \times \boldsymbol{A} = \begin{pmatrix} -\frac{\partial A_\phi}{\partial z} \\ 0 \\ \frac{1}{r}\frac{\partial (rA_\phi)}{\partial r} \end{pmatrix}, \tag{A.8}$$

with:

$$\frac{\partial A_\phi}{\partial z} = \frac{\partial k}{\partial z}\left[\frac{\partial A_\phi}{\partial k} + \frac{\partial A_\phi}{\partial K}\frac{\partial K}{\partial k} + \frac{\partial A_\phi}{\partial E}\frac{\partial E}{\partial k}\right], \tag{A.9}$$

and by applying $rA_\phi = f \cdot g$, with $f = \sqrt{br}$, and $g = \frac{\mu_0 I}{\pi k}\left[\left(1 - \frac{1}{2}k^2\right)K(k) - E(k)\right]$, it follows that:

$$\frac{\partial (rA_\phi)}{\partial r} = \frac{\partial f}{\partial r}g + f\frac{\partial k}{\partial r}\left[\frac{\partial g}{\partial k} + \frac{\partial g}{\partial K}\frac{\partial K}{\partial k} + \frac{\partial g}{\partial E}\frac{\partial E}{\partial k}\right]. \tag{A.10}$$

The individual terms of this equation are given by:

$$\begin{aligned}
\frac{\partial k}{\partial z} &= \frac{1}{2}\left(\frac{4br}{(r+b)^2 + z^2}\right)^{-\frac{1}{2}} \cdot \frac{-8brz}{\left((r+b)^2 + z^2\right)^2} = -\frac{zk^3}{4br} \\
\frac{\partial k}{\partial r} &= \frac{1}{2}\left(\frac{4br}{(r+b)^2 + z^2}\right)^{-\frac{1}{2}}\left[\frac{4b}{(r+b)^2 + z^2} - \frac{8br\,(r+b)}{\left((r+b)^2 + z^2\right)^2}\right] = \frac{2bk - rk^3 - bk^3}{4br} \\
\frac{\partial A_\phi}{\partial k} &= -\frac{\mu_0 I}{\pi k^2}\sqrt{\frac{b}{r}}\left[\left(1 - \frac{1}{2}k^2\right)K - E\right] - \frac{\mu_0 I}{\pi}\sqrt{\frac{b}{r}}K \\
\frac{\partial A_\phi}{\partial K} &= \frac{\mu_0 I}{\pi k}\sqrt{\frac{b}{r}}\left(1 - \frac{1}{2}k^2\right) \\
\frac{\partial A_\phi}{\partial E} &= -\frac{\mu_0 I}{\pi k}\sqrt{\frac{b}{r}} \\
\frac{\partial f}{\partial r} &= \frac{b}{2\sqrt{br}} \\
\frac{\partial g}{\partial k} &= -\frac{\mu_0 I}{\pi k^2}\left[\left(1 - \frac{1}{2}k^2\right)K - E\right] - \frac{\mu_0 I}{\pi}K \\
\frac{\partial g}{\partial K} &= \frac{\mu_0 I}{\pi k}\left(1 - \frac{1}{2}k^2\right) \\
\frac{\partial g}{\partial E} &= -\frac{\mu_0 I}{\pi k} \\
\frac{\partial K}{\partial k} &= \frac{E}{k\,(1-k^2)} - \frac{K}{k} \\
\frac{\partial E}{\partial k} &= \frac{E - K}{k}.
\end{aligned} \tag{A.11}$$

By substitution of (A.11) in (A.10) and (A.9), it follows that:

$$\begin{aligned}
\frac{\partial (rA_\phi)}{\partial r} &= \frac{\mu_0 I r}{2\pi\sqrt{(r+b)^2 + z^2}}\left[K(k) + \frac{b^2 - r^2 - z^2}{(r-b)^2 + z^2}E(k)\right] \\
\frac{\partial A_\phi}{\partial z} &= -\frac{\mu_0 I z}{2\pi r\sqrt{(r+b)^2 + z^2}}\left[-K(k) + \frac{b^2 + r^2 + z^2}{(r-b)^2 + z^2}E(k)\right],
\end{aligned} \tag{A.12}$$

which needs to be substituted in (A.8), resulting in:

$$\boldsymbol{B} = \frac{\mu_0 I}{2\pi\sqrt{(r+b)^2+z^2}} \begin{pmatrix} \frac{z}{r}\left[-K(k) + \frac{b^2+r^2+z^2}{(r-b)^2+z^2}E(k)\right] \\ 0 \\ \left[K(k) + \frac{b^2-r^2-z^2}{(r-b)^2+z^2}E(k)\right] \end{pmatrix}. \tag{A.13}$$

By converting (A.13) to cartesian coordinates ($r = \sqrt{p_x^2+p_y^2}$, $B_x = \frac{p_x}{\sqrt{p_x^2+p_y^2}}B_r = \frac{p_x}{r}B_r$, $B_y = \frac{p_y}{r}B_r$, $B_z = B_z$), the expression for the magnetic flux density $\boldsymbol{B}$ at the location of the sensor generated by the source coil is obtained:

$$\boldsymbol{B} = \frac{\mu_0 N I}{2\pi\sqrt{\left(\sqrt{p_x^2+p_y^2}+b\right)^2+p_z^2}} \begin{pmatrix} \frac{p_x p_z}{p_x^2+p_y^2}\left[-K(k) + \frac{b^2+p_x^2+p_y^2+p_z^2}{\left(\sqrt{p_x^2+p_y^2}-b\right)^2+p_z^2}E(k)\right] \\ \frac{p_y p_z}{p_x^2+p_y^2}\left[-K(k) + \frac{b^2+p_x^2+p_y^2+p_z^2}{\left(\sqrt{p_x^2+p_y^2}-b\right)^2+p_z^2}E(k)\right] \\ \left[K(k) + \frac{b^2-p_x^2-p_y^2-p_z^2}{\left(\sqrt{p_x^2+p_y^2}-b\right)^2+p_z^2}E(k)\right] \end{pmatrix}, \tag{A.14}$$

where N denotes the number of windings, $K(k)$ and $E(k)$ have been defined in (A.6), and:

$$k = \sqrt{\frac{4b\sqrt{p_x^2+p_y^2}}{\left(\sqrt{p_x^2+p_y^2}+b\right)^2+p_z^2}}. \tag{A.15}$$

A.1.2 Dipole Approximation

If the point of interest satisfies $R = \sqrt{r^2+z^2} \gg b$, (A.5) can be simplified:

$$\begin{aligned} A_\phi &= \frac{\mu_0 I}{2\pi}\int_{-\pi/2}^{\pi/2} \frac{b\sin\phi'}{\sqrt{r^2+b^2+z^2-2br\sin\phi'}}d\phi' \\ &= \frac{\mu_0 I}{2\pi}\int_{-\pi/2}^{\pi/2} \frac{1}{R}\frac{b\sin\phi'}{\sqrt{1+\frac{b^2}{R^2}-\frac{2br\sin\phi'}{R^2}}}d\phi' \\ &\approx \frac{\mu_0 I}{2\pi}\int_{-\pi/2}^{\pi/2} \frac{b\sin\phi'}{R}\frac{1}{\sqrt{1-\frac{2br\sin\phi'}{R^2}}}d\phi' \\ &\approx \frac{\mu_0 I}{2\pi}\int_{-\pi/2}^{\pi/2} \frac{b\sin\phi'}{R}\left(1+\frac{br\sin\phi'}{R^2}\right)d\phi' \\ &= \frac{\mu_0 I b}{2\pi R}\int_{-\pi/2}^{\pi/2} \left(\sin\phi' + \frac{br\sin^2\phi'}{R^2}\right)d\phi' \\ &= \frac{\mu_0 I b}{2\pi R}\int_{-\pi/2}^{\pi/2} \left(\sin\phi' + \frac{br}{R^2}\left(\frac{1}{2}-\frac{1}{2}\cos 2\phi'\right)\right)d\phi' \\ &= \frac{\mu_0 I b^2 r}{4R^3} = \frac{\mu_0 I b^2 r}{4\left(r^2+z^2\right)^{3/2}}, \end{aligned} \tag{A.16}$$

which means for $\boldsymbol{B}$:

$$\boldsymbol{B} = \boldsymbol{\nabla}\times\boldsymbol{A} = \begin{pmatrix} -\frac{\partial A_\phi}{\partial z} \\ 0 \\ \frac{1}{r}\frac{\partial\left(rA_\phi\right)}{\partial r} \end{pmatrix} = \frac{\mu_0 I b^2}{4\left(r^2+z^2\right)^{\frac{5}{2}}}\begin{pmatrix} 3rz \\ 0 \\ 2z^2-r^2 \end{pmatrix}. \tag{A.17}$$

For N windings, the magnetic flux density using the dipole approximation, expressed in cartesian coordinates, is given by:

$$\boldsymbol{B} = \frac{\mu_0 N I b^2}{4\left(p_x^2 + p_y^2 + p_z^2\right)^{\frac{5}{2}}} \begin{pmatrix} 3p_x p_z \\ 3p_y p_z \\ 2p_z^2 - p_x^2 - p_y^2 \end{pmatrix}. \tag{A.18}$$

A.2 Partial Derivatives

This section describes the derivation of the partial derivatives of the magnetic flux density $\boldsymbol{B}$ with respect to the position error $\delta\boldsymbol{p}$. Let $\hat{\boldsymbol{p}}$ be the estimation of the true position $\boldsymbol{p}$, and:

$$\hat{\boldsymbol{p}} = \boldsymbol{p} + \delta\boldsymbol{p}. \tag{A.19}$$

First, the partial derivatives of the magnetic flux density using the analytical model are derived, followed by the partial derivatives of the magnetic flux density using the dipole approximation.

A.2.1 Analytical Model

In order to calculate the partial derivatives of the magnetic flux density with respect to the position error, (A.14) is separated into multiple functions:

$$\hat{\boldsymbol{B}} = \begin{pmatrix} \hat{p}_x f g\left[-K(k) + hiE(k)\right] \\ \hat{p}_y f g\left[-K(k) + hiE(k)\right] \\ f\left[K(k) + hjE(k)\right] \end{pmatrix}, \tag{A.20}$$

with

$$\begin{aligned} f &= \frac{\mu_0 N I}{2\pi\sqrt{\left(\sqrt{\hat{p}_x^2 + \hat{p}_y^2} + b\right)^2 + \hat{p}_z^2}} \\ g &= \frac{\hat{p}_z}{\hat{p}_x^2 + \hat{p}_y^2} \\ h &= \frac{1}{\left(\sqrt{\hat{p}_x^2 + \hat{p}_y^2} - b\right)^2 + \hat{p}_z^2} \\ i &= b^2 + \hat{p}_x^2 + \hat{p}_y^2 + \hat{p}_z^2 \\ j &= b^2 - \hat{p}_x^2 - \hat{p}_y^2 - \hat{p}_z^2. \end{aligned} \tag{A.21}$$

The partial derivatives of $\hat{\boldsymbol{B}}$ with respect to δp_x are then given by:

$$
\begin{aligned}
\frac{\partial \hat{B}_x}{\partial \delta p_x} &= fg\left(-K+hiE\right)+\hat{p}_x\left(\frac{\partial f}{\partial \delta p_x}g\left(-K+hiE\right)+f\left(\frac{\partial g}{\partial \delta p_x}\left(-K+hiE\right)+gQ\right)\right)\\
\frac{\partial \hat{B}_y}{\partial \delta p_x} &= \hat{p}_y\left(\frac{\partial f}{\partial \delta p_x}g\left(-K+hiE\right)+f\left(\frac{\partial g}{\partial \delta p_x}\left(-K+hiE\right)+gQ\right)\right)\\
\frac{\partial \hat{B}_z}{\partial \delta p_x} &= \frac{\partial f}{\partial \delta p_x}\left(K+hjE\right)+f\left(\frac{\partial K}{\partial k}\frac{\partial k}{\partial \delta p_x}+\frac{\partial h}{\partial \delta p_x}jE+h\left(\frac{\partial j}{\partial \delta p_x}E+j\frac{\partial E}{\partial k}\frac{\partial k}{\partial \delta p_x}\right)\right)\\
Q &= \left(-\frac{\partial K}{\partial k}\frac{\partial k}{\partial \delta p_x}+\frac{\partial h}{\partial \delta p_x}iE+h\left(\frac{\partial i}{\partial \delta p_x}E+i\frac{\partial E}{\partial k}\frac{\partial k}{\partial \delta p_x}\right)\right). \qquad \text{(A.22)}
\end{aligned}
$$

Similarly, the partial derivatives of $\hat{\boldsymbol{B}}$ with respect to δp_y are given by:

$$
\begin{aligned}
\frac{\partial \hat{B}_x}{\partial \delta p_y} &= \hat{p}_x\left(\frac{\partial f}{\partial \delta p_y}g\left(-K+hiE\right)+f\left(\frac{\partial g}{\partial \delta p_y}\left(-K+hiE\right)+gR\right)\right)\\
\frac{\partial \hat{B}_y}{\partial \delta p_y} &= fg\left(-K+hiE\right)+\hat{p}_y\left(\frac{\partial f}{\partial \delta p_y}g\left(-K+hiE\right)+f\left(\frac{\partial g}{\partial \delta p_y}\left(-K+hiE\right)+gR\right)\right)\\
\frac{\partial \hat{B}_z}{\partial \delta p_y} &= \frac{\partial f}{\partial \delta p_y}\left(K+hjE\right)+f\left(\frac{\partial K}{\partial k}\frac{\partial k}{\partial \delta p_y}+\frac{\partial h}{\partial \delta p_y}jE+h\left(\frac{\partial j}{\partial \delta p_y}E+j\frac{\partial E}{\partial k}\frac{\partial k}{\partial \delta p_y}\right)\right)\\
R &= \left(-\frac{\partial K}{\partial k}\frac{\partial k}{\partial \delta p_y}+\frac{\partial h}{\partial \delta p_y}iE+h\left(\frac{\partial i}{\partial \delta p_y}E+i\frac{\partial E}{\partial k}\frac{\partial k}{\partial \delta p_y}\right)\right), \qquad \text{(A.23)}
\end{aligned}
$$

and the partial derivatives of $\hat{\boldsymbol{B}}$ with respect to δp_z are given by:

$$
\begin{aligned}
\frac{\partial \hat{B}_x}{\partial \delta p_z} &= \hat{p}_x\left(\frac{\partial f}{\partial \delta p_z}g\left(-K+hiE\right)+f\left(\frac{\partial g}{\partial \delta p_z}\left(-K+hiE\right)+gS\right)\right)\\
\frac{\partial \hat{B}_y}{\partial \delta p_z} &= \hat{p}_y\left(\frac{\partial f}{\partial \delta p_z}g\left(-K+hiE\right)+f\left(\frac{\partial g}{\partial \delta p_z}\left(-K+hiE\right)+gS\right)\right)\\
\frac{\partial \hat{B}_z}{\partial \delta p_z} &= \frac{\partial f}{\partial \delta p_z}\left(K+hjE\right)+f\left(\frac{\partial K}{\partial k}\frac{\partial k}{\partial \delta p_z}+\frac{\partial h}{\partial \delta p_z}jE+h\left(\frac{\partial j}{\partial \delta p_z}E+j\frac{\partial E}{\partial k}\frac{\partial k}{\partial \delta p_z}\right)\right)\\
S &= \left(-\frac{\partial K}{\partial k}\frac{\partial k}{\partial \delta p_z}+\frac{\partial h}{\partial \delta p_z}iE+h\left(\frac{\partial i}{\partial \delta p_z}E+i\frac{\partial E}{\partial k}\frac{\partial k}{\partial \delta p_z}\right)\right). \qquad \text{(A.24)}
\end{aligned}
$$

The individual terms of (A.22), (A.23), and (A.24) are given by:

$$
\begin{aligned}
\frac{\partial f}{\partial \delta p_x} &= \frac{-\mu_0 N I \hat{p}_x \left(\sqrt{\hat{p}_x^2+\hat{p}_y^2}+b\right)}{2\pi\left(\left(\sqrt{\hat{p}_x^2+\hat{p}_y^2}+b\right)^2+\hat{p}_z^2\right)^{\frac{3}{2}}\sqrt{\hat{p}_x^2+\hat{p}_y^2}} \\
\frac{\partial f}{\partial \delta p_y} &= \frac{-\mu_0 N I \hat{p}_y \left(\sqrt{\hat{p}_x^2+\hat{p}_y^2}+b\right)}{2\pi\left(\left(\sqrt{\hat{p}_x^2+\hat{p}_y^2}+b\right)^2+\hat{p}_z^2\right)^{\frac{3}{2}}\sqrt{\hat{p}_x^2+\hat{p}_y^2}} \\
\frac{\partial f}{\partial \delta p_z} &= \frac{-\mu_0 N I \hat{p}_z}{2\pi\left(\left(\sqrt{\hat{p}_x^2+\hat{p}_y^2}+b\right)^2+\hat{p}_z^2\right)^{\frac{3}{2}}} \\
\frac{\partial g}{\partial \delta p_x} &= \frac{-2\hat{p}_x\hat{p}_z}{\left(\hat{p}_x^2+\hat{p}_y^2\right)^2}, \quad \frac{\partial g}{\partial \delta p_y} = \frac{-2\hat{p}_y\hat{p}_z}{\left(\hat{p}_x^2+\hat{p}_y^2\right)^2}, \quad \frac{\partial g}{\partial \delta p_z} = \frac{1}{\hat{p}_x^2+\hat{p}_y^2} \\
\frac{\partial h}{\partial \delta p_x} &= \frac{-2\hat{p}_x \left(\sqrt{\hat{p}_x^2+\hat{p}_y^2}-b\right)}{\left(\left(\sqrt{\hat{p}_x^2+\hat{p}_y^2}-b\right)^2+\hat{p}_z^2\right)^2\sqrt{\hat{p}_x^2+\hat{p}_y^2}} \\
\frac{\partial h}{\partial \delta p_y} &= \frac{-2\hat{p}_y \left(\sqrt{\hat{p}_x^2+\hat{p}_y^2}-b\right)}{\left(\left(\sqrt{\hat{p}_x^2+\hat{p}_y^2}-b\right)^2+\hat{p}_z^2\right)^2\sqrt{\hat{p}_x^2+\hat{p}_y^2}} \\
\frac{\partial h}{\partial \delta p_z} &= \frac{-2\hat{p}_z}{\left(\left(\sqrt{\hat{p}_x^2+\hat{p}_y^2}-b\right)^2+\hat{p}_z^2\right)^2} \\
\frac{\partial i}{\partial \delta p_x} &= 2\hat{p}_x, \quad \frac{\partial i}{\partial \delta p_y} = 2\hat{p}_y, \quad \frac{\partial i}{\partial \delta p_z} = 2\hat{p}_z \\
\frac{\partial j}{\partial \delta p_x} &= -2\hat{p}_x, \quad \frac{\partial j}{\partial \delta p_y} = -2\hat{p}_y, \quad \frac{\partial j}{\partial \delta p_z} = -2\hat{p}_z \\
\frac{\partial k}{\partial \delta p_x} &= \frac{\frac{b\hat{p}_x}{\sqrt{\hat{p}_x^2+\hat{p}_y^2}\left(\left(\sqrt{\hat{p}_x^2+\hat{p}_y^2}+b\right)^2+\hat{p}_z^2\right)} - \frac{2b\hat{p}_x\left(\sqrt{\hat{p}_x^2+\hat{p}_y^2}+b\right)}{\left(\left(\sqrt{\hat{p}_x^2+\hat{p}_y^2}+b\right)^2+\hat{p}_z^2\right)^2}}{\sqrt{\frac{b\sqrt{\hat{p}_x^2+\hat{p}_y^2}}{\left(\sqrt{\hat{p}_x^2+\hat{p}_y^2}+b\right)^2+\hat{p}_z^2}}} \\
\frac{\partial k}{\partial \delta p_y} &= \frac{\frac{b\hat{p}_y}{\sqrt{\hat{p}_x^2+\hat{p}_y^2}\left(\left(\sqrt{\hat{p}_x^2+\hat{p}_y^2}+b\right)^2+\hat{p}_z^2\right)} - \frac{2b\hat{p}_y\left(\sqrt{\hat{p}_x^2+\hat{p}_y^2}+b\right)}{\left(\left(\sqrt{\hat{p}_x^2+\hat{p}_y^2}+b\right)^2+\hat{p}_z^2\right)^2}}{\sqrt{\frac{b\sqrt{\hat{p}_x^2+\hat{p}_y^2}}{\left(\sqrt{\hat{p}_x^2+\hat{p}_y^2}+b\right)^2+\hat{p}_z^2}}} \\
\frac{\partial k}{\partial \delta p_z} &= \frac{-2b\hat{p}_z\sqrt{\hat{p}_x^2+\hat{p}_y^2}}{\sqrt{\frac{b\sqrt{\hat{p}_x^2+\hat{p}_y^2}}{\left(\sqrt{\hat{p}_x^2+\hat{p}_y^2}+b\right)^2+\hat{p}_z^2}}\left(\left(\sqrt{\hat{p}_x^2+\hat{p}_y^2}+b\right)^2+\hat{p}_z^2\right)^2}.
\end{aligned}
\tag{A.25}
$$

A.2.2 Dipole Approximation

In order to calculate the partial derivatives of the magnetic flux density using the dipole approximation, (A.18) is separated into multiple functions:

$$\hat{\boldsymbol{B}} = \begin{pmatrix} fg \\ fh \\ fi \end{pmatrix}, \tag{A.26}$$

with

$$f = \frac{\mu_0 N I b^2}{4\left(\hat{p}_x^2 + \hat{p}_y^2 + \hat{p}_z^2\right)^{\frac{5}{2}}} \tag{A.27}$$

$$\begin{aligned} g &= 3\hat{p}_x\hat{p}_z \\ h &= 3\hat{p}_y\hat{p}_z \\ i &= 2\hat{p}_z^2 - \hat{p}_x^2 - \hat{p}_y^2. \end{aligned} \tag{A.28}$$

The partial derivatives of $\hat{\boldsymbol{B}}$ with respect to δp_x are then given by:

$$\begin{aligned} \frac{\partial \hat{B}_x}{\partial \delta p_x} &= \frac{\partial f}{\partial \delta p_x} g + f \frac{\partial g}{\partial \delta p_x} \\ \frac{\partial \hat{B}_y}{\partial \delta p_x} &= \frac{\partial f}{\partial \delta p_x} h + f \frac{\partial h}{\partial \delta p_x} \\ \frac{\partial \hat{B}_z}{\partial \delta p_x} &= \frac{\partial f}{\partial \delta p_x} i + f \frac{\partial i}{\partial \delta p_x}. \end{aligned} \tag{A.29}$$

Similarly, the partial derivatives of $\hat{\boldsymbol{B}}$ with respect to δp_y are given by:

$$\begin{aligned} \frac{\partial \hat{B}_x}{\partial \delta p_y} &= \frac{\partial f}{\partial \delta p_y} g + f \frac{\partial g}{\partial \delta p_y} \\ \frac{\partial \hat{B}_y}{\partial \delta p_y} &= \frac{\partial f}{\partial \delta p_y} h + f \frac{\partial h}{\partial \delta p_y} \\ \frac{\partial \hat{B}_z}{\partial \delta p_y} &= \frac{\partial f}{\partial \delta p_y} i + f \frac{\partial i}{\partial \delta p_y}. \end{aligned} \tag{A.30}$$

and the partial derivatives of $\hat{\boldsymbol{B}}$ with respect to δp_z are given by:

$$\begin{aligned} \frac{\partial \hat{B}_x}{\partial \delta p_z} &= \frac{\partial f}{\partial \delta p_z} g + f \frac{\partial g}{\partial \delta p_z} \\ \frac{\partial \hat{B}_y}{\partial \delta p_z} &= \frac{\partial f}{\partial \delta p_z} h + f \frac{\partial h}{\partial \delta p_z} \\ \frac{\partial \hat{B}_z}{\partial \delta p_z} &= \frac{\partial f}{\partial \delta p_z} i + f \frac{\partial i}{\partial \delta p_z}. \end{aligned} \tag{A.31}$$

The individual terms of (A.29), (A.30), and (A.31) are given by:

$$
\begin{aligned}
\frac{\partial f}{\partial \delta p_x} &= \frac{-5\mu_0 N I b^2 \hat{p}_x}{4\left(\hat{p}_x^2+\hat{p}_y^2+\hat{p}_z^2\right)^{\frac{7}{2}}} \\
\frac{\partial f}{\partial \delta p_y} &= \frac{-5\mu_0 N I b^2 \hat{p}_y}{4\left(\hat{p}_x^2+\hat{p}_y^2+\hat{p}_z^2\right)^{\frac{7}{2}}} \\
\frac{\partial f}{\partial \delta p_z} &= \frac{-5\mu_0 N I b^2 \hat{p}_z}{4\left(\hat{p}_x^2+\hat{p}_y^2+\hat{p}_z^2\right)^{\frac{7}{2}}} \\
\frac{\partial g}{\partial \delta p_x} &= 3\hat{p}_z, \quad \frac{\partial g}{\partial \delta p_y} = 0, \quad \frac{\partial g}{\partial \delta p_z} = 3\hat{p}_x \\
\frac{\partial h}{\partial \delta p_x} &= 0, \quad \frac{\partial h}{\partial \delta p_y} = 3\hat{p}_z, \quad \frac{\partial h}{\partial \delta p_z} = 3\hat{p}_y \\
\frac{\partial i}{\partial \delta p_x} &= -2\hat{p}_x, \quad \frac{\partial i}{\partial \delta p_y} = -2\hat{p}_y, \quad \frac{\partial i}{\partial \delta p_z} = 4\hat{p}_z.
\end{aligned}
\tag{A.32}
$$

Substitution of (A.32) in (A.29) results in the desired equation:

$$
\frac{\partial \hat{\boldsymbol{B}}}{\partial \delta p_x} = \frac{\mu_0 N I b^2}{4\left(\hat{p}_x^2+\hat{p}_y^2+\hat{p}_z^2\right)^{\frac{7}{2}}} \begin{pmatrix} -12\hat{p}_x^2\hat{p}_z + 3\hat{p}_y^2\hat{p}_z + 3\hat{p}_z^3 \\ -15\hat{p}_x\hat{p}_y\hat{p}_z \\ 3\hat{p}_x^3 + 3\hat{p}_x\hat{p}_y^2 - 12\hat{p}_x\hat{p}_z^2 \end{pmatrix}. \tag{A.33}
$$

Similarly, by substitution of (A.32) in (A.30):

$$
\frac{\partial \hat{\boldsymbol{B}}}{\partial \delta p_y} = \frac{\mu_0 N I b^2}{4\left(\hat{p}_x^2+\hat{p}_y^2+\hat{p}_z^2\right)^{\frac{7}{2}}} \begin{pmatrix} -15\hat{p}_x\hat{p}_y\hat{p}_z \\ 3\hat{p}_x^2\hat{p}_z - 12\hat{p}_y^2\hat{p}_z + 3\hat{p}_z^3 \\ 3\hat{p}_x^2\hat{p}_y + 3\hat{p}_y^3 - 12\hat{p}_y\hat{p}_z^2 \end{pmatrix}, \tag{A.34}
$$

and by substitution of (A.32) in (A.31):

$$
\frac{\partial \hat{\boldsymbol{B}}}{\partial \delta p_z} = \frac{\mu_0 N I b^2}{4\left(\hat{p}_x^2+\hat{p}_y^2+\hat{p}_z^2\right)^{\frac{7}{2}}} \begin{pmatrix} 3\hat{p}_x^3 + 3\hat{p}_x\hat{p}_y^2 - 12\hat{p}_x\hat{p}_z^2 \\ 3\hat{p}_x^2\hat{p}_y + 3\hat{p}_y^3 - 12\hat{p}_y\hat{p}_z^2 \\ 9\hat{p}_x^2\hat{p}_z + 9\hat{p}_y^2\hat{p}_z - 6\hat{p}_z^3 \end{pmatrix}. \tag{A.35}
$$

B

Derivation of the Process Model

The error equations that comprise the process model can be derived by writing the derivative of the state as a function of the state itself. The error state $\delta\boldsymbol{x}$ denotes the difference between the true state $\boldsymbol{x}$ and an estimation of the state $\hat{\boldsymbol{x}}$. The error state is chosen as:

$$\delta\boldsymbol{x} = \begin{pmatrix}\delta\boldsymbol{p} & \delta\boldsymbol{v} & \delta\boldsymbol{\theta} & \delta\boldsymbol{a} & \delta\boldsymbol{\omega}\end{pmatrix}^T, \tag{B.1}$$

where $\delta\boldsymbol{p}$ denotes the position error, $\delta\boldsymbol{v}$ the velocity error, $\delta\boldsymbol{\theta}$ the orientation error, $\delta\boldsymbol{a}$ the accelerometer bias, and $\delta\boldsymbol{\omega}$ the gyroscope bias. For the position error, velocity error, accelerometer bias, and gyroscope bias, the derivative of the error state as a function of the state itself is simply given by:

$$\hat{\boldsymbol{x}} = \boldsymbol{x} + \delta\boldsymbol{x}. \tag{B.2}$$

For the orientation error $\delta\boldsymbol{\theta}$, rotation matrices are used:

$$\hat{\boldsymbol{R}}_s^c = \boldsymbol{R}_s^c \delta\boldsymbol{R} \approx \boldsymbol{R}_s^c \left(\boldsymbol{I} + \tilde{\delta\boldsymbol{\theta}}\right) \Rightarrow \tilde{\delta\boldsymbol{\theta}} \approx \left(\boldsymbol{R}_s^c\right)^T \hat{\boldsymbol{R}}_s^c - \boldsymbol{I}, \tag{B.3}$$

where $\boldsymbol{R}_s^c$ denotes the rotation matrix describing the orientation of frame Ψ_s with respect to frame Ψ_c. The columns of $\boldsymbol{R}_s^c$ are the unit axes of frame Ψ_s expressed in frame Ψ_c: $\boldsymbol{R}_s^c = \begin{pmatrix}\boldsymbol{X}_s^c & \boldsymbol{Y}_s^c & \boldsymbol{Z}_s^c\end{pmatrix}$. The tilde operator ($\tilde{}$) indicates a skew-symmetric matrix form:

$$\tilde{\delta\boldsymbol{\theta}} = \begin{pmatrix} 0 & -\delta\theta_z & \delta\theta_y \\ \delta\theta_z & 0 & -\delta\theta_x \\ -\delta\theta_y & \delta\theta_x & 0 \end{pmatrix}. \tag{B.4}$$

The orientation is estimated by integration of angular velocity using the following differential equation [59]:

$$\dot{\boldsymbol{R}}_s^c = \boldsymbol{R}_s^c \tilde{\boldsymbol{\omega}}_s^{s,c}, \tag{B.5}$$

where $\boldsymbol{\omega}_s^{s,c}$ denotes the angular velocity of frame Ψ_s with respect to Ψ_c, expressed in Ψ_s. The derivative of the orientation error is found by applying (B.3), (B.5), and neglecting the product of errors:

$$\begin{aligned}
\dot{\tilde{\delta\boldsymbol{\theta}}} &= \left(\dot{\boldsymbol{R}}_s^c\right)^T \hat{\boldsymbol{R}}_s^c + \left(\boldsymbol{R}_s^c\right)^T \dot{\hat{\boldsymbol{R}}}_s^c \\
&= \left(\boldsymbol{R}_s^c \tilde{\boldsymbol{\omega}}_s^{s,c}\right)^T \boldsymbol{R}_s^c \left(\boldsymbol{I} + \tilde{\delta\boldsymbol{\theta}}\right) + \left(\boldsymbol{R}_s^c\right)^T \hat{\boldsymbol{R}}_s^c \tilde{\hat{\boldsymbol{\omega}}}_s^{s,c} \\
&= \left(\boldsymbol{R}_s^c \tilde{\boldsymbol{\omega}}_s^{s,c}\right)^T \boldsymbol{R}_s^c \left(\boldsymbol{I} + \tilde{\delta\boldsymbol{\theta}}\right) + \left(\boldsymbol{R}_s^c\right)^T \boldsymbol{R}_s^c \left(\boldsymbol{I} + \tilde{\delta\boldsymbol{\theta}}\right) \tilde{\hat{\boldsymbol{\omega}}}_s^{s,c} \\
&= -\tilde{\boldsymbol{\omega}}_s^{s,c} \left(\boldsymbol{I} + \tilde{\delta\boldsymbol{\theta}}\right) + \left(\boldsymbol{I} + \tilde{\delta\boldsymbol{\theta}}\right) \left(\tilde{\boldsymbol{\omega}}_s^{s,c} + \tilde{\delta\boldsymbol{\omega}}\right) \\
&\approx \tilde{\delta\boldsymbol{\omega}} - \tilde{\boldsymbol{\omega}}_s^{s,c} \tilde{\delta\boldsymbol{\theta}} + \tilde{\delta\boldsymbol{\theta}} \tilde{\boldsymbol{\omega}}_s^{s,c}.
\end{aligned} \tag{B.6}$$

The vector representation of the orientation error $\dot{\delta\boldsymbol{\theta}}$ is found by writing out the skew-symmetric matrices indicated by the tilde operator $(\tilde{\ })$:

$$
\begin{aligned}
\begin{pmatrix} 0 & -\dot{\delta\theta}_z & \dot{\delta\theta}_y \\ \dot{\delta\theta}_z & 0 & -\dot{\delta\theta}_x \\ -\dot{\delta\theta}_y & \dot{\delta\theta}_x & 0 \end{pmatrix} &= \begin{pmatrix} 0 & -\delta\omega_z & \delta\omega_y \\ \delta\omega_z & 0 & -\delta\omega_x \\ -\delta\omega_y & \delta\omega_x & 0 \end{pmatrix} \\
&\quad - \begin{pmatrix} 0 & -\omega_z & \omega_y \\ \omega_z & 0 & -\omega_x \\ -\omega_y & \omega_x & 0 \end{pmatrix} \begin{pmatrix} 0 & -\delta\theta_z & \delta\theta_y \\ \delta\theta_z & 0 & -\delta\theta_x \\ -\delta\theta_y & \delta\theta_x & 0 \end{pmatrix} \\
&\quad + \begin{pmatrix} 0 & -\delta\theta_z & \delta\theta_y \\ \delta\theta_z & 0 & -\delta\theta_x \\ -\delta\theta_y & \delta\theta_x & 0 \end{pmatrix} \begin{pmatrix} 0 & -\omega_z & \omega_y \\ \omega_z & 0 & -\omega_x \\ -\omega_y & \omega_x & 0 \end{pmatrix} \\
&= \begin{pmatrix} 0 & -\delta\omega_z & \delta\omega_y \\ \delta\omega_z & 0 & -\delta\omega_x \\ -\delta\omega_y & \delta\omega_x & 0 \end{pmatrix} \\
&\quad - \begin{pmatrix} -\omega_z\delta\theta_z - \omega_y\delta\theta_y & \omega_y\delta\theta_x & \omega_z\delta\theta_x \\ \omega_x\delta\theta_y & -\omega_z\delta\theta_z - \omega_x\delta\theta_x & \omega_z\delta\theta_y \\ \omega_x\delta\theta_z & \omega_y\delta\theta_z & -\omega_y\delta\theta_y - \omega_x\delta\theta_x \end{pmatrix} \\
&\quad + \begin{pmatrix} -\omega_z\delta\theta_z - \omega_y\delta\theta_y & \omega_x\delta\theta_y & \omega_x\delta\theta_z \\ \omega_y\delta\theta_x & -\omega_z\delta\theta_z - \omega_x\delta\theta_x & \omega_y\delta\theta_z \\ \omega_z\delta\theta_x & \omega_z\delta\theta_y & -\omega_y\delta\theta_y - \omega_x\delta\theta_x \end{pmatrix} \\
&= \begin{pmatrix} 0 & -\delta\omega_z & \delta\omega_y \\ \delta\omega_z & 0 & -\delta\omega_x \\ -\delta\omega_y & \delta\omega_x & 0 \end{pmatrix} \\
&\quad + \begin{pmatrix} 0 & \omega_x\delta\theta_y - \omega_y\delta\theta_x & \omega_x\delta\theta_z - \omega_z\delta\theta_x \\ \omega_y\delta\theta_x - \omega_x\delta\theta_y & 0 & \omega_y\delta\theta_z - \omega_z\delta\theta_y \\ \omega_z\delta\theta_x - \omega_x\delta\theta_z & \omega_z\delta\theta_y - \omega_y\delta\theta_z & 0 \end{pmatrix}. \qquad \text{(B.7)}
\end{aligned}
$$

Sorting the individual components of the vector $\dot{\delta\boldsymbol{\theta}} = \begin{pmatrix} \dot{\delta\theta}_x & \dot{\delta\theta}_y & \dot{\delta\theta}_z \end{pmatrix}^T$ results in:

$$
\dot{\delta\boldsymbol{\theta}} = \delta\boldsymbol{\omega} + \begin{pmatrix} \omega_z\delta\theta_y - \omega_y\delta\theta_z \\ \omega_x\delta\theta_z - \omega_z\delta\theta_x \\ \omega_y\delta\theta_x - \omega_x\delta\theta_y \end{pmatrix} = \delta\boldsymbol{\omega} - \tilde{\boldsymbol{\omega}}_s^{s,c}\delta\boldsymbol{\theta}. \qquad \text{(B.8)}
$$

It should be noted that the indices $()_s^{s,c}$ have been omitted for readability. The derivative of the velocity error is found by applying (B.2), (B.3) and neglecting the product of errors:

$$
\begin{aligned}
\dot{\delta\boldsymbol{v}} &= \dot{\hat{\boldsymbol{v}}}_s^c - \dot{\boldsymbol{v}}_s^c \\
&= \hat{\boldsymbol{R}}_s^c\hat{\boldsymbol{s}}^s - \boldsymbol{R}_s^c\boldsymbol{s}^s \\
&= \boldsymbol{R}_s^c\left(\boldsymbol{I} + \tilde{\delta\boldsymbol{\theta}}\right)(\boldsymbol{s}^s + \delta\boldsymbol{a}) - \boldsymbol{R}_s^c\boldsymbol{s}^s \\
&= \boldsymbol{R}_s^c\boldsymbol{s}^s + \boldsymbol{R}_s^c\delta\boldsymbol{a} + \boldsymbol{R}_s^c\tilde{\delta\boldsymbol{\theta}}\boldsymbol{s}^s + \boldsymbol{R}_s^c\tilde{\delta\boldsymbol{\theta}}\delta\boldsymbol{a} - \boldsymbol{R}_s^c\boldsymbol{s}^s \\
&\approx \boldsymbol{R}_s^c\delta\boldsymbol{a} - \boldsymbol{R}_s^c\tilde{\boldsymbol{s}}^s\delta\boldsymbol{\theta}, \qquad \text{(B.9)}
\end{aligned}
$$

and the derivative of the position:

$$
\dot{\delta\boldsymbol{p}} = \delta\boldsymbol{v}. \qquad \text{(B.10)}
$$

The accelerometer bias and gyroscope bias are modeled as first order Markov processes:

$$\begin{aligned}\dot{\delta\boldsymbol{a}} &= -\beta_a \delta\boldsymbol{a} + \sqrt{2\sigma_a^2\beta_a}\boldsymbol{u} \\ \dot{\delta\boldsymbol{\omega}} &= -\beta_\omega \delta\boldsymbol{\omega} + \sqrt{2\sigma_\omega^2\beta_\omega}\boldsymbol{u},\end{aligned} \tag{B.11}$$

where $\boldsymbol{u}$ denotes unity white noise. Summarizing, the process model is given by:

$$\begin{aligned}\dot{\delta\boldsymbol{p}} &= \delta\boldsymbol{v} \\ \dot{\delta\boldsymbol{v}} &= \boldsymbol{R}_s^c \delta\boldsymbol{a} - \boldsymbol{R}_s^c \tilde{\boldsymbol{s}}^s \delta\boldsymbol{\theta} \\ \dot{\delta\boldsymbol{\theta}} &= \delta\boldsymbol{\omega} - \tilde{\boldsymbol{\omega}}_s^{s,c} \delta\boldsymbol{\theta} \\ \dot{\delta\boldsymbol{a}} &= -\beta_a \delta\boldsymbol{a} \\ \dot{\delta\boldsymbol{\omega}} &= -\beta_\omega \delta\boldsymbol{\omega}.\end{aligned} \tag{B.12}$$

References

[1] G. A. Borelli, *De Motu Animalium*. Lugduni Batavorum, 1679.

[2] W. Braune and O. Fischer, *Determintation of the Moments of Inertia of the Human Body and Its Limbs*. Berlin: Springer-Verlag, 1989.

[3] S. I. Newton, *Philosophia Materialis Principia Mathematica*. In: Danbury: Encyclopedia Americana. Grolier Incorporated, 1988.

[4] R. Descartes, *Oeuvres De Descartes*. French and European Publication, 1596.

[5] R. Baker, "The History of Gait Analysis before the Advent of Modern Computers," *Gait and Posture*, vol. 26, no. 3, pp. 331–342, 2007.

[6] W. Weber and E. Weber, *Mechanik Der Menschlichen Gehwerkzeuge*. Gottingen: Fisher-Verlag, 1836.

[7] E. Muybridge, *Complete Human and Animal Locomotion*. Dover Publishers, 1887.

[8] H. D. Eberhart, *Fundamental Studies of Human Locomotion and Other Information Relating to Design of Artificial Limbs*. Berkeley, California, 1947.

[9] V. T. Inman, H. J. Ralston, and F. Todd, *Human Walking*. Baltimore: Williams and Wilkins, 1981.

[10] E. J. Marey, "De La Mesure Dans Les Differents Acts De La Locomotion," *Comptes Rendues de l'Academie des Sciences de Paris*, vol. 97, pp. 820–825, 1883.

[11] H. D. Eberhart and V. T. Inman, "An Evaluation of Experimental Procedures Used in a Fundamental Study of Human Locomotion," *Annals of the New York Academy of Sciences*, vol. 51, no. Human Engineering, pp. 1213–1228, 1951.

[12] K. Meyer, H. L. Applewhite, and F. A. Biocca, "A Survey of Position Trackers," *Presence: Teleoperators and Virtual Environments*, vol. 1, no. 2, pp. 173–200, 1992.

[13] Optotrak, http://www.ndigital.com.

[14] Vicon, http://www.vicon.com.

[15] D. Roetenberg, C. T. M. Baten, and P. H. Veltink, "Estimating Body Segment Orientation by Applying Inertial and Magnetic Sensing near Ferromagnetic Materials," *IEEE Transactions on Neural Systems and Rehabilitation Engineering*, vol. 15, no. 3, pp. 469–471, 2007.

[16] X. Yun and E. R. Bachmann, "Design, Implementation, and Experimental Results of a Quaternion-Based Kalman Filter for Human Body Motion Tracking," *IEEE Transactions on Robotics*, vol. 22, no. 6, pp. 1216–1227, 2006.

[17] A. M. Sabatini, "Quaternion-Based Extended Kalman Filter for Determining Orientation by Inertial and Magnetic Sensing," *IEEE Transactions on Biomedical Engineering*, vol. 53, no. 7, pp. 1346–1356, 2006.

[18] Ascension Technology Corporation, "Flock of Birds," http://www.ascension-tech.com.

[19] Polhemus, http://www.polhemus.com.

[20] Xsens Technologies B.V., http://www.xsens.com.

[21] G. Carlet, "Essai Experimental Sur La Locomotion Humaine, Etude De La Marche," Ph.D. dissertation, Academie de Paris, 1872.

[22] E. J. Marey, *Animal Mechanism: A Treatise on Terrestrial and Aerial Locomotion*. HS king, London, 1874.

[23] J. Amar, "Trottoir Dynamographique," *Comptes rendus hebdomadaires des seances de l'Academie des Sciences*, vol. 163, pp. 130–132, 1916.

[24] H. Elftman, "The Measurement of the External Force in Walking," *Science*, vol. 88, no. 2276, pp. 152–153, 1938.

[25] D. Cunningham and G. Brown, "Two Devices for Measuring the Forces Acting on the Human Body During Walking," in *Proceedings of the Society for Experimental Stress Analysis*, vol. 9, 1952, pp. 75–90.

[26] Advanced Mechanical Technology, Inc. (AMTI), http://amti.biz.

[27] The Kistler Corporation, http://www.kistler.com.

[28] D. Roetenberg, H. J. Luinge, C. T. M. Baten, and P. H. Veltink, "Compensation of Magnetic Disturbances Improves Inertial and Magnetic Sensing of Human Body Segment Orientation," *IEEE Transaction on Neural Systems and Rehabilitation Engineering*, vol. 13, no. 3, pp. 395–405, 2005.

[29] H. Tan, A. M. Wilson, and J. Lowe, "Measurement of Stride Parameters Using a Wearable GPS and Inertial Measurement Unit," *Journal of Biomechanics*, vol. 41, no. 7, pp. 1398–1406, 2008.

[30] D. Roetenberg and P. H. Veltink, "Camera-Marker and Inertial Sensor Fusion for Improved Motion Tracking," *Gait and Posture*, vol. 22, no. S1, pp. 51–52, 2005.

[31] E. Foxlin, M. Harrington, and G. Pfeifer, "Constellation: A Wide-Range Wireless Motion-Tracking System for Augmented Reality and Virtual Set Applications," in *Proceedings of the ACM SIGGRAPH Conference on Computer Graphics*, Orlando, Florida, USA, 1998, pp. 371–378.

[32] M. Tanigawa, J. D. Hol, F. Dijkstra, H. J. Luinge, and P. J. Slycke, "Augmentation of Low-Cost GPS/MEMS INS with UWB Positioning System for Seamless Outdoor/Indoor Positioning," in *ION GNSS* , vol. Session C4: Indoor Positioning, Savannah, Georgia, 2008.

[33] S. Emura and S. Tachi, "Multisensor Integrated Prediction for Virtual Reality," *Presence*, vol. 7, no. 4, pp. 410–422, 1998.

[34] D. Roetenberg, P. Slycke, A. Ventevogel, and P. H. Veltink, "A Portable Magnetic Position and Orientation Tracker," *Sensors and Actuators A: Physical*, vol. 135, no. 2, pp. 426–432, 2007.

[35] D. Roetenberg, P. Slycke, and P. H. Veltink, "Ambulatory Position and Orientation Tracking Fusing Magnetic and Inertial Sensing," *IEEE Transactions on Biomedical Engineering*, vol. 54, no. 5, pp. 883–890, 2007.

[36] P. H. Veltink, C. B. Liedtke, E. Droog, and H. van der Kooij, "Ambulatory Measurement of Ground Reaction Forces," *IEEE Transactions on Neural Systems and Rehabilitation Engineering*, vol. 13, no. 3, pp. 423–427, 2005.

[37] S. J. M. Bamberg, A. Y. Benbasat, D. M. Scarborough, D. E. Krebs, and J. A. Paradiso, "Gait Analysis Using a Shoe-Integrated Wireless Sensor System," *IEEE Transactions on Information Technology in Biomedicine*, vol. 12, no. 4, pp. 413–423, 2008.

[38] M. A. Razian and M. G. Pepper, "Design, Development, and Characteristics of an in-Shoe Triaxial Pressure Measurement Transducer Utilizing a Single Element of Piezoelectric Copolymer Film," *IEEE Transactions on Neural Systems and Rehabilitation Engineering*, vol. 11, no. 3, pp. 288–293, 2003.

[39] A. Forner-Cordero, H. F. J. M. Koopman, and F. C. T. van der Helm, "Use of Pressure Insoles to Calculate the Complete Ground Reaction Forces," *Journal of Biomechanics*, vol. 37, pp. 1427–1432, 2004.

[40] H. H. C. M. Savelberg and A. L. H. de Lange, "Assessment of the Horizontal, Fore-Aft Component of the Ground Reaction Force from Insole Pressure Patterns by Using Artificial Neural Networks," *Clinical Biomechanics*, vol. 14, pp. 585–592, 1999.

[41] K. Zhang, M. Sun, D. Kevin Lester, F. Xavier Pi-Sunyer, C. N. Boozer, and R. W. Longman, "Assessment of Human Locomotion by Using an Insole Measurement System and Artificial Neural Networks," *Journal of Biomechanics*, vol. 38, no. 11, pp. 2276–2287, 2005.

[42] M. Kljajić and J. Krajnik, "The Use of Ground Reaction Measuring Shoes in Gait Evaluation," *Clinical Physics and Physiological Measurement*, vol. 8, pp. 133–142, 1987.

[43] L.-P. Chao and C.-Y. Yin, "The Six-Component Force Sensor for Measuring the Loading of the Feet in Locomotion," *Materials and Design*, vol. 20, no. 5, pp. 237–244, 1999.

[44] D. A. Winter, *Biomechanics and Motor Control of Human Movement*, 2nd ed. New York: Wiley, 1990.

[45] H. F. J. M. Koopman, H. J. Grootenboer, and H. J. de Jongh, "An Inverse Dynamics Model for the Analysis, Reconstruction and Prediction of Bipedal Walking," *Journal of Biomechanics*, vol. 28, no. 11, pp. 1369–1376, 1995.

[46] A. Forner-Cordero, H. F. J. M. Koopman, and F. C. T. van der Helm, "Inverse Dynamics Calculations During Gait with Restricted Ground Reaction Force Information from Pressure Insoles," *Gait and Posture*, vol. 23, no. 2, pp. 189–199, 2006.

[47] A. H. Hansen, D. S. Childress, S. C. Miff, S. A. Gard, and K. P. Mesplay, "The Human Ankle During Walking: Implications for Design of Biomimetic Ankle Prostheses," *Journal of Biomechanics*, vol. 37, no. 10, pp. 1467–1474, 2004.

[48] S. Barnett, J. L. Cunningham, and S. West, "A Comparison of Vertical Force and Temporal Parameters Produced by an in-Shoe Pressure Measuring System and a Force Platform," *Clinical Biomechanics*, vol. 15, no. 10, pp. 781–785, 2000.

[49] K. J. Chesnin, L. Selby-Silverstein, and M. P. Besser, "Comparison of an in-Shoe Pressure Measurement Device to a Force Plate: Concurrent Validity of Center of Pressure Measurements," *Gait and Posture*, vol. 12, pp. 128–133, 2000.

[50] E. S. Roland, M. L. Hull, and S. M. Stover, "Design and Demonstration of a Dynamometric Horseshoe for Measuring Ground Reaction Loads of Horses During Racing Conditions," *Journal of Biomechanics*, vol. 38, pp. 2102–2112, 2005.

[51] H. J. Luinge and P. H. Veltink, "Measuring Orientation of Human Body Segments Using Miniature Gyroscopes and Accelerometers," *Medical and Biological Engineering and Computing*, vol. 43, no. 2, pp. 273–282, 2005.

[52] E. R. Bachmann, "Inertial and Magnetic Tracking of Limb Segment Orientation for Inserting Humans into Synthetic Environments," PhD Thesis, Naval Postgraduate School, 2000.

[53] R. K. Curey, M. E. Ash, L. O. Thielman, and C. H. Barker, "Proposed IEEE Inertial Systems Terminology Standard and Other Inertial Sensor Standards," *IEEE Position Location Navigation Symposium 2004*, 2004.

[54] P. H. Veltink, P. Slycke, J. Hemssems, R. Buschman, G. Bultstra, and H. Hermens, "Three Dimensional Inertial Sensing of Foot Movements for Automatic Tuning of a Two-Channel Implantable Drop-Foot Stimulator," *Medical Engineering and Physics*, vol. 25, pp. 21–28, 2003.

[55] D. Roetenberg, "Inertial and Magnetic Sensing of Human Motion," PhD Thesis, University of Twente, 2006.

[56] A. M. Sabatini, C. Martelloni, S. Scapellato, and F. Cavallo, "Assessment of Walking Features from Foot Inertial Sensing," *IEEE Transactions on Biomedical Engineering*, vol. 52, no. 3, pp. 486–494, 2005.

[57] I. P. I. Pappas, M. R. Popovic, T. Keller, V. Dietz, and M. Morari, "A Reliable Gait Phase Detection System," *IEEE Transactions on Neural Systems and Rehabilitation Engineering*, vol. 9, no. 2, pp. 113–125, 2001.

[58] A. L. Hof, "An Explicit Expression for the Moment in Multibody Systems," *Journal of Biomechanics*, vol. 25, no. 10, pp. 1209–1211, 1992.

[59] J. E. Bortz, "A New Mathematical Formulation for Strapdown Inertial Navigation," *IEEE Transactions on Aerospace and Electronic Systems*, vol. 7, no. 1, pp. 61–66, 1971.

[60] B. A. MacWilliams, M. Cowley, and D. E. Nicholson, "Foot Kinematics and Kinetics During Adolescent Gait," *Gait and Posture*, vol. 17, no. 3, pp. 214–224, 2003.

[61] C. B. Liedtke, S. A. W. Fokkenrood, J. T. Menger, H. van der Kooij, and P. H. Veltink, "Evaluation of Instrumented Shoes for Ambulatory Assessment of Ground Reaction Forces," *Gait and Posture*, vol. 26, no. 1, pp. 39–47, 2007.

[62] D. A. Winter, "Human Balance and Posture Control During Standing and Walking," *Gait and Posture*, vol. 3, no. 4, pp. 193–214, 1995.

[63] M. A. Townsend, "Biped Gait Stabilization Via Foot Placement," *Journal of Biomechanics*, vol. 18, no. 1, pp. 21–38, 1985.

[64] C. E. Bauby and A. D. Kuo, "Active Control of Lateral Balance in Human Walking," *Journal of Biomechanics*, vol. 33, no. 11, pp. 1433–1440, 2000.

[65] T. M. Owings and M. D. Grabiner, "Variability of Step Kinematics in Young and Older Adults," *Gait and Posture*, vol. 20, no. 1, pp. 26–29, 2004.

[66] F. Danion, E. Varraine, M. Bonnard, and J. Pailhous, "Stride Variability in Human Gait: The Effect of Stride Frequency and Stride Length," *Gait and Posture*, vol. 18, no. 1, pp. 69–77, 2003.

[67] A. L. Hof, R. M. van Bockel, T. Schoppen, and K. Postema, "Control of Lateral Balance in Walking: Experimental Findings in Normal Subjects and above-Knee Amputees," *Gait and Posture*, vol. 25, no. 2, pp. 250–258, 2007.

[68] J. B. Dingwell, J. P. Cusumano, P. R. Cavanagh, and D. Sternad, "Local Dynamic Stability Versus Kinematic Variability of Continuous Overground and Treadmill Walking," *Journal of Biomechanical Engineering*, vol. 123, no. 1, pp. 27–32, 2001.

[69] H. J. Luinge, "Inertial Sensing of Human Movement," PhD Thesis, University of Twente, 2002.

[70] H. M. Schepers, H. F. J. M. Koopman, and P. H. Veltink, "Ambulatory Assessment of Ankle and Foot Dynamics," *IEEE Transactions on Biomedical Engineering*, vol. 54, no. 5, pp. 895–902, 2007.

[71] W. Zijlstra and A. L. Hof, "Assessment of Spatio-Temporal Gait Parameters from Trunk Accelerations During Human Walking," *Gait and Posture*, vol. 18, no. 2, pp. 1–10, 2003.

[72] H. M. Schepers, E. H. F. Asseldonk, J. H. Buurke, and P. H. Veltink, "Ambulatory Estimation of Center of Mass Displacement During Walking," *IEEE Transactions on Biomedical Engineering*, vol. 56, no. 4, pp. 1189–1195, 2009.

[73] H. M. Schepers and P. H. Veltink, "A Stochastic Magnetic Measurement Model for the on-Body Estimation of Relative Positions and Orientations," in *BME2009*, Egmond aan Zee, The Netherlands, 2009, p. 79.

[74] K. Kiriyama, T. Warabi, M. Kato, T. Yoshida, and N. Kokayashi, "Medial-Lateral Balance During Stance Phase of Straight and Circular Walking of Human Subjects," *Neuroscience Letters*, vol. 388, no. 2, pp. 91–95, 2005.

[75] A. D. Kuo, "Energetics of Actively Powered Locomotion Using the Simplest Walking Model," *Journal of Biomechanical Engineering*, vol. 124, pp. 113–120, 2002.

[76] S. S. Hasan, D. W. Robin, D. W. Szurkus, D. H. Ashmead, S. W. Peterson, and R. G. Shiavi, "Simultaneous Measurement of Body Center of Pressure and Center of Gravity During Upright Stance. Part I: Methods," *Gait and Posture*, vol. 4, no. 1, pp. 1–10, 1996.

[77] ——, "Simultaneous Measurement of Body Center of Pressure and Center of Gravity During Upright Stance. Part II: Amplitude and Frequency Data," *Gait and Posture*, vol. 4, no. 1, pp. 11–20, 1996.

[78] G. A. Cavagna, "Force Platforms as Ergometers," *Journal of Applied Physiology*, vol. 39, no. 1, pp. 174–179, 1975.

[79] T. Shimba, "An Estimation of Center of Gravity from Force Platform Data," *Journal of Biomechanics*, vol. 17, no. 1, pp. 53–60, 1984.

[80] V. M. Zatsiorsky and D. L. King, "An Algorithm for Determining Gravity Line Location from Posturographic Recordings," *Journal of Biomechanics*, vol. 31, no. 2, pp. 161–164, 1998.

[81] J. M. Donelan, R. Kram, and A. D. Kuo, "Simultaneous Positive and Negative External Mechanical Work in Human Walking," *Journal of Biomechanics*, vol. 35, no. 1, pp. 117–124, 2002.

[82] O. Caron, B. Faure, and Y. Breniere, "Estimating the Centre of Gravity of the Body on the Basis of the Centre of Pressure in Standing Posture," *Journal of Biomechanics*, vol. 30, no. 11, pp. 1169–1171, 1997.

[83] B. J. Benda, P. O. Riley, and D. E. Krebs, "Biomechanical Relationship between Center of Gravity and Center of Pressure During Standing," *IEEE Transactions on Rehabilitation Engineering*, vol. 2, no. 1, pp. 3–10, 1994.

[84] Y. Breniere, "Why We Walk the Way We Do," *Journal of Motor Behaviour*, vol. 28, no. 4, pp. 291–298, 1996.

[85] J. B. Saunders, V. T. Inman, and H. D. Eberhart, "The Major Determinants in Normal and Pathological Gait," *The Journal of Bone and Joint Surgery*, vol. 35, no. 3, pp. 543–558, 1953.

[86] M. W. Whittle, "Three-Dimensional Motion of the Center of Gravity of the Body During Walking," *Human Movement Science*, vol. 16, no. 2, pp. 347–355, 1997.

[87] M. H. A. Eames, A. Cosgrove, and R. Baker, "Comparing Methods of Estimating the Total Body Centre of Mass in Three-Dimensions in Normal and Pathological Gaits," *Human Movement Science*, vol. 18, no. 5, pp. 637–646, 1999.

[88] S. A. Gard, S. C. Miff, and A. D. Kuo, "Comparison of Kinematic and Kinetic Methods for Computing the Vertical Motion of the Body Center of Mass During Walking," *Human Movement Science*, vol. 22, no. 6, pp. 597–610, 2004.

[89] E. M. Gutierrez-Farewik, A. Bartonek, and H. Saraste, "Comparison and Evaluation of Two Common Methods to Measure Center of Mass Displacement in Three Dimensions During Gait," *Human Movement Science*, vol. 25, no. 2, pp. 238–256, 2006.

[90] M. A. Thirunarayan, D. C. Kerrigan, M. Rabufetti, U. Della Croce, and M. Saini, "Comparison of Three Methods for Estimating Vertical Displacement of Center of Mass During Level Walking in Patients," *Gait and Posture*, vol. 4, no. 4, pp. 306–314, 1996.

[91] D. Lafond, M. Duarte, and F. Prince, "Comparison of Three Methods to Estimate the Center of Mass During Balance Assessment," *Journal of Biomechanics*, vol. 37, no. 9, pp. 1421–1426, 2004.

[92] D. Lenzi, A. Cappello, and L. Chiari, "Influence of Body Segment Parameters and Modeling Assumptions on the Estimate of Center of Mass Trajectory," *Journal of Biomechanics*, vol. 36, no. 9, pp. 1335–1341, 2003.

[93] H. M. Schepers, H. F. J. M. Koopman, C. T. M. Baten, and P. H. Veltink, "Ambulatory Measurement of Ground Reaction Force and Estimation of Ankle and Foot Dynamics," in *ISB2007*, Taipei, Taiwan, 2007.

[94] R. F. Chandler, C. E. Clauser, J. T. McConville, H. M. Reynolds, and J. W. Young, "Investigation of inertial properties of the human body," National Technical Information Service, Springfield, Virginia, USA, Tech. Rep. DOT HS-801430, 1975.

[95] A. L. Hof and E. Otten, "Assessment of Two-Dimensional Induced Accelerations from Measured Kinematic and Kinetic Data," *Gait and Posture*, vol. 22, pp. 182–188, 2005.

[96] E. Foxlin, "Pedestrian Tracking with Shoe-Mounted Inertial Sensors," *Computer Graphics and Applications, IEEE*, vol. 25, no. 6, pp. 38–46, 2005.

[97] F. Caron, E. Duflos, D. Pomorski, and P. Vanheeghe, "GPS/IMU Data Fusion Using Multisensor Kalman Filtering: Introduction of Contextual Aspects," *Information Fusion*, vol. 7, no. 2, pp. 221–230, 2006.

[98] J. Kuipers, "Tracking and determining orientation of object using coordinate transformation means, system and process," pp. 1–13, 1976.

[99] F. H. Raab, E. B. Blood, T. O. Steiner, and H. R. Jones, "Magnetic Position and Orientation Tracking System," *IEEE Transactions on Aerospace and Electronic Systems*, vol. 15, no. 5, pp. 709–718, 1979.

[100] E. Paperno, I. Sasada, and E. Leonovich, "A New Method for Magnetic Position and Orientation Tracking," *Magnetics, IEEE Transactions on*, vol. 37, no. 4, pp. 1938–1940, 2001.

[101] D. K. Cheng, *Field and Wave Electromagnetics*, 2nd ed. Addison-Wesley, 1989.

[102] R. G. Brown and P. Y. C. Hwang, *Introduction to Random Signals and Applied Kalman Filtering*, 3rd ed. John Wiley, 1997.

[103] S. LaScalza, J. Arico, and R. Hughes, "Effect of Metal and Sampling Rate on Accuracy of Flock of Birds Electromagnetic Tracking System," *Journal of Biomechanics*, vol. 36, no. 1, pp. 141–144, 2003.

[104] M. A. Nixon, B. C. McCallum, W. R. Fright, and N. B. Price, "The Effects of Metals and Interfering Fields on Electromagnetic Trackers," *Presence*, vol. 7, no. 2, pp. 204–218, 1998.

[105] W. H. K. de Vries, H. E. J. Veeger, C. T. M. Baten, and F. C. T. van der Helm, "Magnetic Distortion in Motion Labs, Implications for Validating Inertial Magnetic Sensors," *Gait and Posture*, vol. 29, no. 4, pp. 535–541, 2009.

[106] H. J. Luinge, P. H. Veltink, and C. T. M. Baten, "Ambulatory Measurement of Arm Orientation," *Journal of Biomechanics*, vol. Accepted, 2007.

[107] R. Zhu and Z. Zhou, "A Real-Time Articulated Human Motion Tracking Using Tri-Axis Inertial/Magnetic Sensors Package," *IEEE Transactions on Neural Systems and Rehabilitation Engineering*, vol. 12, no. 2, pp. 295–302, 2004.

[108] G. S. Faber, I. Kingma, A. J. M. Bakker, and J. H. van DieÃ«n, "Low-Back Loading in Lifting Two Loads Beside the Body Compared to Lifting One Load in Front of the Body," *Journal of Biomechanics*, vol. 42, no. 1, pp. 35–41, 2009.

[109] A. Gelb, *Applied Optimal Estimation*. The M.I.T. press, 1974.

[110] D. Roetenberg, H. J. Luinge, and P. Slycke, "6 DOF Motion Analysis Using Inertial Sensors," in *Proceedings of Measuring Behavior 2008, 6th International Conference on Methods and Techniques in Behavioral Research*, Maastricht, The Netherlands, 2008, pp. 14–15.

[111] S. J. Julier and J. K. Uhlmann, "A New Extension of the Kalman Filer to Nonlinear Systems," in *International Symposium on Aerospace/Defense Sensing, Simulation and Controls*, Orlando, USA, 1997.

[112] F. Gustafsson, F. Gunnarsson, N. Bergman, U. Forssell, J. Jansson, R. Karlsson, and P.-J. Nordlund, "Particle Filters for Positioning, Navigation and Tracking," *IEEE Transactions on Signal Processing*, vol. 50, no. 2, pp. 425–437, 2002.

[113] P. H. Veltink, H. G. Kortier, and H. M. Schepers, "Sensing Power Transfer between the Human Body and the Environment," *IEEE Transactions on Biomedical Engineering*, vol. In Press, 2009.

[114] C. Giacomozzi and V. Macellari, “Piezo-Dynamometric Platform for a More Complete Analysis of Foot-to-Floor Interaction,” *Rehabilitation Engineering, IEEE Transactions on*, vol. 5, no. 4, pp. 322–330, 1997.

Summary

Traditional human movement analysis systems consist of an optical position measurement system with one or more 6D force plates mounted in a laboratory. Although clinically accepted as 'the golden standard' for the assessment of human movement, the restriction to a laboratory environment with its limited measurement volume prevents these systems to be used in an ambulatory environment. Moreover, optical measurement systems suffer from marker visibility problems, since the line of sight from camera to marker is easily blocked due to movement of the subject. A correct force measurement requires subjects to place their feet completely on the force plates, which poses a restriction on the natural gait pattern. With only one or a few force plates mounted in a laboratory, this also means that usually many successive trials are required to obtain sufficient data. Another drawback is the impossibility to distinguish the ground reaction force acting on each foot when standing with both feet on a single force plate, as only the total ground reaction force is registered. To overcome these limitations, this thesis has two objectives which can be summarized as follows:

- Develop and evaluate a method to assess the 3D ground reaction force, the center of pressure trajectory, the center of mass trajectory, and the movement of the foot using an instrumented shoe.
- Develop and evaluate a method to estimate relative positions and orientations on the human body by fusion of inertial and magnetic sensing using a tightly coupled filter structure. The method should not be dependent on a specific coil configuration and should allow the instants of actuation to be chosen adaptively based on the uncertainty of the estimated position and orientation. Furthermore, the number of actuations and the actuation parameters should be chosen such that the system achieves maximal accuracy at minimal energy consumption.

The first objective is discussed in Chapters 2 to 4. In Chapter 2, an instrumented shoe for assessing the dynamics of ankle and foot is introduced, which integrates the measurement of ground reaction force with the measurement of human movement. The instrumented shoe consists of an orthopaedic sandal with two 6D force/moment sensors mounted beneath the heel and the forefoot, and two inertial sensors rigidly attached to the force/moment sensors. Data obtained from a healthy subject was used for validation by comparison with a reference optical position measurement system and a force plate. The ground reaction force and ankle moment showed good correspondence with the reference system, indicated by the average rms difference being $1.1\ \%$ of the maximal magnitude for the ground reaction force, and $2.3\ \%$ of the maximal magnitude for the ankle moment. The average rms difference between the center of pressure trajectories estimated by both measurement systems was 5.1 mm, corresponding to $1.7\ \%$ of the length of the shoe. The reproduction of the ankle power showed larger differences ($14\ \%$ of the maximal power), which was caused by an inaccurate estimation of the angular velocity by the reference system due to the use of a single segment foot model.

The instrumented shoe is used in Chapter 3 to assess lateral foot placement and stride length of each foot during human walking. To analyze if the ambulatory system is able to discriminate between different walking conditions, both parameters were determined during walking with eyes open and with eyes closed. An optical position measurement system was used as a reference to analyze the accuracy of the ambulatory measurement system. The average percentage difference between both measurement systems was calculated as $7.8\ \%$ for lateral foot placement, and $0.67\ \%$ for stride length. Moreover, the ambulatory system was able to discriminate between different walking conditions, like the reference system.

Chapter 4 proposes a method to continuously estimate center of mass displacement during walking using the instrumented shoe. The estimation of center of mass displacement is achieved by fusing low-pass filtered center of pressure data with high-pass filtered double integrated center of mass acceleration, both estimated using the instrumented shoes. A comparison with an optical position measurement system based on the segmental kinematics methods for a group of seven stroke patients revealed that the center of mass can be continuously estimated, allowing center of mass displacement to be assessed under ambulatory conditions. The average rms difference of each component of the center of mass displacement was 0.020 m for the forward direction, 0.013 m for the lateral direction, and 0.007 m for the upward direction.

The second objective is discussed in Chapter 5 and Chapter 6. A stochastic magnetic measurement model that can be used to predict the magnetic field generated by a source coil at the location of a sensor, based on an estimation of the relative position and orientation of the sensor with respect to the source is described in Chapter 5. The measurement model is used in a realtime Extended Kalman Filter (EKF) with a tightly coupled structure described in Chapter 6, to estimate relative position and orientation of the sensor with respect to the source. Change of position and orientation is predicted by integration of acceleration and angular velocity measured by an inertial sensor. Magnetic updates are used to reduce the inherent integration drift due to noise and a fluctuating offset. To minimize energy consumption, the magnetic system only actuates if the uncertainty associated with the position and orientation exceeds a predefined threshold. Moreover, only the coil delivering most information for the reduction of the uncertainty is actuated. Two sources of error were defined that could lead to divergence of the fusion filter, being the use of a linearized version of the nonlinear measurement model to update the estimate of position and orientation, and the appearance of ferromagnetic objects in the vicinity of the source or sensor. It appeared that the linearized model introduced errors which generally increased for sensor locations near the source, and that a ferromagnetic object influenced the measurements only if it was located near or between the source and sensor. The performance of the fusion filter was evaluated by comparison with an optical position measurement system. The filter was able to provide a stable and accurate estimation of relative position and orientation for several types of movements, as indicated by the average rms error being 0.033 m for the position and 3.6 degrees for the orientation.

Samenvatting

Traditionele systemen voor de analyse van menselijke beweging bestaan uit een optisch positie meetsysteem met één of enkele 6D krachtplaten ingebouwd in een laboratorium. Hoewel deze meetsystemen klinisch worden geaccepteerd als 'de gouden standaard' voor de analyse van menselijke beweging, zorgt de gebondenheid aan een laboratorium omgeving met het beperkte meetvolume ervoor dat deze systemen niet kunnen worden gebruikt voor ambulante metingen. Daarnaast hebben optische systemen last van marker zichtbaarheid problemen, omdat de visuele verbindingslijn tussen camera en marker makkelijk wordt verbroken door beweging van de proefpersoon. Een correcte meting met een krachtplaat vereist dat de voeten van de proefpersoon compleet op de krachtplaat worden geplaatst, wat tot verstoringen van het natuurlijke looppatroon kan leiden. Bovendien bevat een laboratorium normaal gesproken slechts één of enkele krachtplaten, waardoor er vaak veel metingen nodig zijn om voldoende data te verkrijgen. Een ander nadeel is dat het niet mogelijk is om de grond reactie kracht onder iedere voet te onderscheiden, omdat alleen de totale grond reactie kracht wordt gemeten. Om deze nadelen te verhelpen, heeft dit proefschrift twee doelstellingen die als volgt kunnen worden samengevat:

- Ontwikkel en evalueer een methode voor het schatten van de 3D grond reactie kracht, de verplaatsing van het aangrijpingspunt, de verplaatsing van het massamiddelpunt van het lichaam en de beweging van de voeten door gebruik te maken van een geïnstrumenteerde schoen.
- Ontwikkel en evalueer een methode voor het schatten van relatieve posities en oriëntaties op het menselijk lichaam door fusie van inertiële en magnetische metingen in een Kalman filter. De methode mag niet afhankelijk zijn van een bepaalde spoelenconfiguratie en moet het mogelijk maken om de momenten van actueren adaptief te kiezen op basis van een schatting van de onzekerheid van de positie en oriëntatie. Daarnaast moeten het aantal actuaties en de actuatie parameters zo gekozen worden dat het systeem maximale nauwkeurigheid bereikt bij minimaal energieverbruik.

De eerste doelstelling wordt behandeld in Hoofdstuk 2, 3 en 4. In Hoofdstuk 2 wordt een geïnstrumenteerde schoen geïntroduceerd om de dynamica van voet en enkel te schatten door metingen van kracht en beweging van het menselijk lichaam te combineren. De geïnstrumenteerde schoen bestaat uit een orthopedische sandaal met twee 6D kracht/moment sensoren die onder de schoen zijn bevestigd en twee inertiële sensoren die star zijn verbonden aan de kracht/moment sensoren. Het ambulante systeem is gevalideerd door vergelijking met een optisch positie meetsysteem en een krachtplaat met behulp van metingen aan een gezonde proefpersoon. De grond reactie kracht en het enkel moment kwamen goed overeen met het referentiesysteem, zoals bevestigd door het gemiddelde rms verschil van $1.1\ \%$ van de maximale grond reactie kracht en $2.3\ \%$ van het maximale enkel moment. Het gemiddelde rms verschil tussen de paden van het aangrijpingspunt geschat door beide systemen was 5.1 mm, ofwel $1.7\ \%$ van de lengte van de schoen. De schatting van het enkel vermogen toonde een groter verschil ($14\ \%$ van het maximale vermogen), veroorzaakt door een foute schatting van de hoeksnelheid door het referentiesysteem dat gebruik maakte van een voetmodel gebaseerd op slechts één segment.

De geïnstrumenteerde schoen is gebruikt in Hoofdstuk 3 voor de schatting van laterale voetplaatsing en stap lengte van iedere voet tijdens lopen. Om te analyseren of het systeem in staat is verschillende loopcondities te onderscheiden, zijn beide parameters geschat tijdens lopen met ogen open en ogen dicht. Een optisch positie meetsysteem is als referentie gebruikt om de

nauwkeurigheid van het ambulante meetsysteem te analyseren. Het gemiddelde percentuele verschil tussen beide meetsystemen was $7.8\ \%$ voor de laterale voetplaatsing en $0.67\ \%$ voor de stap lengte. Daarnaast was het ambulante systeem in staat om verschillende loopcondities te onderscheiden, evenals het referentie systeem.

Hoofdstuk 4 stelt een methode voor om de verplaatsing van het massamiddelpunt tijdens lopen te schatten met behulp van de geïnstrumenteerde schoen. De schatting van de verplaatsing van het massamiddelpunt is verkregen door fusie van laagdoorlaat gefilterde beweging van het aangrijpingspunt met hoogdoorlaat gefilterde dubbel geïntegreerde versnelling van het massamiddelpunt, beide geschat met de geïnstrumenteerde schoen. Een vergelijking met een optisch positie meetsysteem voor een groep van zeven CVA patiënten liet zien dat het massamiddelpunt continu geschat kan worden. Het gemiddelde rms verschil voor iedere component van de beweging van het massamiddelpunt was 0.020 m voor de voorwaartse richting, 0.013 m voor de zijwaartse richting en 0.007 m voor de verticale richting.

De tweede doelstelling is behandeld in Hoofdstuk 5 en Hoofdstuk 6. Een stochastisch magnetisch meetmodel dat gebruikt kan worden om het magnetisch veld op de locatie van een sensor te voorspellen dat is gegenereerd door een bron bestaande uit een enkele spoel, gebaseerd op een schatting van de relatieve positie en oriëntatie van de sensor ten opzichte van de bron is beschreven in Hoofdstuk 5. Het meetmodel is gebruikt in een realtime Extended Kalman Filter (EKF) beschreven in Hoofdstuk 6, om de relatieve positie en oriëntatie van de sensor ten opzichte van de bron te schatten. Verandering van positie en oriëntatie zijn geschat door integratie van versnelling en hoeksnelheid gemeten door een inertiële sensor. Magnetische metingen zijn gebruikt om de integratie drift te verminderen die veroorzaakt wordt door ruis en een variërende offset. Om het energieverbruik te minimaliseren, wordt het magnetisch systeem alleen geactueerd als de geschatte onzekerheid van de positie en oriëntatie boven een vooraf vastgestelde drempel komt. Daarnaast wordt alleen die spoel geactueerd, die de grootste bijdrage aan de verlaging van de onzekerheid heeft. Twee foutenbronnen zijn vastgesteld die kunnen leiden tot divergentie van het fusiefilter, namelijk het gebruik van een gelineariseerd meetmodel om de schatting van positie en oriëntatie bij te werken en de aanwezigheid van ferromagnetische objecten in de nabijheid van bron of sensor. De fouten veroorzaakt door het gelineariseerde meetmodel waren over het algemeen groter als de sensor zich dichtbij de bron bevindt. Daarnaast heeft een ferromagnetisch object alleen invloed als deze zich dichtbij of tussen de bron en sensor bevindt. De prestaties van het fusiefilter zijn geëvalueerd door te vergelijken met een optisch positie meetsysteem. De resultaten laten zien dat het filter in staat is om een stabiele en nauwkeurige schatting te geven van de relatieve positie en oriëntatie voor verschillende typen bewegingen, zoals ook wordt bevestigd door de gemiddelde rms fout van 0.033 m voor de positie en 3.6 graden voor de oriëntatie.

Dankwoord

Het resultaat van vier jaar zwoegen is dan toch eindelijk daar, mijn proefschrift is klaar! Hoewel ik toch het grootste deel zelf heb moeten doen, zijn er een aantal personen zonder wie dit resultaat er niet zou zijn en die ik dan ook graag wil bedanken.

Vanzelfsprekend begin ik met mijn dagelijks begeleider en promotor, Peter Veltink. Vanaf het begin van mijn promotie is onze relatie uitstekend geweest. In de loop van mijn promotie werden de discussies steeds interessanter en betrok je me meer en meer bij andere, aanverwante zaken wat ik zeer op prijs heb gesteld. Keer op keer wist je met je commentaar zowel de algehele structuur als de details van mijn stukken tekst fors te verbeteren, iets wat ik erg heb bewonderd. Daarnaast zorgde jouw enthousiasme ervoor dat ik er vol voor bleef gaan. Ik hoop dat we in de toekomst een goede samenwerking kunnen behouden.

De medewerkers van Xsens wil ik bedanken voor alle hulp en advies tijdens mijn promotie. In het bijzonder wil ik Daniel, Henk en Per bedanken. Daniel Roetenberg, je hebt me aan het begin van mijn promotie ingewerkt in het project FreeMotion. Inmiddels zijn we bij Xsens herenigd en ben je druk bezig datzelfde te doen in de interessante onderwerpen en projecten bij Xsens. Je hebt het zelfs voor elkaar gekregen dat ik je aan ga spreken met 'Zeergeleerde Opponent'! Henk Luinge, je bent altijd een warm voorstander geweest van de krachtschoen en ik zie dan ook erg uit naar onze samenwerking de komende jaren. Per Slycke, vanaf het begin van mijn promotie toonde je veel interesse in mijn werk en ik ben dan ook zeer vereerd om nu voor Xsens te mogen werken. Daarnaast heb ik veel geleerd van het schrijven van het Business Plan onder jouw begeleiding voor de integratie van delen van mijn onderzoek in de producten van Xsens.

Bart Koopman, als afgestudeerd Elektrotechnicus had ik met name in het begin wat moeite met de (bio)mechanische aspecten van mijn onderzoek. Jouw ondersteuning heeft veel geholpen met als resultaat de publicatie van Hoofdstuk 2 van dit proefschrift, waar je als co-auteur aan mee hebt geschreven.

Medewerkers van Roessingh Research and Development, bedankt voor de ondersteuning bij mijn onderzoek en dan met name tijdens de experimenten. Chris Baten, als voorzitter van FreeMotion reageerde je altijd vol enthousiasme over de resultaten van mijn onderzoek. Hoe druk je ook was, ik kon altijd even langskomen om bij te kletsen over zaken die in meer of mindere mate aan FreeMotion waren gerelateerd. Leendert Schaake, bedankt voor alle hulp tijdens de experimenten. Jaap Buurke en Mark Nederhand, bedankt voor jullie bijdrage vanuit de klinische hoek en ik hoop dat ons gezamenlijke werk in de toekomst gepubliceerd zal gaan worden.

Natuurlijk kon ik dit resultaat niet bereiken zonder de technische ondersteuning vanuit de vakgroep. Wim van Riel, hoewel je inmiddels al enige tijd van je welverdiende pensioen geniet, vind ik het toch jammer dat je het laatste deel van mijn promotie niet meer op de vakgroep aanwezig was. Het was voor mij een unieke ervaring om te overleggen temidden van sigaar aroma's en klassieke muziek. Ed Droog en Marcel Weusthof, het was altijd leuk om even binnen te lopen voor een gezellig praatje. Ed, jouw bijdrage aan dit onderzoek is groot geweest, hoewel je soms op tactische wijze enkele vervelende klusjes wist uit te stellen. Daarnaast heb je me geleerd dat het rijden op een Segway zeker niet zonder gevaar is...

Ook wil ik alle andere collega's van de vakgroep Biomedische Signalen en Systemen bedanken voor alle gezelligheid de afgelopen jaren. Remy Wiertz, vier jaar lang hebben we een kamer gedeeld wat me altijd uitstekend is bevallen. Bedankt dat jij mijn paranimf wilt zijn. Wies Elfers, je stond altijd klaar als er praktische zaken geregeld moesten worden en daarnaast vormden alle gesprekjes over onderwerpen die niet aan het werk waren gerelateerd een welkome afwisseling op de dagelijkse werkzaamheden.

Samen met een aantal mensen van de vakgroep Biomedische Werktuigbouwkunde heb ik de afgelopen jaren vele wedstrijden in het BSS/BW zaalvoetbalteam gespeeld, alle spelers bedankt! Toch zijn er een aantal mensen van deze vakgroep die ik in het bijzonder wil bedanken. Edsko Hekman, bedankt voor het op het oog simpele, maar slimme en uiterst functionele ontwerp van de opstelling om een zuiver moment aan te brengen voor calibratie van de krachtsensoren. Paul van Geffen en Jan Veneman, de gezamenlijke trainingen voor de BMTI triathlon heb ik altijd erg leuk gevonden, maar Paul, ik vind het toch wat overdreven om er op het moment suprême een veredelde toertocht door Twente van te maken. Edwin van Asseldonk, 'broer', je hebt een flinke inhoudelijke bijdrage gehad aan dit proefschrift door als co-auteur mee te schrijven aan twee hoofdstukken. Daarnaast hebben we een goede vriendschap opgebouwd die ik in de toekomst hoop te behouden.

De afgelopen jaren heb ik met veel plezier een aantal studenten begeleid. Arjen, Dirk, Henk, Jasper, Josien, Marianne, Vincent en William, veel van jullie werk heeft een bijdrage aan dit proefschrift gehad. Josien van den Noort wil ik graag in het bijzonder bedanken. Tijdens je afstudeeronderzoek heb je een enorme hoeveelheid data verzameld, waar nu door verschillende mensen nog dankbaar gebruikt van gemaakt wordt. Hoofdstuk 4 van dit proefschrift is op een deel van die data gebaseerd. Na je afstuderen ben je als promovendus begonnen bij het VU Medisch Centrum en ik ben verheugd dat je daar betrokken bent gebleven bij het onderzoek. Ik hoop dan ook dat we onze samenwerking in de toekomst kunnen blijven voortzetten.

Gert Faber, de blijheid en bereidheid om steeds weer als proefpersoon te fungeren en je steeds weer te laten volhangen met sensoren heeft me keer op keer verbaasd. Ik wil je bedanken voor alle hulp en advies tijdens mijn experimenten en dat je me tijdens de lange en grijze meetdagen in Amsterdam door mijn winterdip heen hebt weten te slepen.

Hoewel de eerder genoemde personen vooral een directe invloed hebben gehad op de inhoud van dit proefschrift, is ook de indirecte steun van vrienden en familie onontbeerlijk voor dit resultaat. Alle vrienden vanuit Bruchterveld, maar zeker ook de 'UT moaten' wil ik bedanken voor alle afleiding en gezelligheid. Arno en Marianne, bedankt voor de vele gezellige, maar vaak ook sportieve uurtjes. Arjan, ik vind het erg leuk dat jij mijn paranimf wilt zijn! Pa, ma, Gerlinde & Ingemar, maar ook de rest van de (schoon)familie, bedankt voor alle steun.
Danny Hof, bedankt voor het prachtige ontwerp van de omslag van dit proefschrift!

Toch is er maar één die ik als laatste wil bedanken. Lieve Leonie, bedankt voor alle steun, maar vooral ook alle liefde die je me de afgelopen jaren hebt gegeven! De laatste loodjes wogen toch het zwaarst, maar je hebt me altijd gesteund en me er doorheen weten te slepen op de momenten dat het even tegenzat. Ik geniet van elke dag die we samen zijn. Je maakt me gelukkig en ik zie dan ook erg uit naar de toekomst die we samen tegemoet gaan!

About the Author

Biography

Martin Schepers was born in Hardenberg, The Netherlands on July 4, 1981. He received his high school degree (VWO diploma) from the 'Vechtdal College' in Hardenberg in 1999. In the period from 1999 to 2004, he studied Electrical Engineering at the University of Twente, Enschede, The Netherlands. During his masters degree, he completed a five month project at the Mechatronics Research Group of Loughborough University, Loughborough, UK in 2003, on the subject of distributed control in a mobile robot.

The subject of his MSc thesis was to develop a model for a piezoelectric inertial stepping turntable using bond graphs, at the Control Engineering group of the University of Twente, with Prof.dr.ir. Stefano Stramigioli as his supervisor. In 2005, he started as a PhD student at the Biomedical Signals and Systems group of the University of Twente, under supervision of Prof.dr.ir. Peter Veltink. His research was part of the 'FreeMotion' project, which researches accurate and reliable methods of ambulatory motion analysis to provide practical decision making tools to a large group of professionals in health care, ergonomics and sports. This thesis on ambulatory assessment of human body kinematics and kinetics is the result of his contribution to the project. In April 2009, he was employed at Xsens Technologies B.V., Enschede, The Netherlands, where he is currently working on motion capture technology based on fusion of inertial sensing with various aiding sensor technologies.

List of Publications

Peer-Reviewed Journal Papers

- H.M. Schepers, H.F.J.M. Koopman, and P.H. Veltink. Ambulatory Assessment of Ankle and Foot Dynamics. *IEEE Transactions on Biomedical Engineering*, 54(5):895-902, 2007.
- H.M. Schepers, E.H.F. van Asseldonk, J.H. Buurke, and P.H. Veltink. Ambulatory Estimation of Center of Mass Displacement During Walking. *IEEE Transactions on Biomedical Engineering*, 56(4):1189-1195, 2009.
- P.H. Veltink, H.G. Kortier, and H.M. Schepers. Sensing Power Transfer between the Human Body and the Environment. *IEEE Transactions on Biomedical Engineering*, Accepted.

Peer-Reviewed Conference Proceedings

- H.M. Schepers, and P.H. Veltink. Estimation of Ankle Moment Using Ambulatory Measurement of Ground Reaction Force and Movement of Foot and Ankle. *Proceedings of the first IEEE/RAS-EMBS international conference on biomedical robotics and biomechatronics*, Pisa, Italy, Feb 20-22, 2006.
- P.H. Veltink, D. Roetenberg, H.M. Schepers, P. Slycke, and C.T.M. Baten. Movement and Force Sensing for Ambulatory 3D Human Movement Analysis. *First joint ESMAC-GCMAS Meeting*, Amsterdam, The Netherlands, Sep 27-30, 2006.
- H.M. Schepers, P.H. Veltink, and H.F.J.M. Koopman. Ambulatory Assessment of Foot Dynamics. *Annual Symposium of the IEEE/EMBS Benelux Chapter*, Brussels, Belgium, Dec 7-8, 2006.
- H.M. Schepers, and P.H. Veltink. Ambulatory Estimation of Foot Movement During Gait Using Inertial Sensors. *First Dutch Conference on Bio-Medical Engineering*, Egmond aan Zee, The Netherlands, Jan 18-19, 2007.
- H.M. Schepers, H.F.J.M. Koopman, C.T.M. Baten, and P.H. Veltink. Ambulatory Measurement of Ground Reaction Force and Estimation of Ankle and Foot Dynamics. *Program and Abstracts of the XXI Congress, International Society of Biomechanics*, Taipei, Taiwan, Jul 1-5, 2007.
- H.F.J.M. Koopman, H.M. Schepers, and P.H. Veltink. Ambulatory Measurements Require Deformable Foot Models. *Program and Abstracts of the XXI Congress, International Society of Biomechanics*, Taipei, Taiwan, Jul 1-5, 2007.
- H.M. Schepers, P.H. Veltink. Center of Mass Movement Estimation Using an Ambulatory Measurement System. *Annual Symposium of the IEEE/EMBS Benelux Chapter*, Heeze, The Netherlands, Dec 6-7, 2007.
- P.H. Veltink, H.G. Kortier, H.M. Schepers. Sensing Dynamic Interaction With the Environment. *Annual Symposium of the IEEE/EMBS Benelux Chapter*, Heeze, The Netherlands, Dec 6-7, 2007.
- H.M. Schepers, E.H.F. Van Asseldonk, J.H. Buurke, and P.H. Veltink. Center of Mass Movement Estimation Using an Ambulatory Measurement System. *International Conference on Ambulatory Monitoring of Physical Activity and Movement*, Rotterdam, The Netherlands, May 21-24, 2008.
- P.H. Veltink, H.G. Kortier, and H.M. Schepers. Sensing Dynamic Interaction With the

Environment. *International Conference on Ambulatory Monitoring of Physical Activity and Movement*, Rotterdam, The Netherlands, May 21-24, 2008.

- H.M. Schepers, H.F.J.M. Koopman, E.H.F. Van Asseldonk, J.H. Buurke, and P.H. Veltink. Ambulatory Estimation of Ankle and Foot Dynamics and Center of Mass Movement. *Proceedings of Measuring Behavior 2008, 6th International Conference on Methods and Techniques in Behavioral Research*, Maastricht, The Netherlands, Aug 26-29, 2008.
- H.M. Schepers, E.H.F. Van Asseldonk, J.H. Buurke, H.F.J.M. Koopman, and P.H. Veltink. Ambulatory Assessment of Balance. *The second IEEE/RAS-EMBS International Conference on Biomedical Robotics and Biomechatronics*, Scottsdale, Arizona, USA, Oct 19-22, 2008.
- H.M. Schepers, H.F.J.M. Koopman, E.H.F. Van Asseldonk, J.H. Buurke, and P.H. Veltink. 'The Forceshoe': What Has Been Achieved? - Ambulatory Estimation of Ankle and Foot Dynamics and Center of Mass Movement. *The 10th International Symposium on 3D Analysis of Human Movement*, Santpoort/Amsterdam, The Netherlands, Oct 28-31, 2008.
- H.M. Schepers, and P.H. Veltink. A Stochastic Magnetic Measurement Model for the On-Body Estimation of Relative Positions and Orientations. *Second Dutch Conference on Bio-Medical Engineering*, Egmond aan Zee, The Netherlands, Jan 22-23, 2009.

Publication of this thesis was financially supported by:

Biometrics
HUMAN MOTION TECHNOLOGY SOLUTIONS
www.biometrics.nl

oim
orthopedie
www.oim.nl
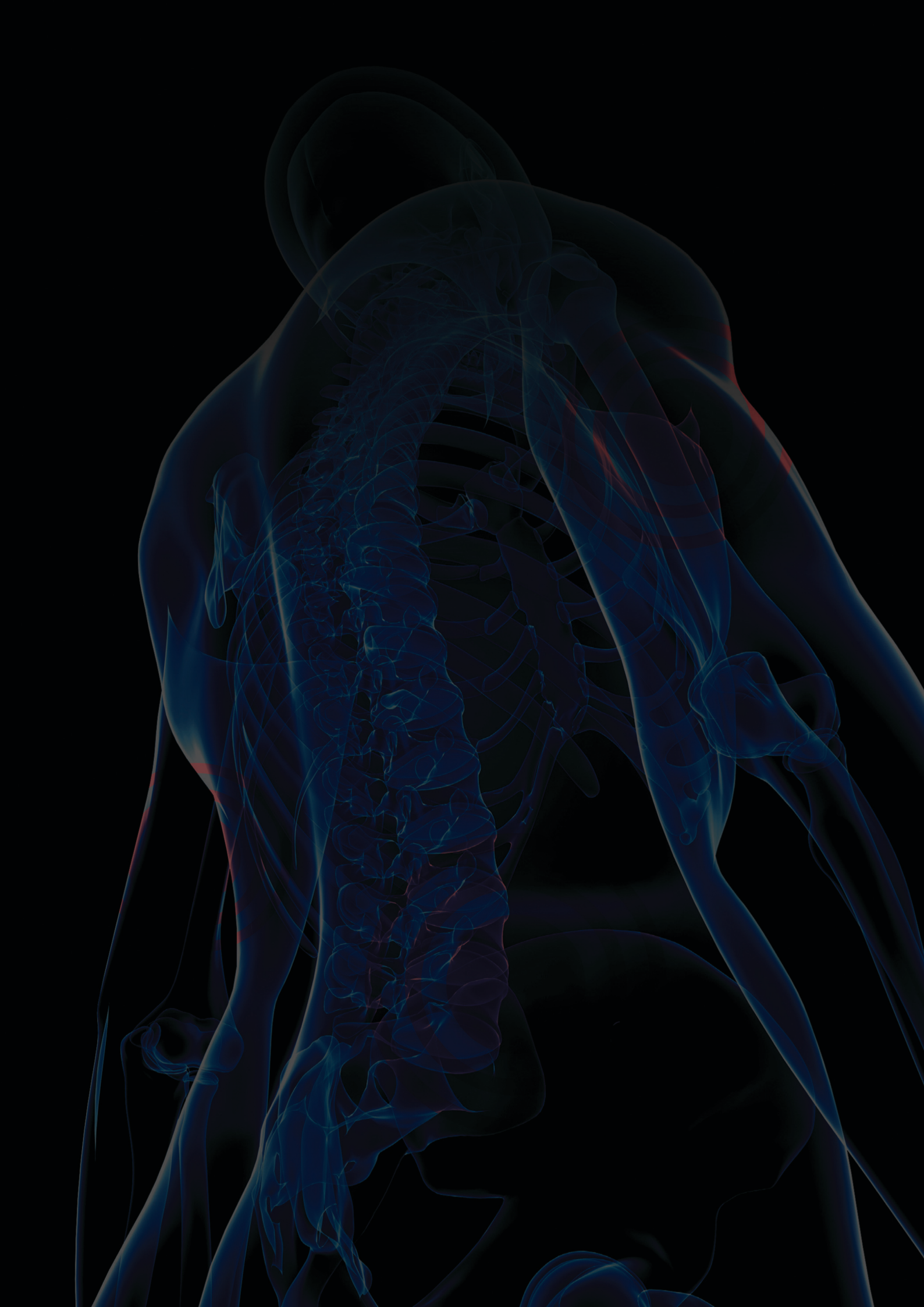
xsens
www.xsens.com